THERMAL IMAGE ANALYSIS USING CALIBRATED VIDEO

IMAGING

A Dissertation Presented to the Faculty of Graduate School

University of Missouri – Columbia

In Partial Fulfillment

Of the Requirements for the Degree

Doctor of Philosophy

by

Dong Li

Dr.  Shahla Keyvan, Dissertation Co-supervisor

Dr.  Kannappan Palaniappan, Dissertation Co-supervisor

May 2006

The undersigned, appointed by the Dean of the Graduate School, have examined the dissertation entitled

THERMAL IMAGE ANALYSIS USING CALIBRATED VIDEO IMAGING

Presented by Dong Li

A candidate for the degree Doctor of Philosophy

And hereby certify that in their opinion it is worthy of acceptance

_____

Professor Shahla Keyvan

_____

Professor Kannappan Palaniappan

_____

Professor Hongchi Shi

_____

Professor Jeffrey Uhlmann

_____

Professor Wenjun Zeng

# ACKNOWLEDGEMENTS

I would like to express sincere appreciation to my co-advisor, Dr. Shahla Keyvan, for her continuous guidance and support. Without her effort, this dissertation would not be possible.

I extend my sincere gratitude to my co-advisor, Dr. Kannappan Palaniappan, for his advices and support.

I would like to thank the committee member Dr. Hongchi Shi, Dr. Jeffrey Uhlmann, Dr. Wenjun Zeng for their advices and suggestions and their efforts in reviewing my dissertation.

I extend my appreciation on Dr. Rodney Rossow, Handi Cokrojoyo, Scott Hixson for their assistance in implementing the experiments.

I dedicate this dissertation to my parents, Fuzhi Li and Jianying Yu, my fiancée, Dandan Liu, who deserve special acknowledgement for their love and support behind me.

Finally, I would like to dedicate this dissertation to Dr. Majdi Najm, for his support from SAP project and for my deeply memorial.

# TABLE OF CONTENTS

# LIST OF ILLUSTRATIONS

VI

# LIST OF TABLES

# ABSTRACT

This research work introduces new techniques for temperature measurement that utilizes visual spectrum of light.  A periscope with a CCD camera is used to capture the image from a high temperature gas fired furnace and calculate the temperature distribution of flame and furnace wall.  The proposed visual thermal imaging methods for calculating the flame or wall temperature profiling are applied in several experiments in the laboratory and commercial furnaces.   These novel approaches include reference technique which utilizes a known temperature measured either by an infrared optical device known as IR-Gun or thermocouples; and camera response curve method which utilizes two-color blackbody technique and flame adiabatic temperature condition.  The camera calibration technology is also utilized and integrated with these temperature calculation methods to enable the temperature measurement in a specified region and produce a three dimensional temperature profiling.  Various experiments are performed and temperature data are collected both with IR-Gun and thermocouples. These data are then compared with the results of CCD camera images using the proposed methods. Calculated temperatures from various experiments indicate that these methods yield excellent results that are closely comparable with both the IR Gun readings and thermocouples records.  Furthermore, the temperature calculations resulting from these techniques provide accurate temperature trends that follow the temperature trend from thermocouples; In addition, they provide more detailed temperature variations as compared to thermocouple readings.

# 1. INTRODUCTION

Many methods for measuring temperature have been employed in the industry today. These temperature measurement applications can be divided into two types: contact and non-contact.

Conventional contact temperature measurement methods include thermocouple, resistance temperature detectors (RTDs), and thermistor etc. Ordinary mercury-in-glass thermometers also fall into this category. Contact temperature sensors such as thermocouples have a well-known technology and are commonly used to measure industrial furnace temperatures for commercial or test purposes. However, like all other contact temperature sensors, thermocouples must equilibrate with the temperature of the target material. This results in the long response time of the thermocouples. In addition, the installation of thermocouples is normally limited by working environments such as contamination, safety hazard (high voltage), and maximum or minimum measured temperature. [1, 2]

Non-contact measurement methods are so called because the measuring device does not have to touch the fluid or product being measured. They have overcome the disadvantages of traditional contact temperature measurement methods. Optical radiation pyrometer, fiber-optic sensor probe and laser-induced fluorescence (LIF) spectroscopy are examples of non-contact measurement methods.

The optical radiation pyrometers range from the traditional pyrometers used many years ago to new multi-wavelength pyrometers. The traditional pyrometers are not

accurate for measuring the temperature in the furnace because they calculate the temperature based on a single wavelength and the emissivity value of the surface. However, the emissivity information is too complicated to calculate since the actual surface conditions may not be known or the emissivity may be varying with the temperature of the object itself. Siddall et al [3] attempted to calculate the luminous emissivity based on their experiments, but the emissivity equations are not suitable to other applications since they are very sensitive to the experimental environment.

The two-color pyrometer (also called ratio pyrometer) measures the temperature independently of emissivity, hence, more and more researchers are interested in applying this technique in the industry. Basically, this type of instrument uses the ratio of two spectral radiances measured over two different wavelength bands to determine the true temperature. Hottel and Broughton [4] pioneered the two-color optical pyrometer in attempting to measure the true temperature and total radiation from the luminous gas flame temperature in the furnaces. Recently, the three-wavelength pyrometer [5] and multi-wavelength pyrometer [6] have been proposed. Multi-wavelength pyrometer split the radiation into multiple parts through interference filters and achieves the better accuracy. However, these pyrometers cannot be used to measure the particle temperature of flames which contain gases that have high emissivity in lines or bands near one of the pyrometer wavelengths. This can be detected experimentally by the fact that the radiation measured at the three wavelengths will not fit a Planck blackbody continuum. [5]

Many researchers have developed laser-based methods over the past several years. For examples, in recent years Meier et al [7] and Elloit [8] have developed laser-based methods for flame temperature measurements. Meier's technique demonstrates the

laser-induced fluorescence of the OH radical to be used for temperature measurement. Elloit utilizes an iodine vapor filter and an injection-seeded Nd:YAG laser to measure instantaneous and average temperature fields in combustion environments. Elliot's technique requires molecular seeds to be added into the flame.

Fiber-optic sensor probes [9-10] have also been used to measure combustion temperatures; however, many of these probes need to be inserted in the combustion region and can only produce single point temperature measurement at a time.

The above methods can only support the single-point temperature measurement and a limited amount of equipment can be installed in the restricted space, the spatial resolution of temperature data is insufficient for an accurate depiction of furnace temperature distribution measurement. [11] The 2-D temperature measurement known in the community is IR cameras. Aside from their high cost, they are not suitable for high temperature industrial furnace. [12]

## 1.1    Motivation

Combustion control is a matter of great importance to the operation of commercial glass furnaces and other fuel-burning devices. Optimized combustion has both economic and environmental benefits. One of the primary factors that influences both efficiency and pollutant formation of a combustion system is the relative proportion of the combustible and oxidant, typically expressed as the air/fuel (or oxygen/fuel in oxy/fuel burning glass furnace applications) ratio. The proper balance of fuel and air (or oxygen) is necessary to optimize combustion. If the mixture is fuel-rich, combustion efficiency will be low and fuel gases will contain high levels of pollutants such as carbon monoxide (CO) and unburned hydrocarbons. If the combustion mixture is fuel-lean, the

3

burned gas will have high excess air or oxygen in oxy/fuel combustion and both performance and efficiency of the combustion system will suffer and nitrogen oxide emissions would increase.

Aside from the environmental benefits of improved combustion control, there are substantial benefits for cost saving as well. Efficient combustion saves fuel. A typical glass furnace that produces an output of 200 tons of glass per day consumes about $2.4 million of fuel annually. A five percent improvement in efficiency would save well over $100,000 per year in fuel cost alone. Fuel savings are not the only financial benefits of a combustion monitoring system. Other benefits include improved product quality, improved reliability, less frequent maintenance, and longer service life of combustion-related subassemblies. [13]

Furnace temperature is an important component in its combustion control. The knowledge of 3-D temperature profile of the furnace would impact the furnace control system in improving furnace thermal efficiency and product quality.

Although many different types of furnaces exist, furnace temperature distribution measurements are especially important in all cases in optimizing furnace operation and indirectly impacting product quality. The high temperature furnace environment is a great challenge for most conventional types of temperature instrumentation. Not only the instrument must be able to withstand high temperature and radiation, it must supply 2-D or 3-D temperature distribution reliably to be comparable with advanced instrumentations for temperature measurement such as cameras.

Thermal imaging is a promising method of non-contact temperature measurement for generating a 2-D temperature distribution. Thermal imaging using infrared (IR)

thermography [14] and charge coupled device (CCD) camera are also the fastest-growing segment of the temperature sensor market. The widespread technique used in the industry for temperature measurement is based on infrared (IR) or near-IR technology. However, the main disadvantages of IR thermography are its high cost, the low resolution of the sensors and the lack of image processing supports: edge detection, shape and filtering (linked with the poor spatial resolution). [15][16]

The invention of the CCD in the mid seventies was the breakthrough for semiconductor imaging devices [17]. The CCD technique overcomes the disadvantage of IR thermography and provides many benefits for temperature distribution measurement, including low cost, high spatial resolution, and the possibility of real-time implementation.

Most recent researchers have employed the CCD camera for temperature measurements and still have focused on the IR wavelength region by installing the IR or near-IR(NIR) filters on the front of the CCD camera. The researchers choose the filter with different bandpass wavelengths in their experiments for capturing the radiation image, for example, 490nm and 531nm filters for oil-fired flames, 950nm and 10nm filters for the steel industry,[18] 600 nm and 700 nm filter for coal fired utility boiler,[19] , 600 and 700nm filters for a simulated gas turbine,[20] 500nm and 600nm filters for gas-fired furnace[21-25], 400 nm and 720nm filters for soot temperature measurement[26], a single 550nm filter for evaporation surface heated by swept electron beam[27]. If the optical bandpass filter is placed at a particular wavelength, 2-D monochromatic image will be obtained. To determine the flame temperature, the ratio between the spectral intensities at the two wavelengths for each pixel is calculated and the temperature is

calculated based on the ratio. Because it is produced by the CCD camera based on the luminance at two wavelengths, the captured image has a low quality. The filter selection and installation increase the experiment cost and its complexity. At the same time, it greatly discounts the benefit of the CCD camera for temperature measurement.

Except for measuring the temperature distribution, the CCD system also can be applied into characterizations and classification of flames [28-29], thermal part classifications [30], target size [31], Emissions of Nox and unburned carbon [32-33], temperature distribution of silver breaking arc [34], fire flame detection [35].

In this work, the CCD system didn't utilize any filters for the data acquisition. That system using the visible region for temperature calculations, as developed here, can provide additional benefits such as the availability of image processing, and image reconstruction.

## 1.2    Overview of Temperature Measurement by the CCD Camera System

The integral flame temperature measurement consists of an optical probe, a CCD camera, frame grabber, a computer and associated software. The schematic diagram of the temperature monitoring system is shown in Fig. 1.1. To protect the CCD camera and its accessories from excessive heat in the furnace, an optical probe shielded with a water-cooled jacket is deployed to distance the camera from the furnace wall (See Fig. 1.2a). The objective lens of the probe has a 90-degree view angle. The cool water protects it from the heat and a jet of air is blown to avoid dust pollution. The CCD camera is installed in the steel shell cooled by water (See Fig 1.2b). The iris controller connected with the camera adjusts the light intensity captured by the CCD camera.
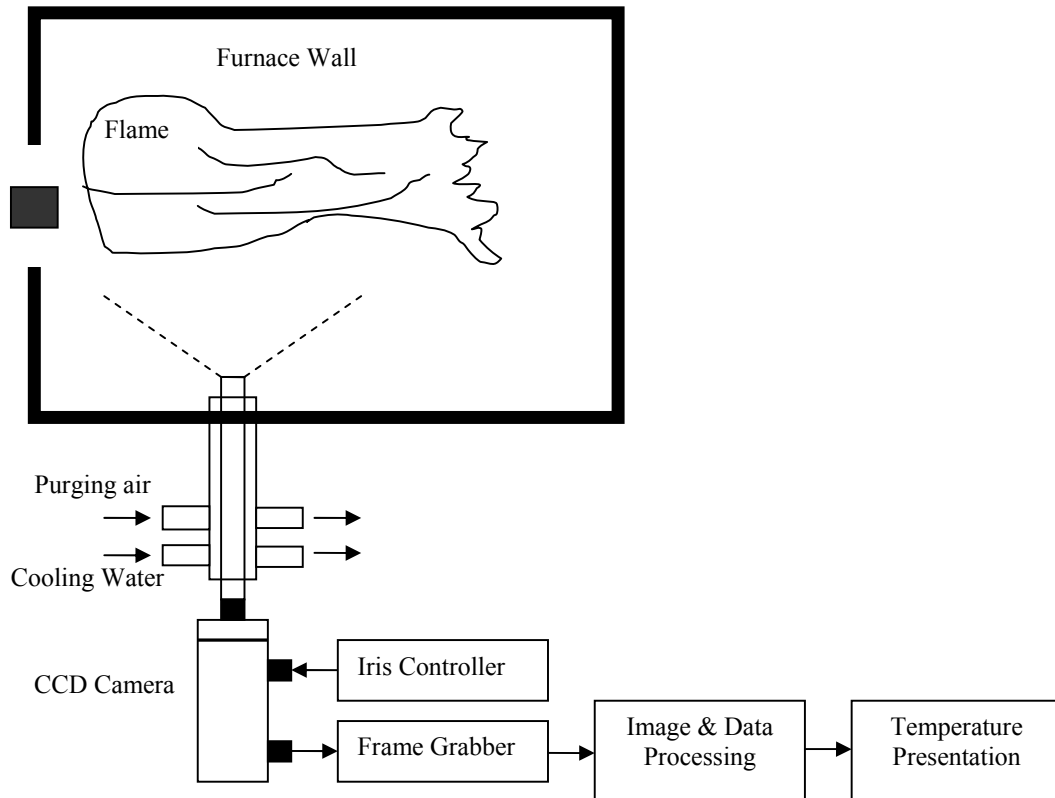
**Figure 1.1 Temperature Monitoring System by CCD Camera**



(a)                                                        (b)

**Figure 1.2 Steel Shell Installed with CCD Camera**

Luminance of combustion flames detected by the lens is converted to electrical signals by the CCD camera and recorded on video tape which can be simultaneously monitored with the LCD screen.

The CCD camera is highly suited to making luminance measurements, and with some adjustment or modification, a standard camera can be made to operate

satisfactorily. There are some requirements for the camera. First, it must respond linearly to light input, which is achieved on most cameras by setting the coefficient of gamma correction to 1.0. The camera output must be stable over long periods of time so that frequent calibration is not required. Lastly, it is preferable that the camera incorporates some type of programmable or fixed gain to improve response at low luminance. [36]

The two-color algorithm is applied for temperature calculations based on the captured image frame. The three-dimensional temperature profiles are supplied by combining the camera calibration technology and temperature calculations. Fig 1.3 illustrates the flowcharts for temperature profile calculation model.
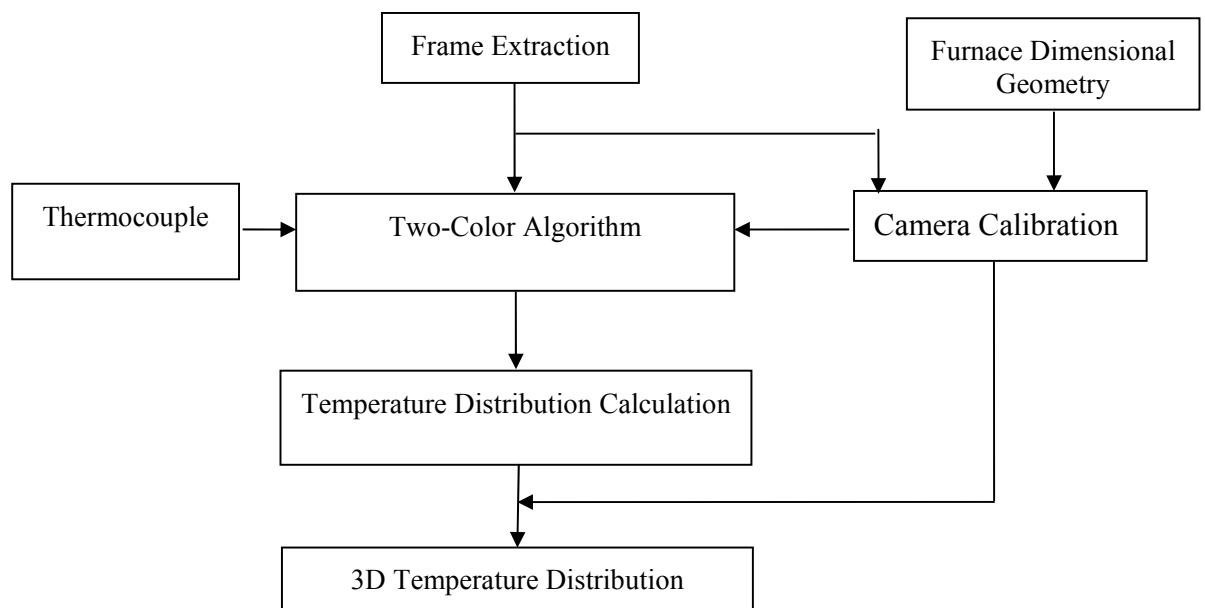


**Figure 1.3 Flowcharts for Temperature Profile Calculation Model**

## 1.3    Overview of Dissertation

The research work presented in this dissertation utilizes the CCD camera for capturing the image of the flame and wall and also introduces several novel visual color

imaging methods for calculating the flame or wall temperature profiling applied in several experiments in the industrial furnace and burner. The new calculation methods are developed based on the two-color algorithm and RGB intensity in the image captured by the CCD camera. The two-color algorithm is derived into the reference method by the use of the single-point temperature measured by an infrared gun or thermocouples and the blackbody method based on the CCD camera response curve and flame adiabatic temperature. The camera calibration technology is also employed and combined with the calculation methods to calculate the temperature in the specified region and to produce the three-dimensional temperature profiling. According to the CCD camera theory, an ISO RGB color space is introduced and applied into the two-color method for calculating the temperature. Experimental results indicate that these methods yield accurate results that are well matched with the IR gun reading and thermocouple records. The new model has great potential for temperature measurement and furnace monitoring for application in the industry fields.

This dissertation is organized as follows: Chapter two presents the CCD camera system model. Chapter three describes the two-color blackbody algorithms. Two novel algorithm, reference method and camera response curve method, are developed. Chapter four describes the experiments and results in a pilot scale glass furnace. This chapter presents the wall and flame temperature calculated using two-color blackbody together with reference method and compares the results with the thermocouple reading recorded by the computer. In chapter five, the blackbody algorithm and reference method are applied to calculate the temperature distribution in an industrial gas-fired furnace. Chapter Six presents the camera calibration linear and non-linear model applied into the

basketball court experiments. Chapter seven presents the camera calibration model with the application for the temperature calculation and furnace dimension measurement. The conclusion from these experiments, future direction, and suggestions are discussed in chapter eight.

# 2. BACKGROUND

## 2.1    Electromagnetic Radiation

Since all materials above absolution zero (0° K) emit radiation based on the temperature of the material, this radiation may be used to find the temperature of the material.  This energy is in the form of electromagnetic radiation and consists of a width range of wavelengths.  The wavelength of visible light is roughly between 400nm and 700nm.  Infrared energy is the part of electromagnetic spectrum and behaves similarly to visible light.  The wavelength of IR energy is about an order of magnitude longer than visible light between 700 and 1,000,000nm.  Infrared is broken into three categories: near-, mid- and far-infrared.  Near-infrared refers to the part of the infrared spectrum that is closest to visible light.
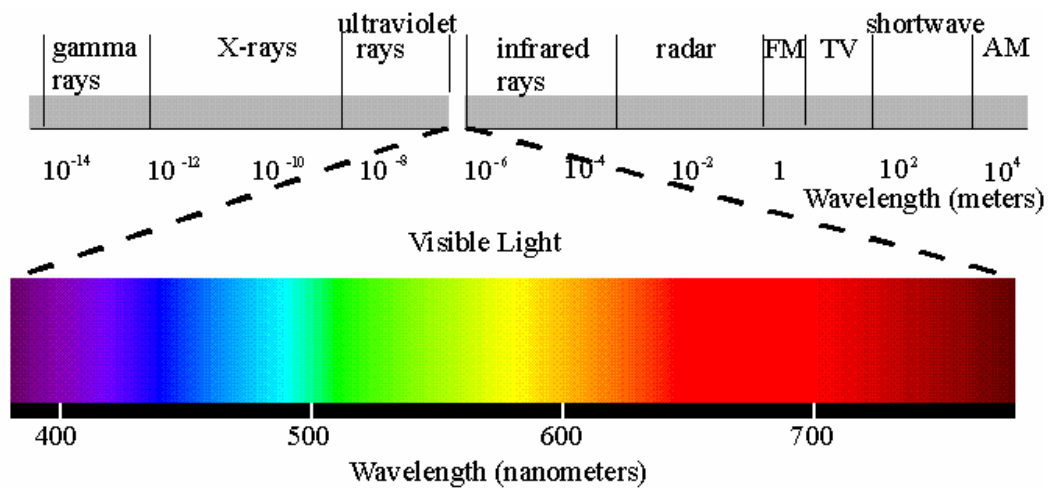


**Figure 2.1 Electromagnetic Spectrum**

### 2.1.1 Blackbody Radiation

The algorithm for calculating temperature in this research work is derived from the Planck's radiation law. Therefore, an understanding of the nature of blackbody radiation is essential.

A blackbody is an idealized object that absorbs all incident radiant energy, i.e. no energy is reflected from or transmitted through it. Since visible light is one form of radiant energy, no light is reflected from such an object, and it looks black (assuming that it is at a very low temperature). Hence it is called a blackbody. A blackbody is an idealized concept because no known material actually absorbs all the incident radiant energy. Only a small number of surfaces, such as carbon black and gold black (which consist of fine metal particles), absorb radiant energy to an extent close to a blackbody.

The temperature of an object which absorbs all the incident radiant energy rises higher and higher, unless the absorbed energy is transferred to the ambient environment. When the rate of energy absorption is equal to the energy dissipation, the object is said to reach thermal equilibrium with its environment. One path for thermal energy dissipation is through thermal radiation heat transfer. The thermal radiative properties of a blackbody have been studied extensively for many years. In 1901, Max Planck[37] derived the theoretical energy spectrum of blackbody radiation. Planck's blackbody radiation law can be expressed in many forms. Here the spectral radiance is expressed as a function of wavelength and absolute temperature:

$$E_\lambda(\lambda,T) = \frac{2C_1}{\lambda^5}\left(e^{C_2/\lambda T} - 1\right)^{-1} \qquad\qquad \text{EQ(2.1)}$$

where $C_1 = hc^2 = 0.59552 \times 10^{-16} Wm^2$ ,$C_2 = hc/k = 1.438769 \times 10^{-2} mK$ ,h $= 6.6260755 \times 10^{-34} Js$ is the Planck's constant, k $= 1.380658 \times 10^{-23} JK^{-1}$ is the Boltzmann

constant, c $= 2.99792458 \times 10^{8} \, ms^{-1}$ is the velocity of light in vacuum, and $E_{\lambda}(\lambda, T)$ is

the radiance at a given wavelength $\lambda$ and a given absolute temperature T. Figure 2.2

shows the spectral radiance of the blackbody at several temperatures. [17]
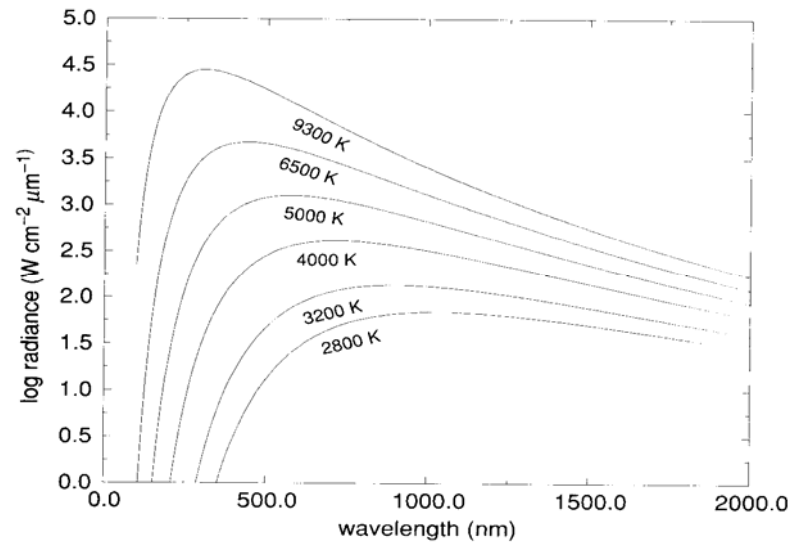


**Figure 2.2 Spectral Radiance Functions of Blackbody Radiators at Different Temperatures**

## 2.1.2 Non-Blackbody Radiation

Many substances reflect or transmit a portion of the incident radiation. Therefore,

the amount of radiation absorbed is less than complete, and the energy that is emitted will

be less than that for a blackbody emitter. A non-blackbody emitter will emit a fraction of

radiation compared to a blackbody emitter at the same temperature. This fraction is

termed the emittance or emissivity of the non-blackbody and may be dependent on the

wavelength of the emitted radiation. Thus, the emissivity is a measure of how close to

the maximum amount of radiation a body is capable of emitting. However, for flames,

the emissivity in the ultraviolet and visible regions is closer to zero. Once solid particles,

such as soot, appear in flames, the emissivity becomes closer to a black or "gray" body.

A gray body is such that the emissivity is not a factor of one, but varies only slightly with

wavelength [38]. It is reported [39] that the emissivity of soot does depend on temperature as well and can be given by:

$$\varepsilon_\lambda = 1 - \exp\left(-\frac{0.526SL}{\lambda T}\right)$$

where 'S' is the mole fraction of soot, L is the path length, $\lambda$ is the wavelength, and T is the temperature. There is some disagreement as to the actual constant listed above, and the power of the wavelength dependence is only one at the longer wavelengths and is closer to 1.39 for the wavelength range of 0.556-0.665 μm [40].

## 2.2 CCD Camera

The sensor, as well as other electronic components, plays a significant role in the performance of an imaging system. Understanding the terms used with the components will help understand the content in the later chapters.

Charge-coupled devices (CCDs) are the most common camera sensors used in machine vision applications. The CCD camera contains a silicon chip which consists of a matrix of light sensitive photosites called pixels. The CCD's popularity can be linked to its characteristically small size and light weight. Additionally, CCDs have an impressive dynamic range and yield a highly-linear relationship between the incoming energy and outgoing signal, making them ideal for metrology.

### 2.2.1 Spectral Response

Spectral response data are very important in identifying an IR-cut filter color reproduction algorithm, and other parameters to be sued in a CCD camera. Spectral response represents an image sensor output per incident light energy per wavelength in the range of spectrum where a CCD camera operates.[41] CCD chips have a characteristic response curve depending on the color of the light. Because different manufacturing

techniques are used for each array type, the spectral response varies with the manufacturer. For example, the Sony interline chips are more sensitive in the blue-green region of the spectrum and less sensitive in the red spectrum. The Kodak chip, however, is more sensitive in the red region. The spectral sensitivity of CCD sensors (quantum efficiency) is the percentage of photons converted to an electronic signal. The higher the quantum efficiency is, the more sensitive the CCD sensor. The spectral response is different for each CCD at every wavelength.

### 2.2.2 Monochrome CCD Cameras

The CCD chip is sensitive to wavelengths from ~350 to 1050nm, although the range is usually given from 400 to 1000nm. This sensitivity is represented in a spectral response curve (see Figure 2.2). Most high-quality cameras, like the Sony XC series, provide an infrared (IR) cutoff filter for imaging specifically in the visible spectrum. These filters are usually removable for near infrared imaging.
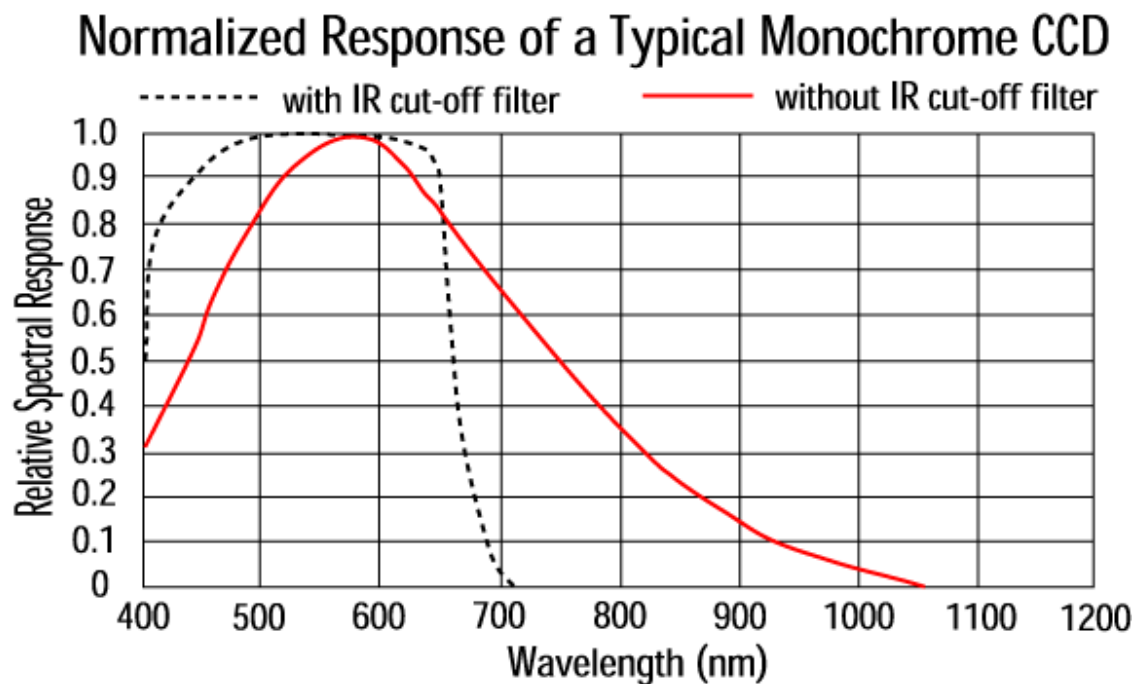


**Figure 2.3 Normalized Spectral Response Curve for a Typical Monochrome CCD Camera.**

### 2.2.3 Color CCD Cameras

The CCD silicon chip is based on a photoelectric effect and, as a result, cannot distinguish between colors. There are two types of color CCD cameras: single-chip and three-chip. The single chip offers a common, low-cost imaging solution and uses a mosaic filter to separate incoming light into a series of colors. Each color is directed to a different set of pixels (see Figure 2.4a). The precise layout of the mosaic pattern varies between manufacturers. Since more pixels are required to recognize color, the single-chip color CCDs inherently have lower resolution than monochrome cameras. The three-chip camera was designed to solve this resolution problem by using a prism to direct each section of the spectrum to a different chip (see Figure 2.4b). Three-chip cameras can offer extremely high resolutions but have lower light sensitivities and are costly.
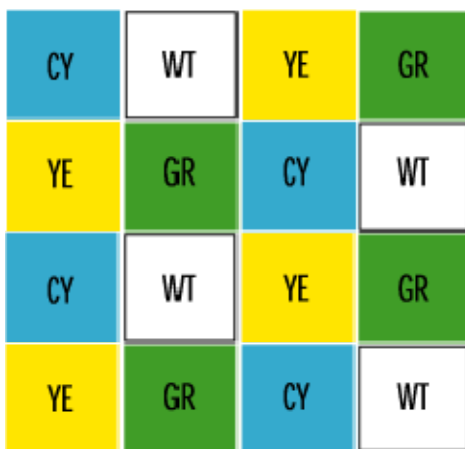


a) Single Chip Color CCD Camera:
This is an example of how a mosaic filter allots different colors to neighboring pixels.
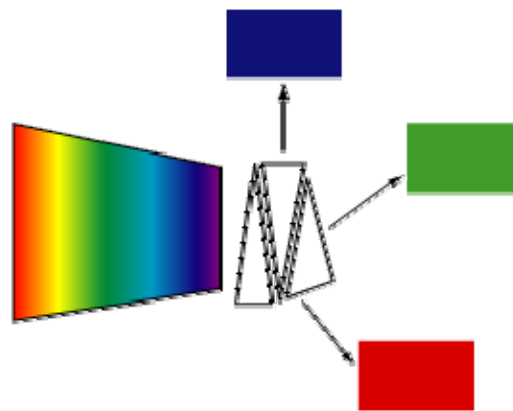
b) Three-Chip Color CCD Camera:
A prism is used to break up the incoming image into its red, green, and blue components.

**Figure 2.4 Methods for Filtering Color CCD Cameras**

The various CCD cameras are employed in the later experiment. Fig 2.5 shows the SONY CCD ICX084AK sensor response curve. The sensor is installed in the

MicroPix C640 CCD camera. From this sensor response curve, this sensor only receives the spectral energy from 400 to 700nm.
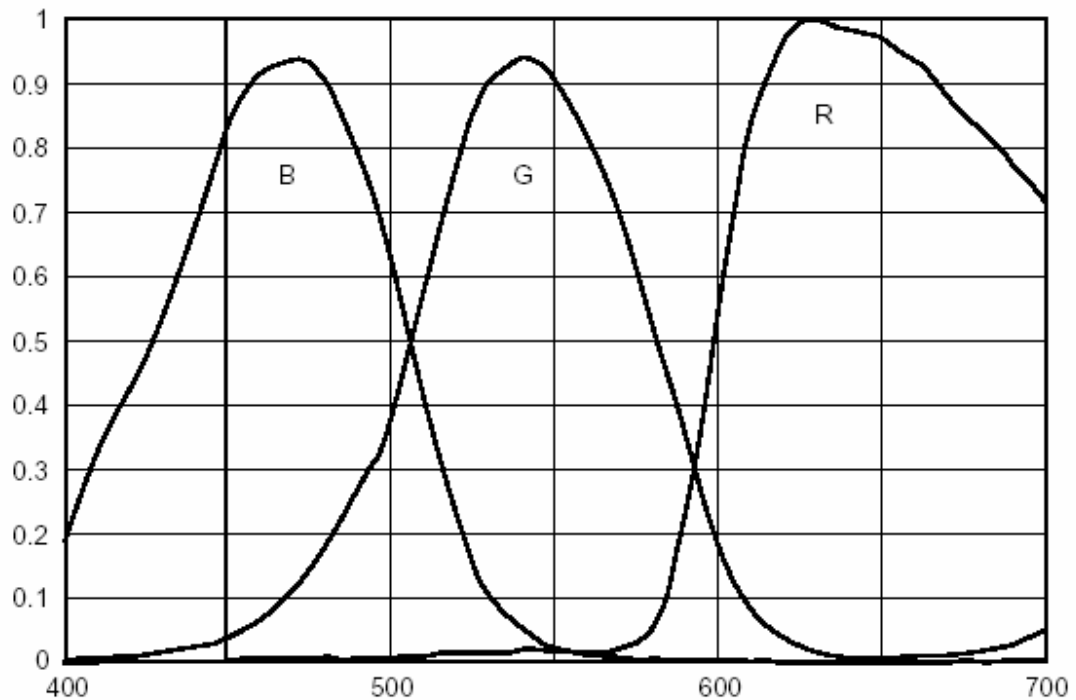


**Figure 2.5 Sony CCD ICX084AK Response Curve**

### 2.2.4    Interlaced vs. Progressive Scan

Conventional CCDs use interlaced scanning across the chip. The chip is divided into two fields: the odd field (rows 1, 3, 5..., etc.) and the even field (rows 2, 4, 6..., etc.). These fields are then integrated to produce a full frame. For example, with a frame rate of 30 frames per second, each field takes 1/60 of a second to read. For most applications, interlaced scanning will not cause a problem. Some trouble can develop in high-speed applications because by the time the second field is scanned, the object has already moved. This causes ghosting or blurring effects in the resulting image.

The progressive scan CCD solves this problem by scanning the lines sequentially (rows 1, 2, 3, 4..., etc.). The progressive scan output has not been standardized so care

should be taken when choosing hardware. Some progressive scan cameras offer an analog output signal, but few monitors are able to display the image. For this reason, capture boards are recommended to digitize the image for display.

### 2.2.5 Frame Rate vs. Shutter Speed

The frame rate refers to the number of full frames (which may consist of two fields) composed in a second. For example, the Panasonic GR-222 three-chip color camera has a frame rate of 30 frames/second (composed of two 1/60 second fields). In high-speed applications, it may be beneficial to choose a faster frame rate to acquire more "images" of the object as it moves.

The shutter speed corresponds to the "exposure time" of the CCD chip. The exposure time controls the amount of light incident on the chip. Camera blooming (over-exposure) can be controlled by decreasing illumination or camera gain or by increasing the shutter speed.

For example, the shutter speed on the Panasonic GR-222 three-chip color camera can be manually selected from 1/60 second (the chip would be exposed for the full fields) to 1/10,000 second (split-second exposure of the chip). Figure 2.6 illustrates the relationship between shutter speed, fields, and full frame.

In addition, the gain control helps in the amplification of the signal coming from the CCD chip. It should be noted that this amplifies the whole signal, including any associated background noise.[42] Most cameras have automatic gain (autogain or AGC), and some enable the user to turn it off and set it manually. The camera working in linear mode and 0 db gain will obtain the highest signal to noise ratio. [43]
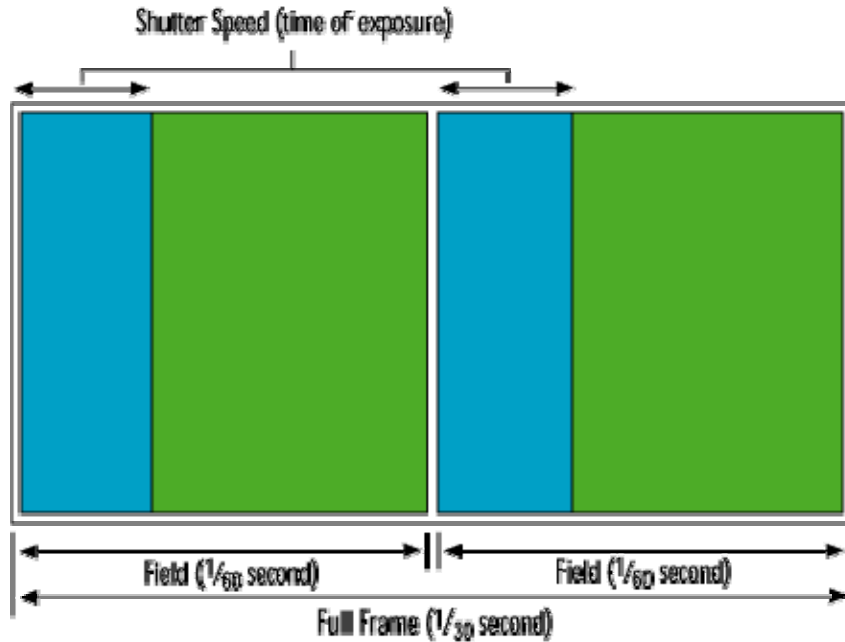
**Figure 2.6 Illustration of the Relationship Between Shutter Speed and Full Frame**

Furthermore, the gamma setting controls the grayscale reproduced on the image. CCDs have a linear response as long as gamma is set to 1. An image gamma of unity ($\tilde{a}=1$) would indicate that the CCD is precisely reproducing the object grayscale (linear response). A gamma setting much greater than unity results in a silhouetted image in black and white, while a gamma setting of much less than unity yields a soft gray image. Gamma can be seen as the ability to stretch one side (either black or white) of the dynamic range of the pixel. This control is often used in signal processing to raise the signal-to-noise ratio.

## 2.2.6     CCD Camera Response Model

The processing of digital color camera data (color correction, demosaicing, and image restoration) often depends on the assumption that the camera sensor responses are linear with respect to source intensity. This response linearity assumption is also closely related to the use of a single spectral sensitivity function to characterize how the camera responds to sources with different spectral power distributions.[44]

For the linear response model, the camera response for a pixel of the ith sensor type pixel is given by[44-48]

$$L_i(T) = e \int_{\lambda l}^{\lambda h} S_i(\lambda) E(\lambda, T) d\lambda + n_i \qquad \text{EQ (2.2)}$$

where $S_{\lambda i}$ is the spectral sensitivity of the $i_{th}$ sensor type, $E_{\lambda i}(\lambda)$ is the incident power density per unit time at wavelength λ, e is the exposure duration, and $n_i$ is a normal random variable. The mean and variance of $n_i$ describe the dark noise and response variability for the ith sensor type. The limits $\lambda_l$ and $\lambda_h$ are the wavelength limits beyond which the spectral response of the sensor is zero. Typically there are three sensor types (red, green, and blue) so that i = r; g; b. For red, green and blue, the equation 2.2 is derived into:

$$L_r(T) = e \int_{\lambda l}^{\lambda h} S_r(\lambda) E(\lambda, T) d\lambda + n_r \qquad \text{EQ (2.3)}$$

$$L_g(T) = e \int_{\lambda l}^{\lambda h} S_g(\lambda) E(\lambda, T) d\lambda + n_g \qquad \text{EQ (2.4)}$$

$$L_b(T) = e \int_{\lambda l}^{\lambda h} S_b(\lambda) E(\lambda, T) d\lambda + n_b \qquad \text{EQ (2.5)}$$

## 2.3    RGB Color Theory

The color flow of a digital image illustrated in Figure 2.7 can be generalized as follows.[49]  An image is captured into a sensor or source device space, which is device and image specific.  It may then be transformed into an unrendered image space, i.e.  a standard color space describing the original's colorimetry. In most workflows, however, the image is directly transformed from the source device space into a rendered image space, which describes the color space of some real or virtual output.  If the rendered

image space describes a virtual output, then additional transforms are necessary to convert the image into an output space, which is an output device specific color space. [50]
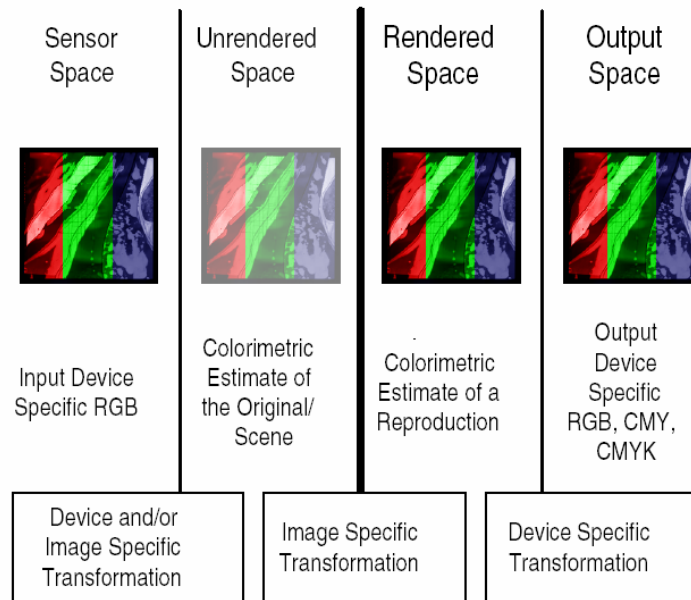


**Figure 2.7 Schematic Representation of a Digital Image Color Flow**

For example, a digital camera works in the following way: The light reflecting from the source is focused by the camera lens onto a charge coupled display (CCD)(sensor). The CCD passes along an analog electrical signal (unrendered color space) that gets sampled by an analog-to-digital converter. This digital signal (unrendered/rendered color space) is then passed through a processor that creates a digital photographic image. In doing so, the processor adjusts image properties such as contrast according to the requirements of the anticipated user, compressing the digital information. The camera output is RGB color intensity for each pixel.

Standard RGB color spaces will always describe either unrendered or rendered image spaces; most existing standard RGB color spaces fall into the category of rendered image spaces. Source and output spaces are always device specific.

### 2.3.1 Unrendered RGB Color Space

The transformation from sensor space to unrendered, device-independent space is image and/or device specific: linearization, pixel reconstruction (if necessary), and white point selection, followed by a matrix conversion (Figure 2.8). If the white point of a scene is not known, as is often the case in digital photography, it has to be estimated.[51]
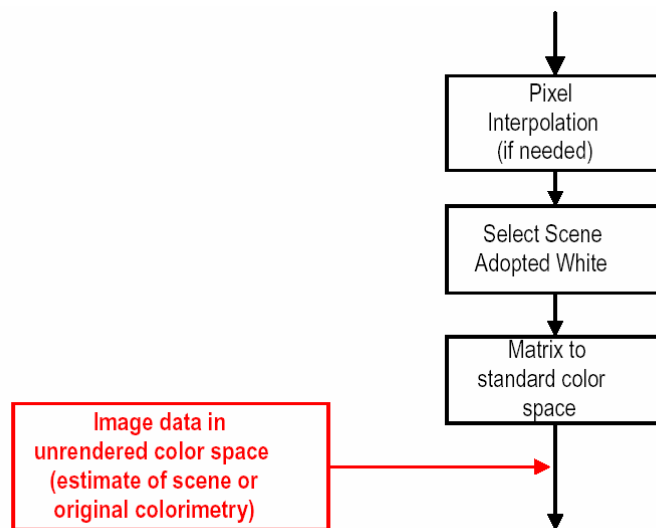


**Figure 2.8 Encoding From Sensor to Unrendered Space**

Unrendered images will need to go through additional transforms to make them viewable or printable. Appearance modeling can be applied when an equivalent or corresponding reproduction is desired, and the output medium supports the dynamic range and gamut of the original. In most applications, the goal is to create a preferred reproduction, meaning the image is optimized to look good on a specific medium with a different dynamic range and gamut than the original. In that case, a digital photography reproduction model is applied. Unrendered image spaces can be used for archiving images when it is important that the original colorimetry is preserved so that a facsimile can be created at a later date.

The advantage of unrendered image spaces, especially if the images are encoded in higher bit-depth, is that they can always be tone and color processed at a later date for all kinds of different rendering intents and output devices at a later date. The quality of the colorimetric estimate depends on the ability to choose the correct scene's adopted white point and the correct transformations.

Examples of unrendered color spaces that can describe an estimate of the scene's or original's colorimetry are ISO RGB, CIE XYZ, Photo YCC, and CIELAB.

There is currently only one unrendered RGB color space that is in the process of becoming a standard. ISO RGB is defined in ISO 17321 – Graphic Technology and Photography – Color characterization of digital still cameras using color targets and spectral illumination. ISO RGB is the reference color space to evaluate digital still camera color analysis. The transformations from sensor data to ISO RGB are defined in the ISO standard 17321.[51]

### 2.3.2    Rendered RGB Color Space

Rendered image spaces are color spaces based on the colorimetry of real or virtual output characteristics. Images can be transformed into rendered spaces from either source or unrendered image spaces. The complexity of these transforms varies: they can range from a simple video-based approach to complicated image dependent algorithms. The transforms are usually non-reversible, as some information of the original scene encoding is discarded or compressed to fit the dynamic range and gamut of the output. The transforms are image specific, especially if pictorial reproduction modeling is applied. The rendering intent of the image has therefore been chosen and may not be easily reversed. For example, an image that has been pictorially rendered for preferred

reproduction cannot be retransformed into a colorimetric reproduction of the original without knowledge of the rendering transform used. [52]

Rendered image spaces are usually designed to closely resemble some output device characteristics, ensuring that there is little loss when converting to the output specific space. Most commercial image applications only support 24-bit image encoding, making it difficult to make major tone and color corrections at that stage without incurring visual image artifacts. Some rendered RGB color spaces are designed so that no additional transform is necessary to view the images; in effect, the rendered RGB color space is the same as the monitor output space. For example, sRGB is a rendered image space that describes a real output and, as such, is equivalent to an output space.

A number of rendered RGB color spaces are used in different imaging applications and workflows today. For examples, sRGB is described by IEC 61966-2 as a default color space for multimedia applications. ROMM (Reference Output Medium Metric) RGB is a wide-gamut, rendered RGB Color Space. It was designed by Eastman Kodak. Apple RGB is based on the classic Apple 13" RGB monitor.

### 2.3.3 ISO RGB

The ISO's (the International Organization for Standardization) original RGB is currently only one unrendered RGB color space. [53]

With the increased popularity of electronic imaging devices comes a need for a default standard color space. For example, images captured with a digital camera have to be calibrated so that they can be displayed on a color monitor with good color and tone reproduction. Since cameras and monitors are manufactured by many different companies, the only way to make color reproduction feasible in the open system

environment is to set up a common default color space on which color images can be exchanged over different devices. For this purpose, sRGB was accepted by the International Electrotechnical Commission (IEC) and the International Standards Organization (ISO) as the default color space for multimedia applications.

The sRGB color space is based on the ITU-R BT.709 reference primaries (see Table 2.1).

**Table 2.1 the Chromaticity Coordinates of the ITU-R BT.709 Standard Phosphors**

| Stimulus | r | g | b | x | y | z |
|---|---|---|---|---|---|---|
| red phosphor | 1 | 0 | 0 | 0.64 | 0.33 | 0.03 |
| green phosphor | 0 | 1 | 0 | 0.30 | 0.60 | 0.10 |
| blue phosphor | 0 | 0 | 1 | 0.15 | 0.06 | 0.79 |
| white (illuminant D65) | 1/3 | 1/3 | 1/3 | 0.3127 | 0.3291 | 0.3583 |

The equi-energy ISO's original RGB (range from 0.0 to 1.0) can be transformed from CIE XYZ values by a matrix conversion. [54]

$$\begin{bmatrix} R_{Lin} \\ G_{Lin} \\ B_{Lin} \end{bmatrix} = \begin{bmatrix} 3.2410 & -1.5374 & -0.4986 \\ -0.9692 & 1.8760 & 0.0416 \\ 0.0556 & -0.2040 & 1.0570 \end{bmatrix} \begin{bmatrix} X \\ Y \\ Z \end{bmatrix} \qquad \text{EQ (2.6)}$$

The relationship between the ISO original RGB and sRGB (range from 0 to 255) is nonlinear. sRGB is the rendered color space. We can get sRGB from the ISO original RGB based on the following equations:

$$\text{if } R_{Lin} \leq 0.00304 \qquad R_{norm} = R_{Lin} \times 12.92 \qquad \text{EQ (2.7)}$$

$$\text{else if } R_{Lin} > 0.00304 \quad R_{norm} = 1.055 \times R_{Lin}^{1/2.4}\text{-}0.055 \qquad \text{EQ (2.8)}$$

$$R = R_{norm} \times 255 \qquad \text{EQ (2.9)}$$

Known:

R: Color intensity in sRGB

$R_{Lin}$: Color intensity in ISO original RGB

The above discussion indicates that the ISO original RGB(0.0-1.0) has a linear relationship with the energy and equi-energy transmission with XYZ. The conclusion can be drawn that the ISO original RGB (0.0-1.0) represents luminance in the flame image when calculating the temperature distribution instead of RGB(0-255).

# 3. Development of an Advanced Two-Color Method

For over forty years, scientists have used the two-color method to measure temperatures. Initially utilizing colored filters to limit the wavelengths to small ranges, the application of CCD camera allows this method to be used without employing these filters.

## 3.1    Two-color Method Description

The two-color method is a common method for the temperature measurement. Hottel and Broughton [4] are pioneers in using this two-color optical pyrometer to attempt to measure the true temperature and total radiation from the luminous gas flame temperatures in the furnaces.  The method has been expanded over recent years to flame temperature measurement in various applications such as the combustion engine [55], coal burner [20, 22, 29, 32, 33] , and steel furnace [18].

A blackbody radiator emits a continuous stream of thermal radiation from its surface.  This radiation forms a continuous spectrum though the intensity varies throughout the spectrum.  The radiance (or brightness) at every wavelength throughout the spectrum depends only on the blackbody temperature.  The radiance at every wavelength increases with the blackbody temperature.  These relationships are quantitively embodied in Planck's Law of blackbody radiation. [37]

As described in Chapter 2, the Planck's radiation law is:

$$E_\lambda(T) = \frac{C_1}{\lambda^5}\left(e^{C_2/\lambda T} - 1\right)^{-1}$$

EQ (3.1)

where λ is the wavelength of the radiation and $E_\lambda(T)$ is radiant energy at the specified wavelength λ.  T is the absolute temperature (K), and $C_1$ and $C_2$ are the first and second Planck's constants.

If the radiation wavelength of the flame is in the range from 400 to 700nm, and the temperature is below 3000 K, then

$$\left(e^{C_2/\lambda T} - 1\right)^{-1} \approx e^{-C_2/\lambda T}$$

EQ(3.2)

The Plank's radiant law (EQ 3.2) can be replaced by the Wien radiant law:

$$E_\lambda(T) = \frac{C_1}{\lambda^5} e^{\left(-\frac{C_2}{\lambda T}\right)}$$

EQ(3.3)

EQ (3.3) is for an idealized blackbody.  However, the furnace environment is not perfect and an additional term for emissivity, $\varepsilon_\lambda$ at the given wavelength, must be added to the equation.

$$E_\lambda(T) = \varepsilon_\lambda \frac{C_1}{\lambda^5} e^{\left(-\frac{C_2}{\lambda T}\right)}$$

EQ (3.4)

The two-color method of temperature measurement is based on the above equation EQ (3.4).  If the homochromy radiant energy $E_{\lambda 1}(T)$ and $E_{\lambda 2}(T)$ from the same position are calculated simultaneously with the wavelength $\lambda_1$ and $\lambda_2$:

$$E_{\lambda 1}(T) = \frac{C_1}{\lambda_1^5} \exp\left(-\frac{C_2}{\lambda_1 T}\right) \varepsilon_{\lambda 1}$$

EQ (3.5)

$$E_{\lambda 2}(T) = \frac{C_1}{\lambda_2^5} \exp\left(-\frac{C_2}{\lambda_2 T}\right) \varepsilon_{\lambda 2}$$

EQ (3.6)

The ratio of the two radiant energy equations (EQ 3.5 and 3.6) is as follows:

$$\frac{E_{\lambda 1}(T)}{E_{\lambda 2}(T)} = \frac{\dfrac{C_1}{\lambda_1^5} \exp\left(-\dfrac{C_2}{\lambda_1 T}\right)\varepsilon_{\lambda 1}}{\dfrac{C_1}{\lambda_2^5} \exp\left(-\dfrac{C_2}{\lambda_2 T}\right)\varepsilon_{\lambda 2}} \qquad \text{EQ (3.7)}$$

Derived from EQ (3.7), the temperature of that position can be determined by

$$T = \frac{C_2\left(\dfrac{1}{\lambda_2} - \dfrac{1}{\lambda_1}\right)}{\ln\dfrac{E_{\lambda 1}(T)}{E_{\lambda 2}(T)} - \ln\left(\dfrac{\varepsilon_{\lambda 1}}{\varepsilon_{\lambda 2}}\right) - 5\ln\left(\dfrac{\lambda_2}{\lambda_1}\right)} \qquad \text{EQ (3.8)}$$

Since it is not possible to directly measure the energy in the given wavelength, it is assumed that the energy is proportional to the color intensity at the specified wavelength:

$$\frac{E_{\lambda 1}(T)}{E_{\lambda 2}(T)} = A\frac{L_{\lambda 1}(T)}{L_{\lambda 2}(T)} \qquad \text{EQ (3.9)}$$

where $L_{\lambda 1}(T)$, $L_{\lambda 2}(T)$ are the color intensity under the wavelength $\lambda_1$, $\lambda_2$. A is the correction coefficient which is influenced by many factors, such as spectral sensitivity $S(\lambda)$ of the CCD camera, sensor measurement noise [47] etc.

Then derive EQ (3.8) based on EQ (3.9)

$$T = \frac{C_2\left(\dfrac{1}{\lambda_2} - \dfrac{1}{\lambda_1}\right)}{\ln\dfrac{L_{\lambda 1}(T)}{L_{\lambda 2}(T)} + \ln A - \ln\left(\dfrac{\varepsilon_{\lambda 1}}{\varepsilon_{\lambda 2}}\right) - 5\ln\left(\dfrac{\lambda_2}{\lambda_1}\right)} \qquad \text{EQ (3.10)}$$

EQ (3.10) is the basic equation for the two-color method. For the traditional R, G, B color channel, the wavelength $\lambda$ should be 700nm, 546nm and 435nm respectively [56]. For the luminance, the $L_{red\ \lambda=700nm}$, $L_{green\ \lambda=546nm}$, $L_{blue\ \lambda=435nm}$ can be read from the captured true color image.

Since the emissivity ε is hard to measure and the correction coefficient A is a comprehensive coefficient, the challenge is to resolve the correction coefficient A and emissivity ε in EQ (3.10).

In order to obtain the value of coefficient A, many methods and assumptions have been proposed by the recent researchers.  Gang etc. [57] employed the tungsten lamp as a standard temperature source to execute the calibration.  The calibration process needs the known true temperature and emissivity of the tungsten lamp.  They also assume that flame emissivity at different points of the flame are identical.  This results in some errors in the temperature distribution measurement.

Two methods are proposed and applied in the experiment: one named reference method based on the known temperature from the thermocouple or infrared (IR) gun; the other named blackbody methods based on the CCD cameras response curve;

## 3.2     Reference Methods

This method is based on the known temperature measured by the thermocouple or IR gun in the specified region.  The region where the thermocouples are installed or where the IR gun is pointed is regarded as the reference region.

This method is based on the assumption that the reference region has the similar emissivity as other regions to be calculated.  From the captured RGB image, the color intensity in the reference region is extracted as $L_R$, $L_G$, $L_B$ from the red, green and blue channel.  The red, green and blue colors are at the wavelength of 700.0, 546.1 and 435.0nm respectively.  Two of the three channels could be chosen to apply the two-color method.

Based on the known temperature $T_{known}$ and color intensity $L_R$, $L_G$, $L_B$ in the reference region, the correction coefficient is determined as:

$$A_{12} = \frac{L_2}{L_1} e^{\frac{C_2\left(\frac{1}{\lambda_2}-\frac{1}{\lambda_1}\right)+5T_{known}\ln\left(\frac{\lambda_2}{\lambda_1}\right)}{T_{known}}}$$

EQ (3.11)

For example, using the red and green channel to resolve the temperature:

$$A_{RG} = \frac{L_G}{L_R} e^{\frac{C_2\left(\frac{1}{\lambda_G}-\frac{1}{\lambda_R}\right)+5T_{known}\ln\left(\frac{\lambda_G}{\lambda_R}\right)}{T_{known}}}$$

EQ (3.12)

Correction coefficient A is employed in our previous calculation for temperature distribution. "A" is based on the reference temperature by thermocouple.

There are several disadvantages to the reference method. First, this method is dependent on the IR gun or thermocouple reading, but the IR gun reading is not accurate and the thermocouple has a low response as the common contact measurement method; secondly, it is difficult to precisely find the corresponding reference region in the image.

The procedure for calculating the temperature is as follows:

1. Measure the temperature by the thermocouples or IR gun.

2. Select the corresponding image pixel with the reference region in which the thermocouple is installed or IR gun is pointed to in the image.

3. Calculate the correction coefficient EQ (3.11) or (3.12) based on the known temperature, pixel location, and colors.

4. Calculate the temperature by EQ (3.10) based on correction coefficient.

## 3.3    Response Curve Method

This method is based on the relationship between the camera sensor response and source intensity. The camera sensor response is represented by response curve of the CCD camera and the source intensity indicates the color intensity in the image.

The processing of digital color camera data (e.g. color correction, demosaicing, and image restoration) often depends on the assumption that the camera sensor responses are linear with respect to source intensity. This response linearity assumption is also closely related to the use of a single spectral sensitivity function to characterize how the camera responds to sources with different spectral power distributions. [44]

If the CCD camera noise effect $n_i$ is ignored, the color intensity at the wavelength $\lambda_1$ and $\lambda_2$ in EQ (2.2) becomes:[47]

$$L_1(T) = e\int_{\lambda l}^{\lambda h} S_{\lambda 1}(\lambda)E(\lambda, T)d\lambda \qquad \text{EQ (3.13)}$$

$$L_2(T) = e\int_{\lambda l}^{\lambda h} S_{\lambda 2}(\lambda)E(\lambda, T)d\lambda \qquad \text{EQ (3.14)}$$

The ratio of $L_1(T)$ and $L_2(T)$ is:

$$\frac{L_1(T)}{L_2(T)} = \frac{\int_{\lambda l}^{\lambda h} S_{\lambda 1}(\lambda)E(\lambda, T)d\lambda}{\int_{\lambda l}^{\lambda h} S_{\lambda 2}(\lambda)E(\lambda, T)d\lambda} \qquad \text{EQ (3.15)}$$

The response curve could be obtained from the CCD camera manufacturer. Figure 3.1 shows the response curve for the CCD sensor SONY ICX084AK which is installed in CCD camera MicroPix C640. This camera is one of those utilized for data acquisition in this work. Appendices 1-4 describe various cameras utilized in this work.
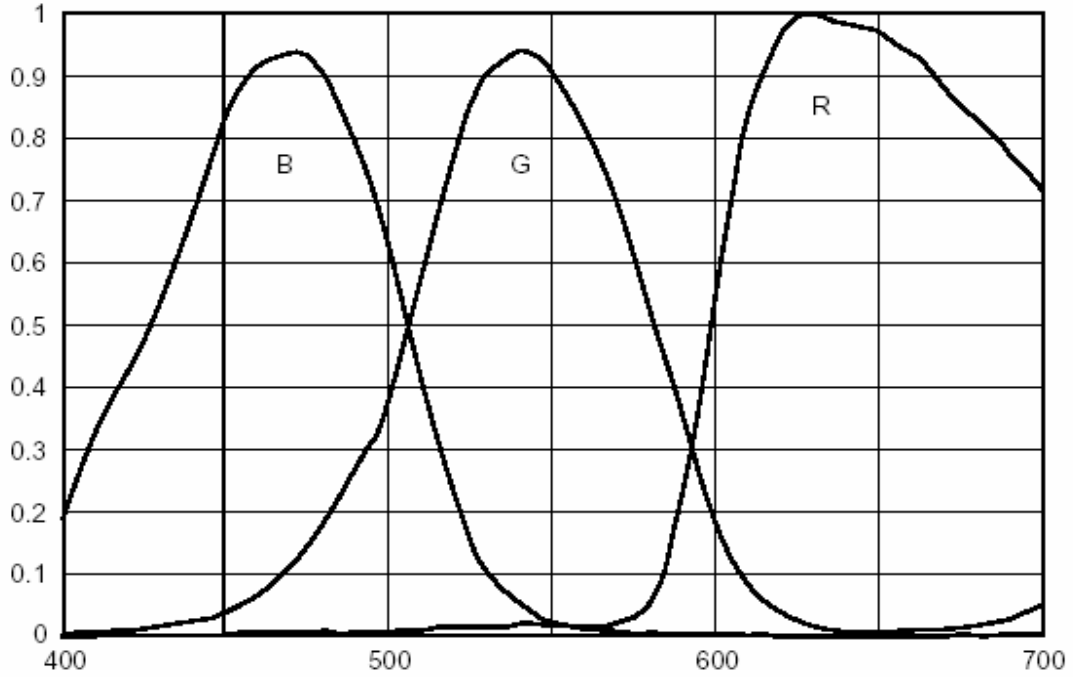
**Figure 3.1  CCD SONY ICX084AK Response Curve**

Based on the above response curve, the limits $\lambda_l$ and $\lambda_h$ are set to 400 and 700nm.  Since the function for the response curve is unknown, the integral in EQ (3.15) can be resolved by setting $d\lambda = \Delta\lambda$, and at a $\Delta\lambda$ nm interval, therefore the EQ (3.15) becomes

$$\frac{L_1(T)}{L_2(T)} = \frac{\sum_{\lambda_l=400}^{\lambda=700} S_1(\lambda)E(\lambda,T)}{\sum_{\lambda_l=400}^{\lambda_h=700} S_2(\lambda)E(\lambda,T)} \qquad \text{EQ (3.16)}$$

For gaseous flames, the size of the soot varies from 0.005 to 0.1 μm [58] and is much smaller than the wavelengths of observation.  Flower [59] proved that, when assuming the soot particles in the flame are homogeneous, optically thin, isothermal along a horizontal line, and small relative to the used wavelength, the spectral emissivity is inversely proportional to the wavelength. It is also proved by Grosshandler [60], i.e.

$$\varepsilon_\lambda = 1/\lambda \qquad \text{EQ (3.17)}$$

Another formulation for a gaseous flame in the Flower's study [59] is obtained by using

$$\frac{\varepsilon_{\lambda 1}}{\varepsilon_{\lambda 2}} = \frac{\lambda_2}{\lambda_1}$$

EQ (3.18)

EQ(3.13) and EQ(3.18) are put into EQ (3.10):

$$T_{known} = \frac{C_2\left(\frac{1}{\lambda_2} - \frac{1}{\lambda_1}\right)}{\ln\frac{\sum\limits_{\lambda_l=400}^{\lambda_h=700} S_1(\lambda)E(\lambda,T_{known})}{\sum\limits_{\lambda_l=400}^{\lambda_h=700} S_2(\lambda)E(\lambda,T_{known})} + \ln A - 6\ln\left(\frac{\lambda_2}{\lambda_1}\right)}$$

EQ (3.19)

where $L_{\lambda 1}$(T), $L_{\lambda 2}$(T) are the color intensities captured by the CCD camera based on two wavelengths $\lambda_1$, $\lambda_2$; $S_1$ and $S_2$ are the spectral sensitivity of the CCD camera at wavelengths $\lambda_1$, $\lambda_2$; and $T_{known}$ is the blackbody temperature which is assumed equal to the known flame adiabatic temperature.

The correction coefficient A will be resolved from EQ (3.19)

$$A_{12} = \frac{\sum\limits_{\lambda_l=400}^{\lambda_h=700} S_2(\lambda)E(\lambda,T_{known})}{\sum\limits_{\lambda_l=400}^{\lambda_h=700} S_1(\lambda)E(\lambda,T_{known})} e^{\frac{C_2\left(\frac{1}{\lambda_2}-\frac{1}{\lambda_1}\right)+6T\ln\left(\frac{\lambda_2}{\lambda_1}\right)}{T_{known}}}$$

EQ (3.20)

where 1 or 2 could be one of the color channel red, green, blue.

The temperature will be determined by

$$T = \frac{C_2\left(\frac{1}{\lambda_2} - \frac{1}{\lambda_1}\right)}{\ln\frac{L_1}{L_2} + \ln A_{12} - 6\ln\left(\frac{\lambda_2}{\lambda_1}\right)}$$

EQ (3.21)

The procedure for the response curve method is as follows:

1.  Known the flame adiabatic temperature as the blackbody temperature T

2.  Known the specified CCD camera sensor response curve $S(\lambda)$.

3.  Calculate the blackbody spectral energy from the lowest wavelength to the highest wavelength at the 5nm interval.  The lowest and highest wavelengths are determined by the CCD response curve.

 4.  Correction coefficient A is determined by EQ (3.20).

5.  Calculate the temperature by EQ (3.21)

# 4.  Laboratory Data Acquisition and Results

## 4.1      Pilot Scale Glass Furnace

The initial experiments were conducted in a 23 – 146 kW (0.16 Million Btu/hr) pilot scale glass furnace with the capacity of melting about 45 to 900 kg of glass per day. The furnace utilizes a single burner system with a turbulent diffusion flame.  Furnace design allows both air-gas and oxygen-fuel combustion with different burner types and burner arrangements, though only oxy-fuel was used for these experiments.  The control of the furnace is through a Labview hardware and software control system.  Three thermocouples were installed in the furnace and were connected with a central computer system to record all readings for temperatures.

The CCD camera system is set up to capture the flame and wall images at this glass furnace (See Figure 4.1).  The high-speed Panasonic GP KR-222 CCD camera was employed and installed in the silver steel shell.  This CCD camera is a 1/2" interline transfer CCD with 768 (H) x 494(V) pixels.  The electronic shutter of the camera is adjustable from 1/60 to 1/10000 second.  The detailed specification for this CCD camera is referred to in Appendix 1.  The lens with an adjustable iris and focus is installed on the front of the CCD camera.  The CCD camera is also connected with a 3-CCD SONY camcorder with the S-video cable.  The signals from the camera are recorded into the mini Digital Video (DV) tape by the camcorder.  The image files are extracted into an 8-bit color image with 720 by 480 pixels from the video tape by Adobe Premiere.

**Figure 4.1 CCD System Set-up at Pilot Scale Glass Furnace**

In this experiment, the temperature profiles of the flame are calculated using CCD by the two-color reference method based on reference temperature measured by the thermocouples. The different color combinations such as red/green, green/blue, and red/blue are examined for the flame temperature calculations in this experiment. After the flame is turned off, the wall temperature profile is calculated for the captured wall image. The calculated results are compared with the readings of three thermocouples installed in the furnace.

## 4.2 Flame Temperature Distribution

The following experiments are to calculate the flame temperature distribution based on the images captured by the CCD camera under the shutter speed of 1/60 second and the fixed lens iris(see Figure 4.2). The reference method (see chapter 3.2) is employed to calculate the temperature distribution and the reference region is chosen

from the image. The reference temperatures are measured by the thermocouple installed on the furnace wall and are recorded by the computer.



**Figure 4.2 Flame Image for the Pilotscale Glass Furnace**

The reference region is an area close to the thermocouple installed on the furnace wall. Table 4.1 lists the pixel locations, color intensities and reference coefficient for the reference regions on Fig. 4.2. Four by four neighboring pixels are sampled as the reference region. The reference temperature 1741.2 K measured by the thermocouple is used in calculating correction coefficient in table 4.1. The reference coefficient for each pixel is separately calculated based on the ratio of red/green, green/blue, and red/blue. For example, Arg in the table 4.1 presents the reference coefficient derived from red and green color channel. The mean and standard deviation for each reference coefficient are also calculated by the coefficients calculated for all selected pixels. The average coefficient is finally utilized for calculating the temperature distributions for the whole image.

**Table 4.1 Correction Coefficient by Sampling Pixels on Wall Region**

| Region | Pixel X | Pixel Y | Red/ Green | Green/Blue | Arg | Agb | Arb |
|---|---|---|---|---|---|---|---|
| 60.tif Thermocouple reading 1741.2 K | 390 | 90 | 2.0000 | 1.4000 | 4.0233 | 10.6444 | 42.8255 |
| | 391 | 90 | 1.9091 | 1.4667 | 4.2149 | 10.1606 | 42.8255 |
| | 392 | 90 | 2.0000 | 1.5000 | 4.0233 | 9.9348 | 39.9705 |
| | 393 | 90 | 2.0000 | 1.6154 | 4.0233 | 9.2251 | 37.1155 |
| | 390 | 91 | 2.1818 | 1.1579 | 3.6880 | 12.8700 | 47.4650 |
| | 391 | 91 | 2.1818 | 1.1579 | 3.6880 | 12.8700 | 47.4650 |
| | 392 | 91 | 2.3000 | 1.2500 | 3.4985 | 11.9217 | 41.7083 |
| | 393 | 91 | 2.4444 | 1.2000 | 3.2918 | 12.4185 | 40.8789 |
| | 390 | 92 | 2.4444 | 1.2000 | 3.2918 | 12.4185 | 40.8789 |
| | 391 | 92 | 2.2500 | 1.1765 | 3.5763 | 12.6668 | 45.2999 |
| | 392 | 92 | 2.3158 | 1.1875 | 3.4747 | 12.5492 | 43.6042 |
| | 393 | 92 | 2.3889 | 1.2000 | 3.3683 | 12.4185 | 41.8296 |
| | 390 | 93 | 2.0000 | 1.5714 | 4.0233 | 9.4832 | 38.1537 |
| | 391 | 93 | 1.9545 | 1.6923 | 4.1169 | 8.8058 | 36.2523 |
| | 392 | 93 | 2.0500 | 1.6667 | 3.9252 | 8.9413 | 35.0960 |
| | 393 | 93 | 2.0000 | 1.6154 | 4.0233 | 9.2251 | 37.1155 |
| **Mean A ± Standard deviation** | | | | | **3.7657± 0.3155** | **11.0346± 1.6054** | **41.1553± 3.7692** |

Based on the average coefficients listed in the above table, the temperature distribution is calculated using red and green channel with minimum average variation. Figure 4.3 presents the flame temperature distribution by the contour.
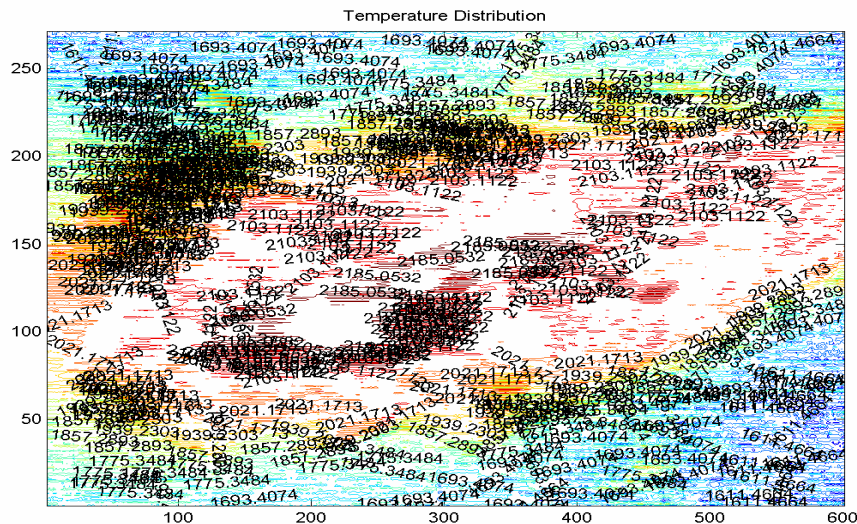


**Figure 4.3 Flame Temperature Distribution Presented by Contour**

Because Fig 4.3 can't present the temperature distribution clearly, the temperature distribution calculated by Red/Green color channel is illustrated in Fig 4.4 by the color

mapping. Figure 4.4 is composed of two images. The top image shows the flame image sampled from Fig. 4.2 and the bottom image shows the temperature distribution calculated based on the ratio of the red and green channel of the flame image.
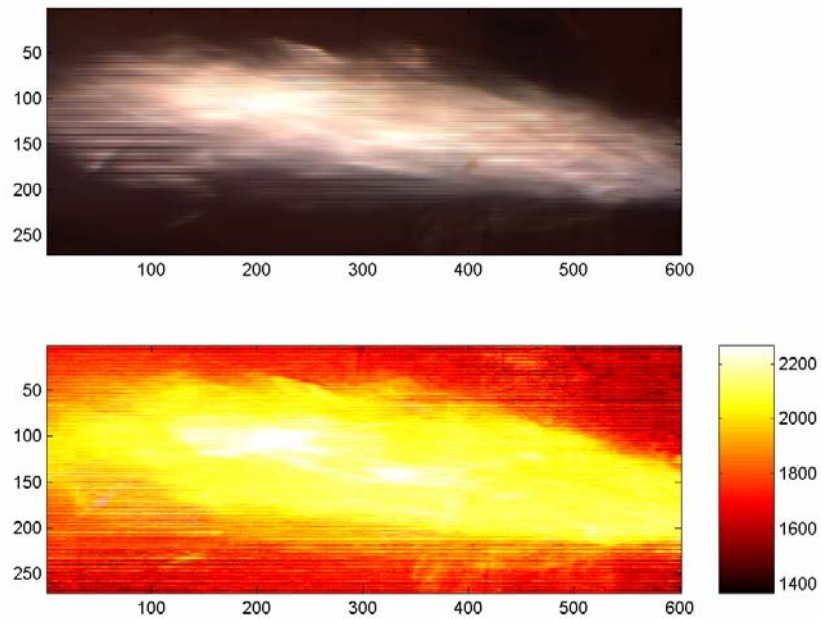


**Figure 4.4 Flame Temperature Profile by the Red / Green Channel**

According to the result in Figure 4.4, the reference method supplies the good result to calculate the temperature distribution based on the image intensities. The temperature varies from the 1400K to 2200K in Figure 4.4. The soot temperature is around 2000K. The highest flame temperature is about 2250K in Fig. 4.4. However, the actual maximum temperature is above 2250K because the actual temperature in white region can't be calculated due to the saturated color. The saturated color is caused when the brightness of the flame is beyond the capacity of the camera sensor sensitivity. The saturation color will be avoided by adjusting the iris or using wide-scope camera.

In order to investigate the influence of different color combinations, green/blue and red/blue channels are also utilized for flame temperature distribution calculations. Fig

4.5 and Fig 4.6 correspondingly present the flame temperature distribution based on green/blue and red/blue channel.
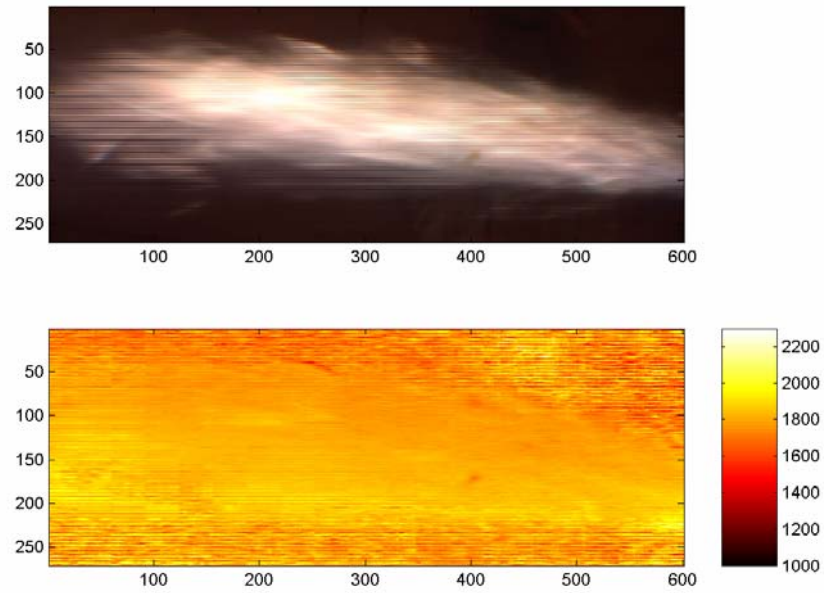


**Figure 4.5 Flame Temperature Profile by the Green / Blue Channel**
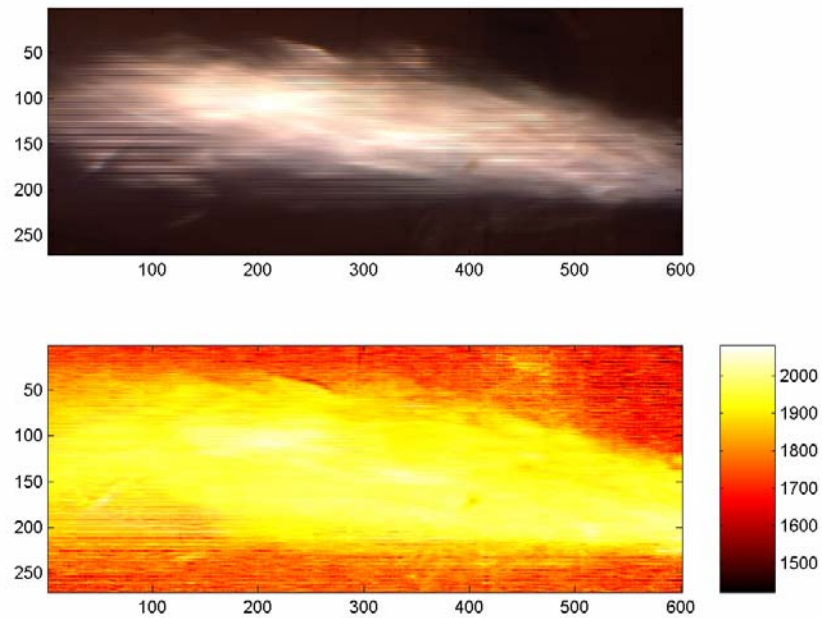


**Figure 4.6 Flame Temperature Profile by the Red / Blue Channel**

Fig 4.5 shows that the flame temperature in most locations is lower than the wall temperature. It is an unreasonable result. Presented in Fig 4.6, the flame profiling is not clear and the maximum flame temperature is 200 degree lower than the one in Fig 4.4. Rodney [61] investigates the spectrum ratio at different wavelengths by using the spectrometer and proposes that the ratio has the lower noise effect at 675nm and 540nm which is close to the wavelengths of red and green color. Compared with all results in Fig 4.4-4.6, it is verified that the temperature calculations by red/green will provide the best results.

## 4.3 Wall Temperature Calculation

The following work calculates the wall temperature change after the flame is turned off and demonstrates the response of the CCD measurement system to the change of the color intensity. As expected, the temperature was reduced gradually over time after the flame is turned off. Figure 4.7 shows the relationship between temperature variation and the time. The temperature is measured by the thermocouple which is connected to the computer for recording the data.
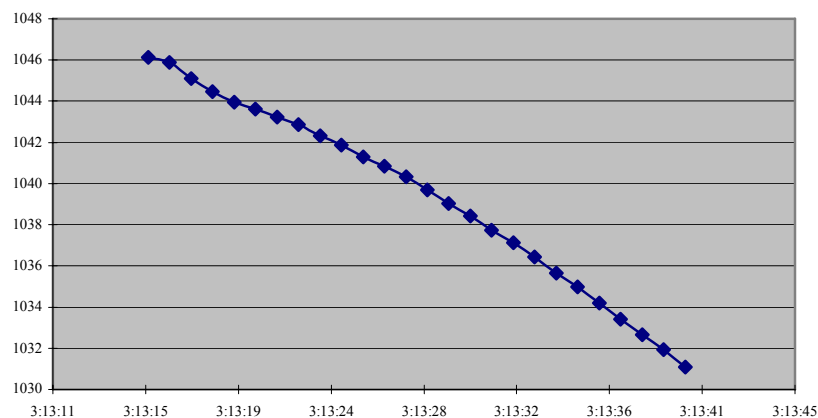


**Figure 4.7 Wall Thermocouple Temperatures vs. Time**

When the flame is turned off, a video with 30 frames per second (fps) is recorded by a SONY 3-CCD video recorder linked with the CCD camera. The sequence of video frames is extracted from at 5 seconds interval. Table 4.2 shows the information about the image captured time, image name, and the corresponding thermocouple temperature. The images with uncompressed TIF format are named with "B" as the initial letter connected with the frame ID. B001.tif, B150.tif, B300.tif, B450.tif, B600.tif and B750.tif are six images captured in 0, 5, 10, 15, 20 and 25 seconds after shutting off the flame. This sequence of images will be utilized for the wall temperature calculations.

**Table 4.2 Reference Temperature List for Different Images**

| Time | Image | Reference Temperature (K) |
|------|-------|---------------------------|
| 3:13:15 | B001.tif | 1319.3 |
| 3:13:20 | B150.tif | 1316.8 |
| 3:13:25 | B300.tif | 1314.5 |
| 3.13.30 | B450.tif | 1311.6 |
| 3.13.35 | B600.tif | 1308.1 |
| 3:13:40 | B750.tif | 1304.2 |

The cropped image is divided into eight regions with equal size. Region numbers are marked by the white color in Figure 4.8.
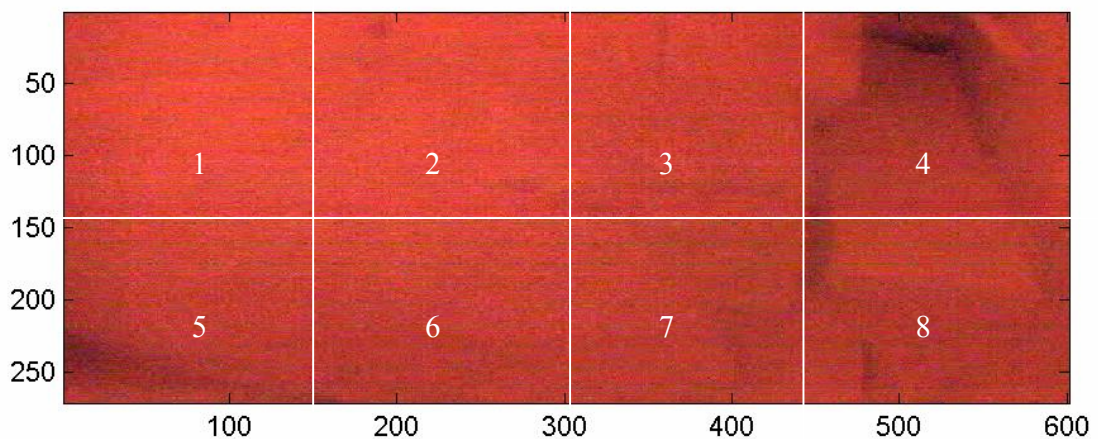


**Figure 4.8 Separated Regions on Furnace Wall**

The average temperature is calculated by the reference method based on the small image in each region (See Fig. 4.8). The thermocouple readings at the corresponding time are regarded as the reference temperature. Table 4.3 lists the reference temperature and the calculated average temperature and standard deviations at eight regions.

**Table 4.3 Average Region Temperature after Flame Turned Off**

| Image | B001.tif | B150.tif | B300.tif | B450.tif | B600.tif | B750.tif |
|---|---|---|---|---|---|---|
| Time | 3:13:15 | 3:13:20 | 3:13:25 | 3:13:30 | 3:13:35 | 3:13:40 |
| Ref. Temp | 1319.3 K | 1316.8 K | 1314.5 K | 1311.6 K | 1308.1 K | 1304.2 K |
| Area 1 | 1323.6 ±4.8 | 1319.8 ±4.9 | 1316.3 ±4.4 | 1311.7 ±4.5 | 1308.9 ±4.2 | 1303.7 ±4.2 |
| Area 2 | 1321.3 ±4.9 | 1318.4 ±4.8 | 1315.2 ±4.3 | 1310.8 ±4.5 | 1308.2 ±4.3 | 1303.1 ±4.2 |
| Area 3 | 1315.5 ±5.4 | 1313.3 ±5.6 | 1310.2 ±5.3 | 1306.2 ±5.2 | 1303.7 ±5.0 | 1298.9 ±4.9 |
| Area 4 | 1312.6 ±5.5 | 1312.2 ±5.2 | 1309.8 ±4.8 | 1306.0 ±4.8 | 1303.7 ±4.6 | 1298.8 ±4.6 |
| Area 5 | 1317.2 ±5.5 | 1314.1 ±4.7 | 1311.1 ±4.6 | 1307.4 ±4.4 | 1304.6 ±4.4 | 1299.8 ±4.2 |
| Area 6 | 1317.7 ±4.8 | 1314.0 ±4.5 | 1310.6 ±4.5 | 1307.0 ±4.4 | 1304.1 ±4.3 | 1299.2 ±4.2 |
| Area 7 | 1314.1 ±4.6 | 1311.7 ±4.2 | 1309.1 ±4.3 | 1305.6 ±4.2 | 1303.1 ±4.3 | 1298.4 ±4.0 |
| Area 8 | 1313.8 ±4.6 | 1311.7 ±4.4 | 1309.1 ±4.5 | 1305.6 ±4.3 | 1303.0 ±4.4 | 1298.5 ±4.2 |

Based on the region temperatures listed in table 4.3, Figure 4.9 illustrates the average temperature trend lines at each region verses the time.
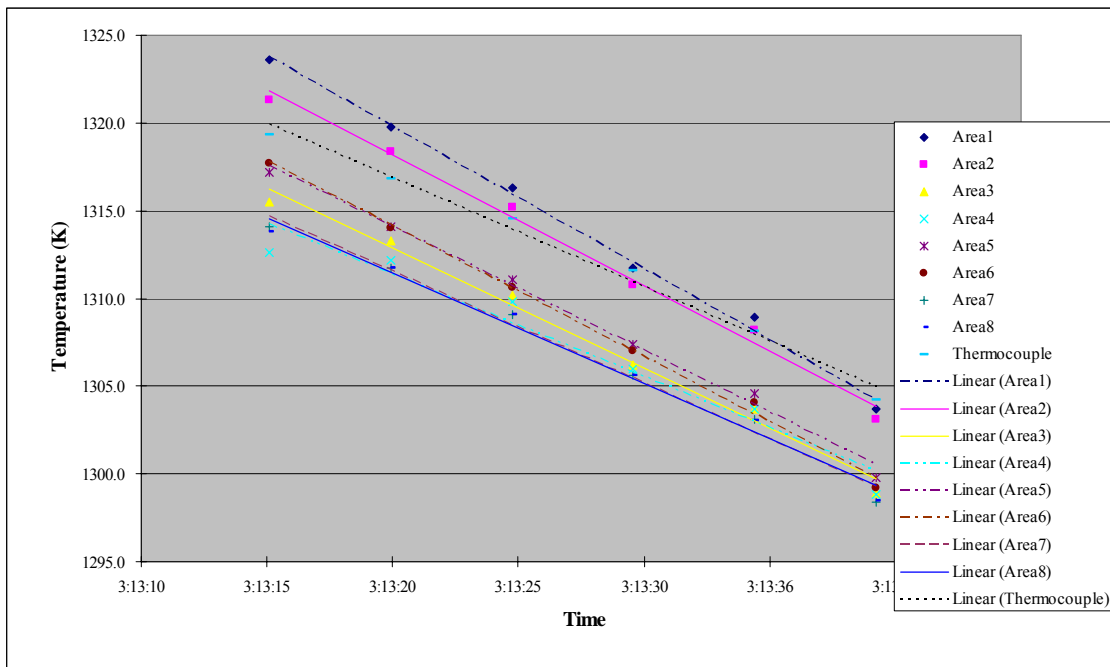


**Figure 4.9 Calculated Region Temperatures vs. Time**

The calculated region temperatures have a similar reducing trend as the thermocouple reading. However, the calculated wall temperatures trendlines show sharper gradient than the thermocouple one in the charts. It is the reason that the CCD image measurement system has real-time response and is more sensitive to temperature change. As illustrated in Fig 4.9, Area 1 and Area 2 have the higher temperature than other regions because these two regions are closer to the flame zone.

The above result is calculated based on one frame. In the following experiment, thirty continuous frames are utilized to calculate the average region temperature. Since the video is recorded by 30 frames per second, the result is average region temperature in one second. Table 4.4 presents the frames number and the average temperature for 30 frames.

**Table 4.4 Average Region Temperature for 30 Frames**

| Frames | B001-B030 | B150-B179 | B300-B329 | B450-B479 | B600-B629 | B750-B779 |
|--------|-----------|-----------|-----------|-----------|-----------|-----------|
| Time | 3:13:15 | 3:13:20 | 3:13:25 | 3:13:30 | 3:13:35 | 3:13:40 |
| Ref. Temp | 1319.3 K | 1316.8 K | 1314.5 K | 1311.6 K | 1308.1 K | 1304.2 K |
| Area 1 | 1317.1±5.0 | 1315.6±4.1 | 1312.9±3.5 | 1308.5±4.1 | 1305.3±3.9 | 1301.1±3.5 |
| Area 2 | 1315.1±4.4 | 1312.5±3.4 | 1309.8±2.8 | 1307.7±4.0 | 1303.9±3.7 | 1298.3±3.7 |
| Area 3 | 1313.5±4.6 | 1312.0±3.6 | 1310.6±3.2 | 1307.1±3.0 | 1303.3±4.2 | 1297.9±4.0 |
| Area 4 | 1313.5±4.9 | 1311.0±4.3 | 1307.9±5.0 | 1305.5±4.4 | 1302.0±3.5 | 1297.4±3.8 |
| Area 5 | 1317.4±4.7 | 1314.1±4.2 | 1312.5±4.4 | 1307.2±4.1 | 1305.3±3.0 | 1300.8±3.6 |
| Area 6 | 1315.1±5.0 | 1312.9±4.3 | 1311.6±4.3 | 1306.9±4.1 | 1303.9±2.9 | 1300.1±4.3 |
| Area 7 | 1313.2±5.2 | 1312.0±3.7 | 1311.6±4.4 | 1307.3±4.4 | 1304.8±3.4 | 1299.3±3.9 |
| Area 8 | 1313.4±5.0 | 1310.9±5.4 | 1309.0±4.3 | 1304.1±4.5 | 1302.0±4.2 | 1297.7±4.6 |

Based on the region temperatures listed in table 4.4, Figure 4.10 illustrates the average temperature trend lines at each region based on 30 frames verses the time.
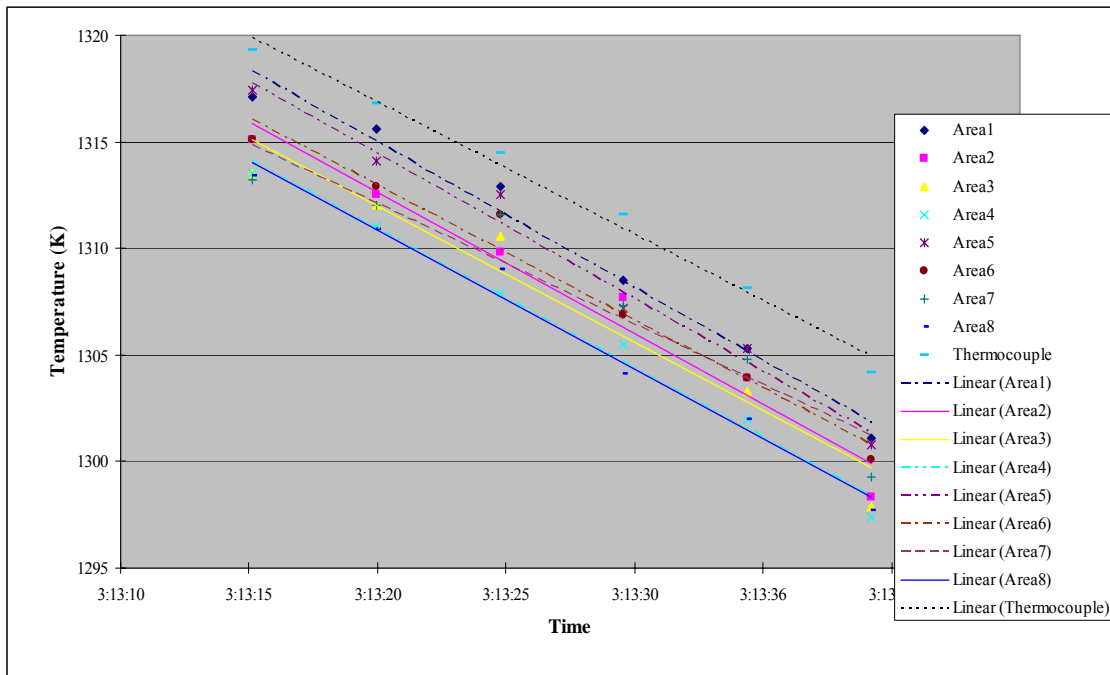


**Figure 4.10 Calculated Region Temperatures based on 30 frames vs. Time**

Compared with Figure 4.9, all trendlines in Fig. 4.10 almost have the same gradient based on the average results from 30 frames. It is the reason that averaging

technology reduces the noise for each frame. As Fig 4.9 illustrated, Area 1 and Area 2 have the higher temperature than other regions in Fig 4.10.

## 4.4    Reference Region Effect

As the above experiment, reference methods are successfully applied into the temperature calculation for flames and wall in the furnace. For the reference method, the selection of a reference region is determined by the accuracy of the temperature calculation. In the experiment, the three different regions are selected as the reference regions. The effect of the reference selection is investigated based on the calculated temperature results.

For the purpose of demonstration, Fig. 4.11 is the contrast-adjusted image based on the original image B001.tif which has the low color intensities. After the image is contrasted, the ratio between color channels is still kept constant.

Based on the image B001.tif, three different regions as the reference are chosen and marked with the numbering (See Fig. 4.11).  As mentioned above, there are three thermocouples installed in this furnace. These three regions are selected based on the installation locations of three thermocouples.

**Figure 4.11 Wall Image Marked With the Different Reference Region**

Table 4.5 – 4.7 pixel locations, color intensities and reference coefficient for three reference regions. The reference temperatures from the thermocouple readings are correspondingly 1323K, 1319K and 1226K for wall region 1, 2 and 3. 4 by 4 pixels in the image are selected as the reference region. The reference coefficient for each pixel is calculated based on the ratio of red and green and reference temperature. The average coefficient is finally utilized for calculating the temperature distributions based on the whole image. The values of average reference coefficient A in Table 4.5 (A = 26.1306) and Table 4.6 (A = 26.0538) are close each other because the reference temperatures are close in these two wall regions. The average reference coefficient in Table 4.7 (A = 35.7810) is greater than the above two.

**Table 4.5 Correction Coefficient by Sampling Pixels for Wall Region 1 in the Images**

| Region 2 | Position X | Position Y | Red / Green | A (RG) |
|---|---|---|---|---|
| B001.tif (Thermocouple reading 1323K) | 120 | 150 | 0.8765 | 26.2737 |
| | 121 | 150 | 0.8787 | 26.2103 |
| | 122 | 150 | 0.8792 | 26.1953 |
| | 123 | 150 | 0.8792 | 26.1953 |
| | 120 | 151 | 0.8708 | 26.4459 |
| | 121 | 151 | 0.8625 | 26.7014 |
| | 122 | 151 | 0.8625 | 26.7014 |
| | 123 | 151 | 0.8625 | 26.7014 |
| | 120 | 152 | 0.8987 | 25.6249 |
| | 121 | 152 | 0.9000 | 25.5889 |
| | 122 | 152 | 0.8992 | 25.6128 |
| | 123 | 152 | 0.8992 | 25.6128 |
| | 120 | 153 | 0.8917 | 25.8280 |
| | 121 | 153 | 0.8824 | 26.1007 |
| | 122 | 153 | 0.8792 | 26.1953 |
| | 123 | 153 | 0.8824 | 26.1007 |
| Average coefficient A ± standard deviation | | | | 26.1306±0.39 |

**Table 4.6 Correction Coefficient by Sampling Pixels for Small Region 2 in the Images**

| Region 2 | Position X | Position Y | Red / Green | A (RG) |
|---|---|---|---|---|
| B001.tif (Thermocouple reading 1319K) | 390 | 90 | 0.9050 | 25.7631 |
| | 391 | 90 | 0.9050 | 25.7631 |
| | 392 | 90 | 0.9046 | 25.7743 |
| | 393 | 90 | 0.9008 | 25.8813 |
| | 390 | 91 | 0.8852 | 26.3368 |
| | 391 | 91 | 0.8802 | 26.4888 |
| | 392 | 91 | 0.8802 | 26.4888 |
| | 393 | 91 | 0.8807 | 26.4740 |
| | 390 | 92 | 0.9091 | 25.6460 |
| | 391 | 92 | 0.9087 | 25.6566 |
| | 392 | 92 | 0.9083 | 25.6674 |
| | 393 | 92 | 0.9083 | 25.6674 |
| | 390 | 93 | 0.8857 | 26.3228 |
| | 391 | 93 | 0.8852 | 26.3368 |
| | 392 | 93 | 0.8848 | 26.3508 |
| | 393 | 93 | 0.8884 | 26.2424 |
| Average coefficient A ± standard deviation | | | | 26.0538±0.35 |

**Table 4.7 Correction Coefficient by Sampling Pixels for Wall Region 3 in the Images**

| Region 3 | Position X | Position Y | Red / Green | A (RG) |
|---|---|---|---|---|
| B001.tif (Thermocouple reading 1226K) | 660 | 160 | 0.9336 | 34.8793 |
| | 661 | 160 | 0.9378 | 34.7249 |
| | 662 | 160 | 0.9414 | 34.5898 |
| | 663 | 160 | 0.9414 | 34.5898 |
| | 660 | 161 | 0.9087 | 35.8349 |
| | 661 | 161 | 0.9053 | 35.9680 |
| | 662 | 161 | 0.9098 | 35.7907 |
| | 663 | 161 | 0.9098 | 35.7907 |
| | 660 | 162 | 0.8947 | 36.3946 |
| | 661 | 162 | 0.8975 | 36.2809 |
| | 662 | 162 | 0.8975 | 36.2809 |
| | 663 | 162 | 0.8980 | 36.2640 |
| | 660 | 163 | 0.8975 | 36.2809 |
| | 661 | 163 | 0.8980 | 36.2640 |
| | 662 | 163 | 0.8975 | 36.2809 |
| | 663 | 163 | 0.8975 | 36.2809 |
| Average coefficient A ± standard deviation | | | | 35.7810±0.68 |

Figure 4.12 – 4.14 correspondingly present the wall temperature distributions based on the reference region 1, 2 and 3. The temperature profile in Fig. 4.12 and Fig. 4.13 are pretty similar because reference coefficients A have the comparable value.
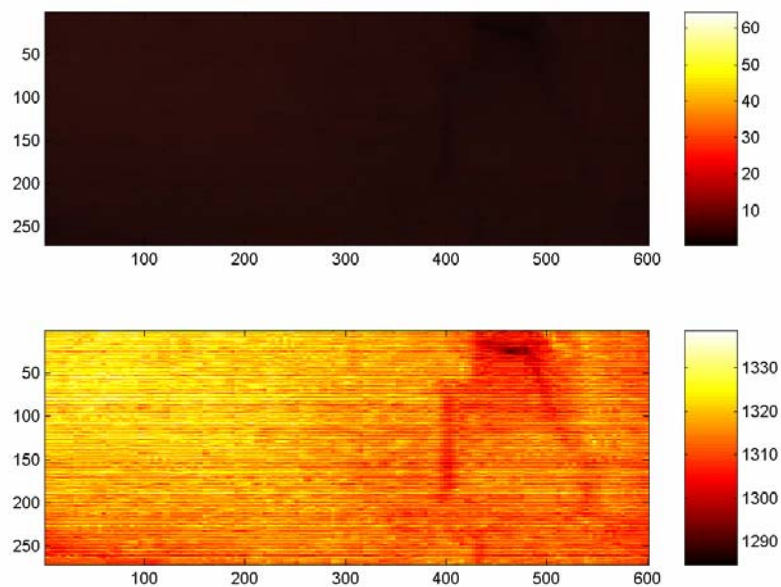


**Figure 4.11 Temperature Distribution Based on Region 1 as Reference**
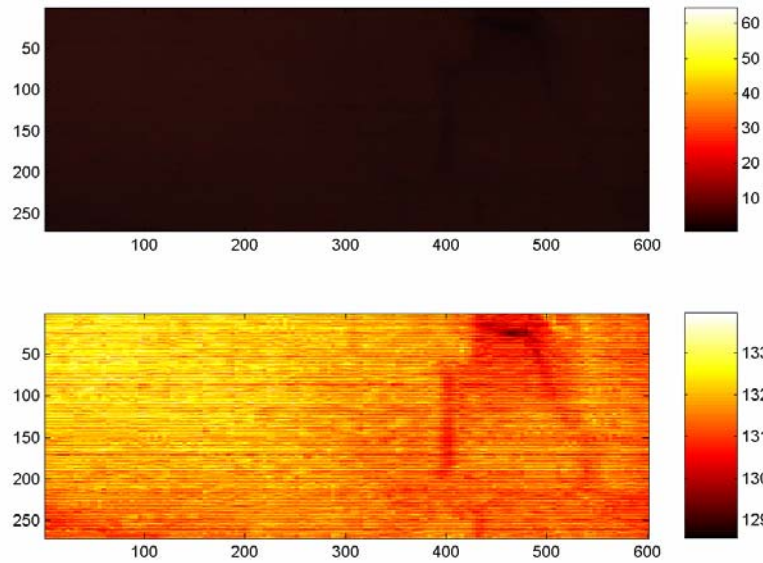
**Figure 4.12 Temperature Distribution based on region 2 as reference**
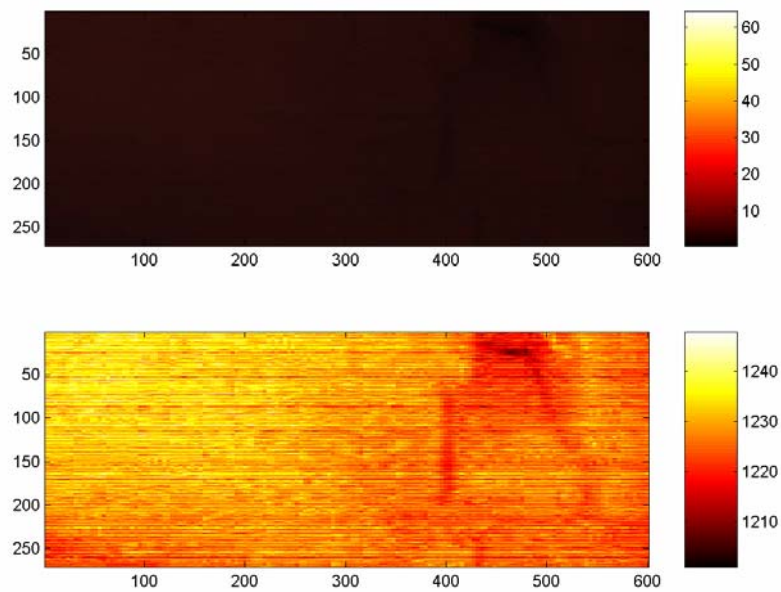


**Figure 4.13 Temperature Distribution based on region 3 as reference**

Based on the result in Fig 4.11 – 4.13, the maximum and minimum temperatures are listed in table 4.8. The corresponding pixel color and location are also presented in this table. The calculated temperatures near the thermocouple installation region are compared with the thermocouple readings. Based on the result on Fig 4.13, the calculated

temperatures Temp-3 on region 1 and region 2 are about 100K lower than the thermocouple readings on these regions. It is the reason that thermocouple 3 is inserted in the air in the furnace and the other two thermocouples are installed on the wall surface.

**Table 4.8 the Temperature Result Based on the Different Reference Regions**

|  | X | Y | Temp-1 (K) A=4.3785 | Temp-2 (K) A=4.4853 | Temp-3 (K) A=6.0952 |
|---|---|---|---|---|---|
| Thermocouple (Reference) |  |  | 1323 | 1319 | 1226 |
| Max Temperature | 2 | 58 | 1338.6 | 1339.5 | 1248.0 |
| Min Temperature | 24 | 479 | 1284.7 | 1285.6 | 1201.0 |
| Temp. around region installing other thermocouple |  |  | 1318 (T2) | 1324 (T1) | 1234 (T1) |
| Temp. around region Installing other thermocouple |  |  | 1313 (T3) | 1314 (T3) | 1230 (T2) |

Note: Temp-1 indicates temperature distribution based on region 1 as reference.

In the above experiment, reference method works well when the corresponding reference region in the image is precisely defined. The calculated result is as good as the accuracy of the method used to obtain the reference temperature, i.e. IR gun or thermocouple readings.

# 5. Commercial Data Acquisition and Results

Temperature monitoring in the glass furnace is critical in each stage of glass production. Real-time temperature monitoring will supply the important evidences for combustion stability and pollutant emission in the furnace. Therefore, in order to increase product quality and uniformity, it is important to measure wall temperature distribution in the furnace reliably and accurately.

After initial trials at laboratory facilities, the different methods are used to calculate temperatures in an industrial environment. All facilities are commercial multi-burner glass furnaces. In the first facility, the same CCD system applied in the laboratory furnace is set up to capture the image of the industrial furnace. The reference method is verified and applied for temperature calculations. In the second and final facility, the firewire CCD camera is employed for data acquisition. The novel response curve method is also proposed and applied to temperature calculations.

## 5.1    Multi-Burner Glass Furnace

The selected commercial furnace is a 179.4x106 kJ/hr multi-burner gas/air-fired used to produce float-glass. The furnace has six ports on each side with five ports containing paired burner jets and one port with a single burner jet. Two sets of six burners are used to produce the flame inside this industrial gas furnace. Both burner sets are activated alternatively in a cycle with duration of 20 minutes. A viewing port looking through the end wall was used to collect the data. The CCD camera system is installed to capture the images of the furnace walls or the flame (illustrated in Figure 5.1). A hand-held optical IR gun is used to obtain the temperatures in the same area of the furnace that is designated to monitor intensities and to calculate temperatures.

CCD camera is
installed in the shell

**Figure 5.1 CCD Camera System Installed in Industrial Furnace**

## 5.2     Wall Temperature Distribution in Furnace I with Panasonic Camera

The CCD system has the same equipment as the one applied in laboratory furnace in Rolla (see Chapter 4.1). The CCD camera Panasonic KP222 (see Appendix 1) is also employed for data acquisition in this industrial glass furnace.   The CCD camera is connected with 3-CCD SONY camcorder with the S-video cable.   The signals from the camera are recorded into the mini Digital Video (DV) tape by the camcorder.   The image files are extracted into 8-bit color image with 720 by 480 pixels from the video tape by Adobe Premiere.

### 5.2.1          Temperature distribution based on backwall reference

Figure 5.2 is captured when the flames from the left burners (right side in the image) are just turned off.   The reference method is employed to calculate the temperature distribution.   The temperature on the back wall in the furnace is 1735 K

measured by IR gun. The 4 by 4 reference pixels, shown by the white rectangle on Fig. 5.2, are used as the back wall region where IR Gun is pointed to.
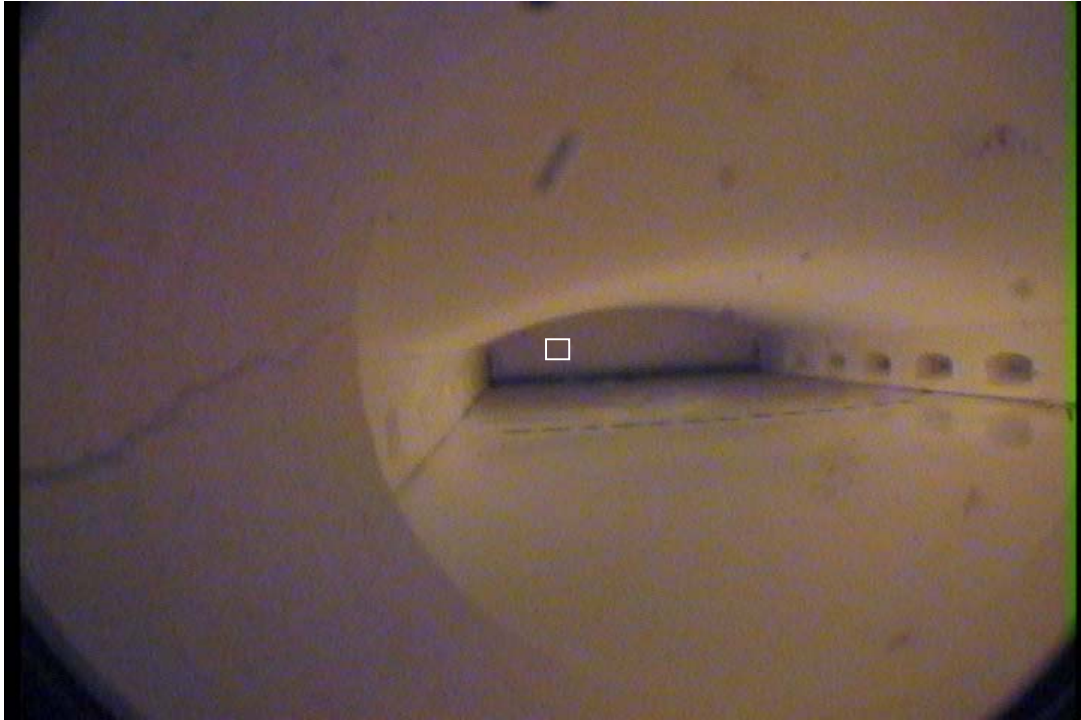


**Figure 5.2 Furnace Wall Image**

Table 5.1 demonstrates the reference pixels location, RGB color value and the corresponding correction coefficient. The correction coefficient $A_{rg}$ is calculated by the use of the ratio of red and green; $A_{gb}$ is calculated by the ratio of green and blue. The average coefficient is calculated based on 16 correction coefficients from each pixel.

**Table 5.1 Correction Coefficient Based on the Reference Pixels**

| Pixel Position | | Color Ratio | | Correction Coefficient | |
|---|---|---|---|---|---|
| X | Y | Red / Green | Green / Blue | $A_{rg}$ | $A_{gb}$ |
| 360 | 225 | 0.8678 | 0.9775 | 9.3831 | 15.4548 |
| 361 | 225 | 0.8693 | 0.9565 | 9.3669 | 15.7942 |
| 362 | 225 | 0.8707 | 0.9518 | 9.3511 | 15.8714 |
| 363 | 225 | 0.8729 | 0.9576 | 9.3282 | 15.7752 |
| 360 | 226 | 0.8418 | 0.9267 | 9.6730 | 16.3024 |
| 361 | 226 | 0.8522 | 0.9214 | 9.5542 | 16.3951 |
| 362 | 226 | 0.8531 | 0.9170 | 9.5449 | 16.4731 |
| 363 | 226 | 0.8522 | 0.9214 | 9.5542 | 16.3951 |
| 360 | 227 | 0.8882 | 0.9659 | 9.1674 | 15.6407 |
| 361 | 227 | 0.8793 | 0.9613 | 9.2605 | 15.7153 |
| 362 | 227 | 0.8813 | 0.9619 | 9.2390 | 15.7050 |
| 363 | 227 | 0.8813 | 0.9619 | 9.2390 | 15.7050 |
| 360 | 228 | 0.8563 | 0.9354 | 9.5091 | 16.1494 |
| 361 | 228 | 0.8742 | 0.9210 | 9.3137 | 16.4024 |
| 362 | 228 | 0.8742 | 0.9210 | 9.3137 | 16.4024 |
| 363 | 228 | 0.8757 | 0.9218 | 9.2986 | 16.3878 |
| Mean A | | | | 9.3810 | 16.0356 |

The temperature distribution is calculated based on the average $A_{rg}$ and $A_{gb}$. Fig 5.3 and Fig 5.4 separately presents the temperature distribution profile calculated by Red/Green ratio and Green/Blue channel.
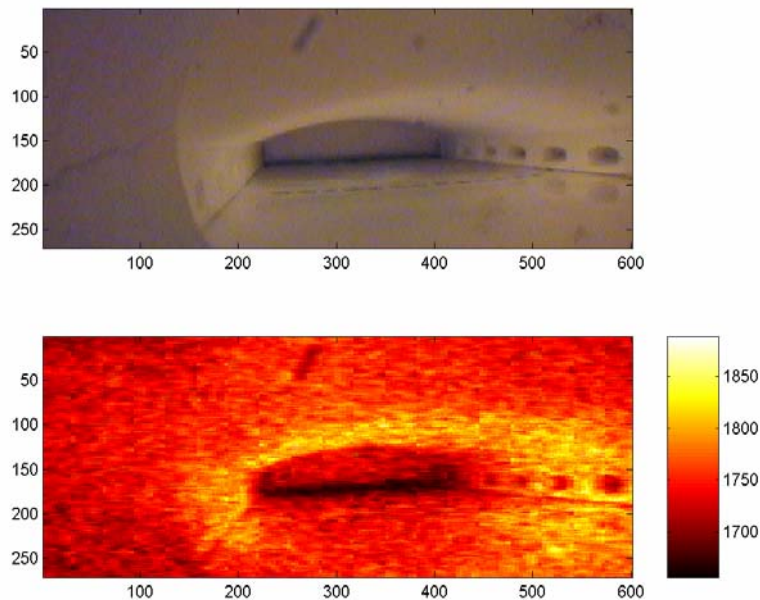


**Figure 5.3 Wall Temperature Distributions Calculated by Red / Green Channel**

**Figure 5.4 Wall Temperature Distributions Calculated by Green / Blue Channel**

Comparing the temperature results in Fig. 5.3 and Fig.5.4 with IR Gun reading in each burner region, Fig. 5.3 presented more reasonable results and clear temperature profile than Fig. 5.4. Therefore, red and green color channel employed in the reference method can obtain more accurate results than green and blue color channel do.

**5.2.2        Iris effect on the temperature calculation**

The iris switch is connected with CCD camera for controlling the light entering the camera. Fig 5.5 is the image captured with the same condition as Fig. 5.4, except for the increased iris position. This iris position allows more light to be captured by camera and results in a brighter image. The following experiment is to calculate the temperature distribution based on Fig. 5.5.

**Figure 5.5 Furnace Image Captured by CCD Adjusted with the Wide Iris Position**

Table 5.2 lists the reference pixel position, color intensity, correction coefficient and

average correction coefficient. Compared with Table 5.1, $A_{rg}$ and $A_{gb}$ value change

because of the ratio of the color intensities varies with the iris adjustment.

**Table 5.2 Correction Coefficient Based on the Reference Pixels on Fig. 5.4**

| Pixel Position | | Color | | Correction Coefficient | |
|---|---|---|---|---|---|
| X | Y | Red / Green | Red / Blue | $A_{rg}$ | $A_{gb}$ |
| 360 | 225 | 0.8841 | 0.8903 | 9.2107 | 16.9686 |
| 361 | 225 | 0.8986 | 0.8571 | 9.0622 | 17.6254 |
| 362 | 225 | 0.8986 | 0.8571 | 9.0622 | 17.6254 |
| 363 | 225 | 0.8986 | 0.8571 | 9.0622 | 17.6254 |
| 360 | 226 | 0.9420 | 0.8903 | 8.6439 | 16.9686 |
| 361 | 226 | 0.9191 | 0.8608 | 8.8594 | 17.5514 |
| 362 | 226 | 0.9254 | 0.8535 | 8.7995 | 17.7006 |
| 363 | 226 | 0.9248 | 0.8526 | 8.8048 | 17.7201 |
| 360 | 227 | 0.8993 | 0.9026 | 9.0548 | 16.7378 |
| 361 | 227 | 0.8944 | 0.8820 | 9.1046 | 17.1289 |
| 362 | 227 | 0.8929 | 0.8805 | 9.1199 | 17.1578 |
| 363 | 227 | 0.8921 | 0.8797 | 9.1278 | 17.1726 |
| 360 | 228 | 0.9058 | 0.8846 | 8.9897 | 17.0780 |
| 361 | 228 | 0.9051 | 0.8726 | 8.9965 | 17.3130 |
| 362 | 228 | 0.9051 | 0.8726 | 8.9965 | 16.9686 |
| 363 | 228 | 0.9058 | 0.8734 | 8.9897 | 17.6254 |
| Mean A | | | | 8.9928 | 17.3115 |

Figure 5.6 and Figure 5.7 correspondingly present the temperature distribution profile calculated by Red / Green and Green / Blue.



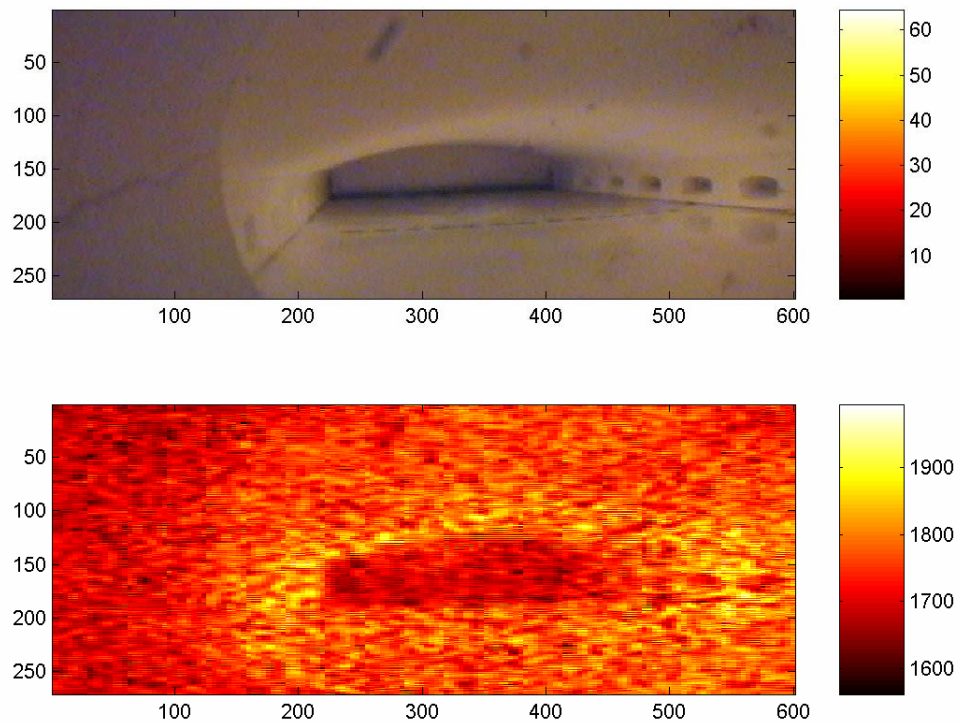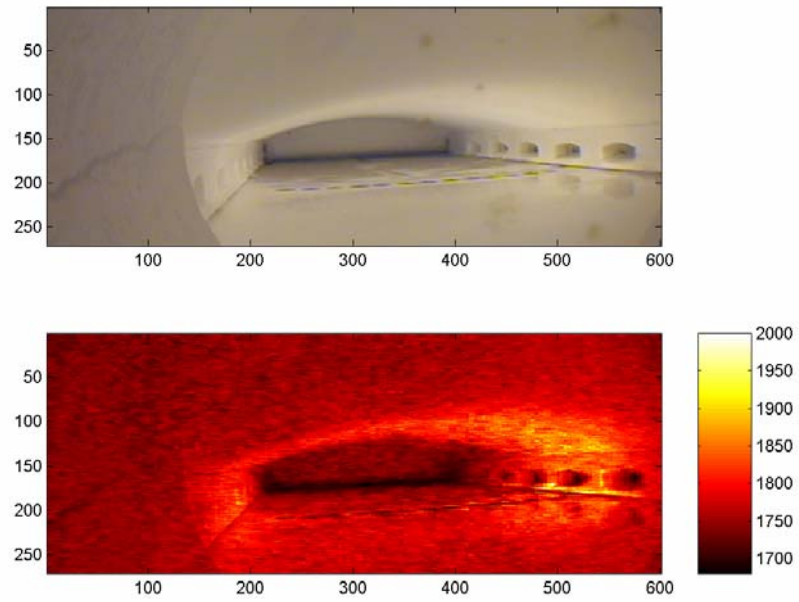**Figure 5.6 Temperature Distributions in the Furnace Calculated by Red / Green Channel**
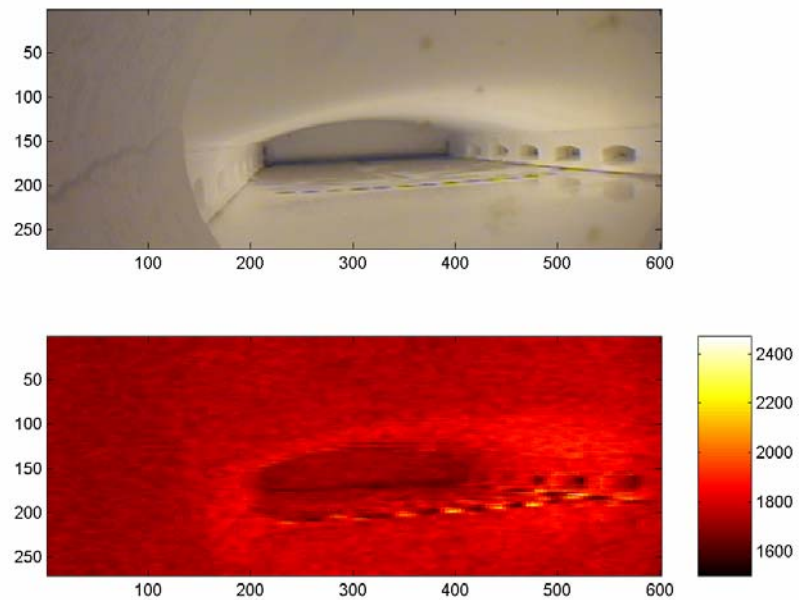


**Figure 5.7 Temperature Distributions in the Furnace Calculated by Green / Blue Channel**

The adjustment of iris influences the ratio of the color in the image. The temperature distribution changes also. Figure 5.6 shows higher temperature than Fig 5.4. The maximum temperature in Figure 5.7 reaches 2400 K, which is unreasonable based on IR gun readings.  Therefore, it proves again that it is not feasible to apply green/blue to temperature calculations.

## 5.3     Wall Temperature Distribution in Furnace II

In the experiment in Furnace I (See Section 5.2), the CCD camera is connected with the video recorder. The image is extracted from the video. In this experiment, the second furnace similar to furnace I is chosen and the CCD camera MicroPix C640 (See Appendix 2) is employed and directly connected with computer by IEEE 1394 firewire interface.  The captured image is also real-time saved to the computer.  This CCD system improves the quality of captured image due to avoid recording the video by the camcorder and video tapes.[62]  The response curve method is utilized for calculating the wall temperature. The calculated temperature results are compared with the thermocouple reading to verify the accuracy of the response curve method.

## 5.3.1          Wall Temperature Calculation Camera Response Curve Method

The camera response curve method is employed to calculate the temperature distribution in this experiment.  The CCD camera MicroPix C640 is assembled with SONY CCD sensor Monochrome Sony ICX-084AL.  The response curve of CCD sensor is shown in Fig.  5.8. The curve shows the response value for red, green and blue color between the wavelength 400 and 700nm. The response curve method utilized this curve to calculate the temperature distribution.
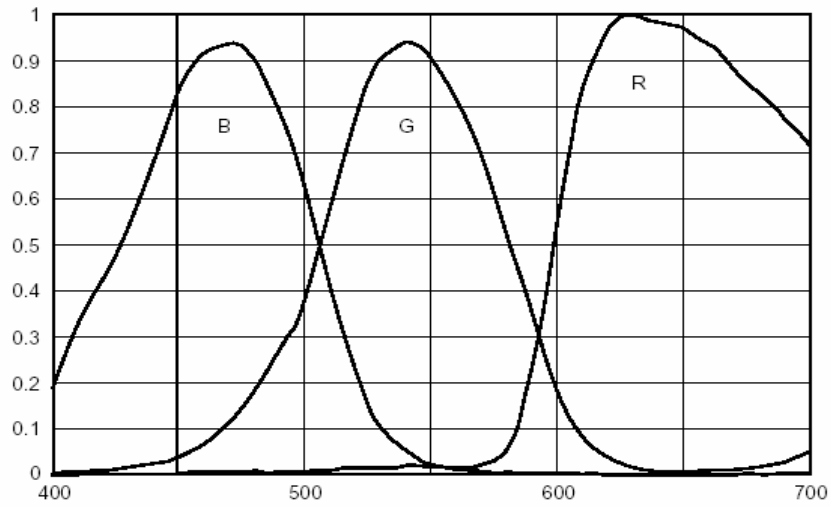
**Figure 5.8 CCD Sensor SONY Monochrome Sony ICX-084AL Response Curve**

A sequence of images is picked up for temperature calculation at one minute interval from 14:28 PM to 14:48 PM (Eastern Time). Figure 5.9 shows the furnace image captured by CCD camera C640 at 14:28 PM.



**Figure 5.9 the Image Captured by MricoPix C640 CCD Camera at 14:28PM**

For the Two-Color method using the camera response curve, the blackbody temperature is set at 2222K based on the Gas / Air combustion adiabatic temperature [63]. The average temperature in the sampled region (6 by 3 pixels) is calculated from eighteen temperature values on the right wall beyond burner 6. This region is marked by white rectangle in Fig. 5.9. The two-color method utilizes the red and green color channel for the temperature calculations.

In order to verify the accuracy of the calculation model, the trend of the calculated temperatures is compared with the readings from the two thermocouples T1 and T2 installed in the furnace neighboring region beyond burner No. 6.

Figure 5.10 demonstrates the temperature variation with the time and the calculated temperature by Red/Green has matched the trend and value with the thermocouple readings.
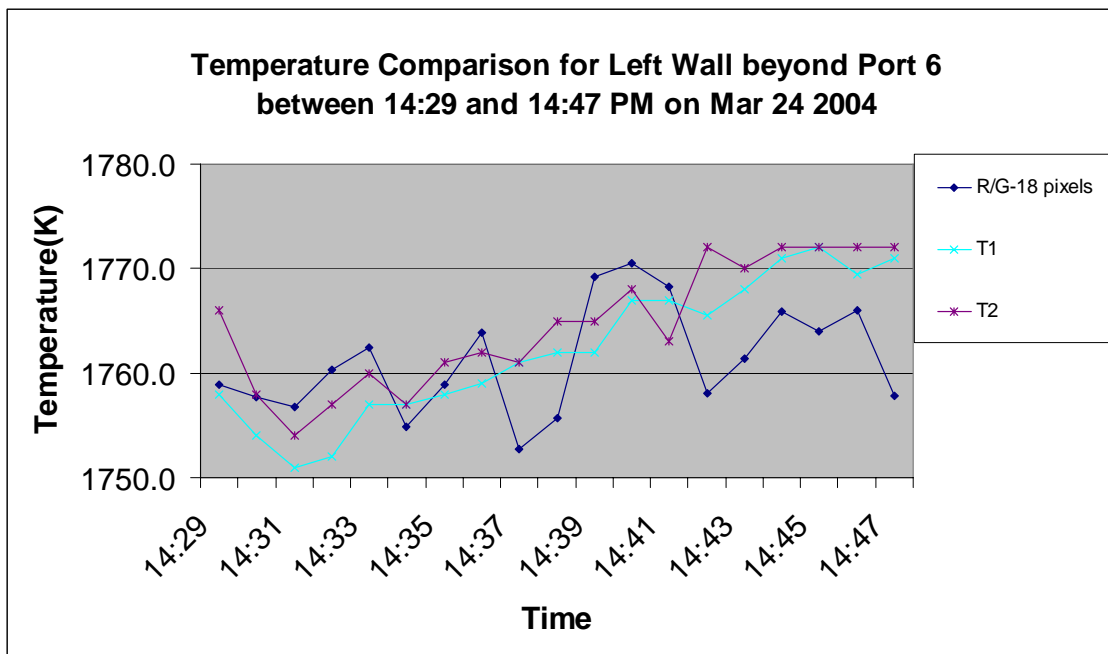


**Figure 5.10 Calculated Temperature Comparisons with Thermocouple Reading**

## 5.4    Wall Temperature Distribution for Furnace I with MicroPix Camera

The new CCD camera Micropix C1024 Camera with higher resolution is utilized in the experiment. Compared with 640 by 480 pixels for C640 camera, it has 1024 by 768 effective pixels (See Appendix 4).  Both the response curve method and reference method are applied to temperature calculations. The results from both methods are compared and discussed in order to investigate the advantage of each method. For the response curve method, the blackbody temperature is set to 1875K when all burners are turned off;  for the reference method, the reference points with 4 by 4 pixel are located on left-side wall between port 4 and port 5.

Figure 5.11 shows the wall temperature distribution based on the image captured by the CCD camera C1024. The maximum temperature is about 1950K located in the crown region near burner 4.
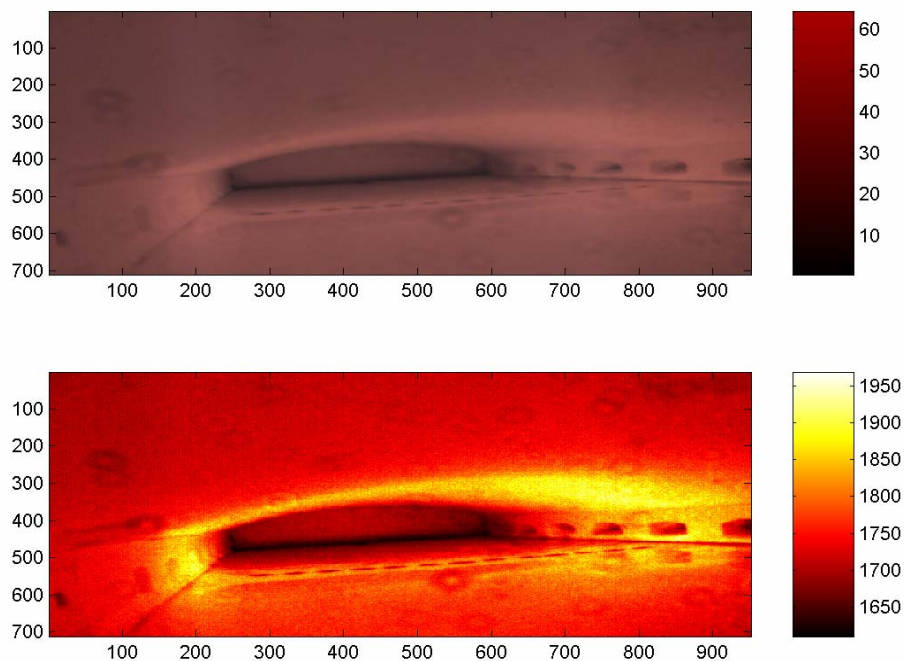


**Figure 5.11 Temperature Distribution Based on the Image Captured by Camera C1024**

Illustrated in Fig. 5.11, the temperature range is between 1600 K and 1975K. The different color options are applied into the temperature calculation. The average temperature for each burner wall is calculated and listed in Table 5.3. IR gun reading for the wall between the burner ports are also listed in this table.

**Table 5.3 Temperature (K) Comparison with Different Calculation Method**

| Method | Color Ratio | Burner 4-5 | Burner 3-4 | Burner 2-3 | Burner 1-2 | 1-backwall | backwall |
|---|---|---|---|---|---|---|---|
| Reference Method | Red/Green | 1862.5 | 1826.3 | 1808.2 | 1774.7 | 1672.1 | 1701.1 |
| | Green/Blue | 1871.0 | 1867.5 | 1861.6 | 1856.0 | 1849.3 | 1853.8 |
| Response Curve Method | Red/Green | 1913.2 | 1875.0 | 1855.9 | 1789.1 | 1716.4 | 1743.3 |
| | Green/Blue | 2173.2 | 2168.5 | 2160.6 | 2153.0 | 2144.2 | 2150.1 |
| IR Gun Readings | | 1867 | 1840 | 1811 | 1794 | 1743 | 1740 |

As listed in Table 5.3, the method based on Red/Green color ratio obtains closer result with the IR Gun readings than the one based on Green/Blue ratio. Compared with IR gun reading, the reference method and response curve method obtains the comparable temperature results.

# 6. Camera Calibration

In previous experiments at commercial furnace, two dimensional temperature distributions are calculated by applying the reference method or camera response curve method based on the captured images. However, the operators in the plant need to acquire the wall temperatures in specified regions in the furnace such as crown, left sidewall, and right sidewall for each burner so that they can monitor the material melting process and optimally control the furnace operations. The camera calibration technique can establish the relationship between the image coordinate system and world coordinate system. The camera calibration technique when integrated with temperature calculation methods will provide the three dimensional temperature distributions for the furnace walls.

The camera calibration problem is considered an important issue in computer vision. Accurate calibration of cameras is especially crucial for applications that involve quantitative measurements such as dimensional measurements and motion from images. Another aspect of camera calibration is to identify the unknown camera model coefficients given the above known/measured data.

The purpose of this work is to implement a camera calibration routine and test its ability to perform accurate measurements in a prototyping environment. The camera calibration experiments in this research are implemented in basketball court to verify the accuracy of linear and nonlinear calibration model.

## 6.1    Introduction

A perspective projection (also called imaging transformation) projects 3-D points onto a plane. The perspective transformation plays a central role in image processing

because it provides an approximation of the manner in which an image is formed by viewing a 3-D world.
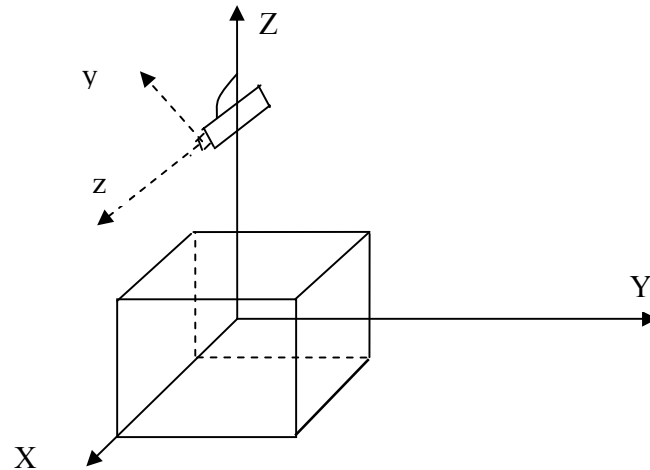


**Figure 6.1 Camera Coordination and World Coordination**

However, implementation of perspective projection equations requires knowledge of the focal length, camera location, and angles of pan and tilt (see Figure 6.1). Although these parameters could be measured directly, determining one or more of the parameters using the camera itself as a measuring device often is more convenient. This requires a set of image points whose world coordinates are known. The computational procedure utilized to obtain the camera parameters using these known points often is referred to as camera calibration.

Existing techniques for camera calibration can be classified into two main categories: linear and nonlinear methods. Direct Linear Transformation (DLT) was developed by Abel-Aziz and Karara[64]. By disregarding lens distortion, DLT falls into linear category and is the most widely used because of its simplicity. Among the linear algorithms, a method known as Tsai's Radial Alignment Constraint camera calibration[65] is viewed by many researchers as a compromise between accuracy and calculation speed.

However, Tsai's RAC method will fail if the camera sensor plane is parallel to the plane defined by the calibration board. The nonlinear calibration techniques [66-70] use a large number of unknowns and a large-scale nonlinear optimization. Nonlinear models are more accurate, but computationally more expensive. Recently, some researches proposed the approaches based on vanishing points defined by the cuboid's projected edges.[71] Such vanishing points correspond to perpendicular direction in space and impose therefore constraints on the transformation between 3D space and the image plane. However, computing vanishing points and lines in the image is often numerically unstable.

## 6.2 Camera Calibration Methods

In this work, two types of camera models are considered. The first model is a pinhole camera model that neglects all optical distortion. The second model takes into account several types of distortions. The first model can be viewed as a first approximation of the second one and will actually be considered as such in the calibration procedure.

## 6.2.1 Linear Camera Calibration

The calibration of the camera is done by taking a set of m object points which: (a) have world coordinates $\{x_{w,i}, y_{w,i}, z_{w,i}\}$, w stands for the world coordination, $i = 1, \ldots, m$ that are known with sufficient precision, and (b) are within the field of view of the camera. These points, referred to as "calibration points", are detected on the camera image at the respective image coordinates, $\{X_i, Y_i\}$.

The most basic camera calibration strategy involves linear least squares identification of the Perspective Transformation Matrix.

The model can be written as

$$X = \frac{a_{11}x_w + a_{12}y_w + a_{13}z_w + a_{14}}{a_{31}x_w + a_{32}y_w + a_{33}z_w + a_{34}}$$ ……………………….EQ(6.1)

$$Y = \frac{a_{21}x_w + a_{22}y_w + a_{23}z_w + a_{24}}{a_{31}x_w + a_{32}y_w + a_{33}z_w + a_{34}}$$ ………………………….EQ(6.2)

where we set $a_{34}=1$ since the scaling of the coefficients $a_{11}$, …, $a_{34}$ does not change the value of X and Y. The coefficients $a_{11}$, …, $a_{34}$ correspond to what is called the "Perspective Transformation Matrix." EQ(6.1) and (6.2) can now be combined into the identification model:

$$\begin{bmatrix} x_w & y_w & z_w & 1 & 0 & 0 & 0 & 1 & -Xx_w & -Xy_w & -Xz_w \\ 0 & 0 & 0 & 0 & x_w & y_w & z_w & 1 & -Yx_w & -Yy_w & -Yz_w \end{bmatrix} \begin{bmatrix} a_{11} \\ \vdots \\ a_{33} \end{bmatrix} = \begin{bmatrix} X \\ Y \end{bmatrix}$$ ……………...EQ(6.3)

The eleven unknown coefficients can be obtained using linear least squares. The minimum number of calibration points is six. Each data point pair $\{(x_{w,i}, y_{w,i}, z_{w,i}), (X_i, Y_i)\}$ contributes two algebraic equations for the unknown coefficient vector $a = [a_{11}, …, a_{33}]^T$ of the type shown in EQ (6.3). One can further show that the calibration points must not be coplanar. To illustrate this point, consider the case of a planar calibration board characterized by $z_{w,i} = C = $ constant, for any i. In this case the coefficient matrix obtained on the left hand side of the "stacked" equations EQ (6.3) is singular since columns 3 and 4 as well as columns 7 and 8 are linearly dependent. [72]

## 6.2.2     Nonlinear Camera Calibration

It is well-known that actual cameras and lenses sustain a variety of aberrations and thus do not obey the above perfect linear model. The main error sources are several

types of imperfections in the design and assembly of lenses composing the camera's optical system.

Three types of distortion are considered in the Weng etc. experiments.[66] The first one is caused by an imperfect lens shape and manifests itself by radial positional error only, whereas the second and the third types of distortion are generally caused by improper lens and camera assembly and generate both radial and tangential errors in point positions.
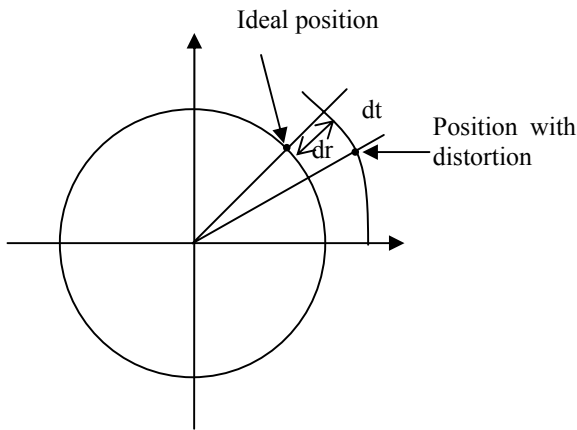


**Figure 6.2 Radial and Tangential Distortions**        **Figure 6.3 Effect of Radial Distortion; Solid Lines: No Distortion; Dashed Lines: with Radial Distortion**
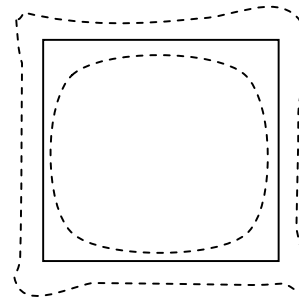
The total distortion model is generated as follows:

$$\delta_x(X,Y) = (g_1 + g_3)X^2 + g_4 XY + g_1 Y^2 + k_1 X(X^2 + Y^2)$$

$$\delta_y(X,Y) = g_2 X^2 + g_3 XY + (g_2 + g_4)Y^2 + k_1 Y(X^2 + Y^2) \ldots\ldots\ldots EQ(6.4)$$

Radial distortions are assumed as third-order distortion in EQ (7.4) by Weng etc.[66] For the majority of medium-angle, non-photogrammetric lenses employed in today's metric and non-metric close-range cameras, the third-order term is sufficient to account for the induced aberrations. For wide-angle lenses, higher order terms (very rarely above seventh order) are often required to adequately model lens distortion.

The complete nonlinear camera model is shown:

$$\frac{a_{11}x_w + a_{12}y_w + a_{13}z_w + a_{14}}{a_{31}x_w + a_{32}y_w + a_{33}z_w + a_{34}} = X + (g_1 + g_3)X^2 + g_4XY + g_1Y^2 + k_1X(X^2 + Y^2)$$

$$\frac{a_{21}x_w + a_{22}y_w + a_{23}z_w + a_{24}}{a_{31}x_w + a_{32}y_w + a_{33}z_w + a_{34}} = Y + g_2X^2 + g_3XY + (g_2 + g_4)Y^2 + k_1Y(X^2 + Y^2) \ldots\ldots EQ(6.5)$$

with: $(k_1, g_1, g_2, g_3, g_4)$ are the set of distortion parameter.

Whenever any nonlinear algorithm is employed, convergence and stability of the algorithm are always issues. A two-step approach suggested by Weng that solves the distortion parameters and other camera parameters alternately in each iteration can be implemented as follows: the first-step consists of using a non-iterative algorithm to directly compute a closed-form solution for all the external parameters and some major internal parameters based on a distortion-free camera model. The second step is a nonlinear optimization based on a camera model that incorporates distortion using the solution of the first step as an initial guess.

## 6.3    Basketball Court Experiment Results

This experiment was implemented in the Student Recreation Center in University of Missouri – Columbia. The basketball courts are chosen for the experiment because they have the comparable size with the commercial furnace. The purpose of the experiment was to obtain the basketball court image and to verify the accuracy of the linear and nonlinear camera calibration model. The view of three basketball courts is captured separately by a commercial digital camera and a CCD camera with lens. In the basketball coordination system, the center of the court is set as the original point and $x_w$ and $y_w$ are shown in Fig. 6.4. $z_w$ is up-vertical to the court.
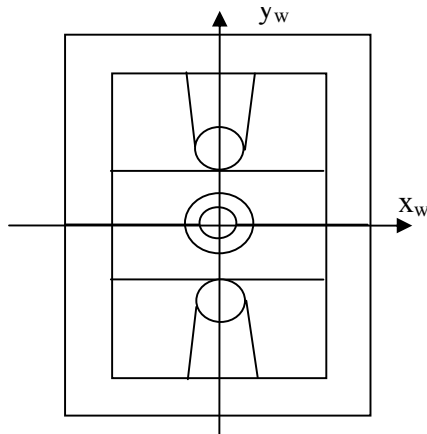
**Figure 6.4 Basketball Court Coordination Systems**

### 6.3.1 Model Verification for Digital Camera Image

The basketball court image is the high-resolution digital image with 1600 by 1200 pixels captured by a common commercial digital camera. Many yellow labels are posted on the court line at 6-foot intervals and are shown as the yellow points in Fig 6.5.



**Figure 6.5 Basketball Court Image Captured by Commercial Digital Camera**

### 6.3.1.1 Linear Model Result

In order to set up the linear camera calibration model, six points will be selected with the known dimensional information in the world coordination and image coordination system. Initially, four points on the basketball court and two points on the basketball board circle are chosen. These six points are listed in Table 6.1 and are marked by yellow crossing-points in Fig. 6.6. Based on the linear model EQ (6.3) and the dimensional information about these six points, the coefficients in the linear camera calibration model are resolved.

Since the court geometrical information is standard and easy to know, the court borderlines are redrawn by the use of the linear model with the yellow color in Fig. 6.6.

**Table 6.1 Six Reference Points Chosen on the Basketball Court**

| Court Coordinate | | | Image Coordinate | | Comment |
|---|---|---|---|---|---|
| $x_w$ (ft) | $y_w$ (ft) | $z_w$ (ft) | X (pixel) | Y (pixel) | |
| -15 | 0 | 0 | 140 | 805 | |
| 15 | 0 | 0 | 1416 | 765 | |
| 15 | 30 | 0 | 1095 | 316 | |
| -15 | 30 | 0 | 290 | 315 | |
| 0 | 30 | 10 | 711 | 51 | Basketball board circle |
| 0.75 | 29.25 | 10 | 732 | 47 | Basketball board circle |

As shown in Fig. 6.6, there are some pixel offsets between the yellow redrawing lines and the original lines, especially in the border region of the image.

**Figure 6.6 Redrawing Basketball Court by Linear Calibration Model**

Then the previous two of six points are changed and two new points are added on the backwall edge instead of on the basketball board circle (see Table 6.2). Thus, the updated six reference points are nearly spread in the whole image (see white crossing points in Fig 6.7).

**Table 6.2 Six Reference Points Chosen on the Basketball Court**

| Court Coordinate | | | Image Coordinate | | Comment |
|---|---|---|---|---|---|
| $x_w$ (m) | $y_w$ (m) | $z_w$ (m) | X (pixel) | Y (pixel) | |
| -15 | 0 | 0 | 140 | 805 | |
| 15 | 0 | 0 | 1416 | 765 | |
| 15 | 30 | 0 | 1095 | 316 | |
| -15 | 30 | 0 | 290 | 315 | |
| *-2.7848* | *45.4182* | *3.3301* | *620* | *113* | *Back Wall* |
| *18.535* | *45.4182* | *3.3301* | *1095* | *123* | *Back Wall* |

Note: Italics points are different points with table 6.1

**Figure 6.7 Redrawing Basketball Court by Linear Calibration Model**

As shown in Fig 6.7, yellow lines are drawn using the linear model. Compared with Fig 6.6, there is a little improvement for matching between the original borderlines and yellow lines in Fig 6.7.

The conclusion is drawn that it is important to select the known points for the linear calibration model calculation. Six accurate-known points will bring better results if they are spread around the whole image. However, there are still some pixel offsets because of unavoidable distortions in the camera system and accuracy in the calibration model. In recent years, many researchers have focused on increasing the accuracy of the camera calibration with nonlinear models.

### 6.3.1.2    Nonlinear Model Result

The nonlinear model considers the distortions of the camera system. Since there are 16 coefficients to be resolved according to EQ (6.3), 17 or more known points are selected in the image (see Table 6.3). All known points are marked by blue crossing in Fig. 6.8. Because it is much slower to draw the lines by the nonlinear model than by the linear one, we only draw the remarkable points by yellow crossing in Fig 6.8.

**Table 6.3 Seventeen Reference Points Chosen on the Basketball Court**

| Court Coordinate | | | Image Coordinate | | Comment |
|---|---|---|---|---|---|
| $x_w$ (m) | $y_w$ (m) | $z_w$ (m) | X (pixel) | Y (pixel) | |
| -15 | -10 | 0 | 45 | 1137 | |
| -5 | -10 | 0 | 610 | 1117 | |
| 5 | -10 | 0 | 1146 | 1086 | |
| -15 | 0 | 0 | 141 | 805 | |
| -5 | 0 | 0 | 1021 | 781 | |
| 15 | 0 | 0 | 1416 | 765 | |
| -15 | 10 | 0 | 206 | 585 | |
| 5 | 10 | 0 | 939 | 573 | |
| 15 | 10 | 0 | 1277 | 567 | |
| -15 | 30 | 0 | 291 | 315 | |
| -5 | 30 | 0 | 567 | 313 | |
| 5 | 30 | 0 | 839 | 314 | |
| 15 | 30 | 0 | 1095 | 316 | |
| -2.7848 | 45.4182 | 3.3301 | 620 | 113 | Back Wall |
| 18.535 | 45.4182 | 3.3301 | 1095 | 123 | Back Wall |

Illustrated as Fig 6.8, most points with yellow crossing are overlapped with the yellow label. Compared with the linear model results in Fig 6.7, the conclusion can be drawn that the non-liner model will supply more accurate results for camera calibration. In order to qualitatively evaluate the results, the average distance between known yellow label points $\vec{X}$ and the corresponding calculated points $\vec{Y}$ are calculated. The average distance equation Er is as follows:

$$\text{Er} = \frac{\sum_{i=1}^{K}\left\|\vec{X_i} - \vec{Y_i}\right\|}{K} \tag{6.1}$$

Where: K is the total number of calibrated points.

X is the known pixel location marked by the yellow label

Y is the corresponding calculated pixel location by calibration model

‖ ‖ is Euclidean distance


Fig 6.6 is redrawn by linear calibration model. The average distance error in Fig 6.6 is 4.89 pixels based on Eq. 6.1.  Fig 6.8 is redrawn by non-linear calibration model. The error is 2.31 pixels.  It proves that the non-linear model introduce less error than the linear one. However, the non-linear model consumes more calculation time.
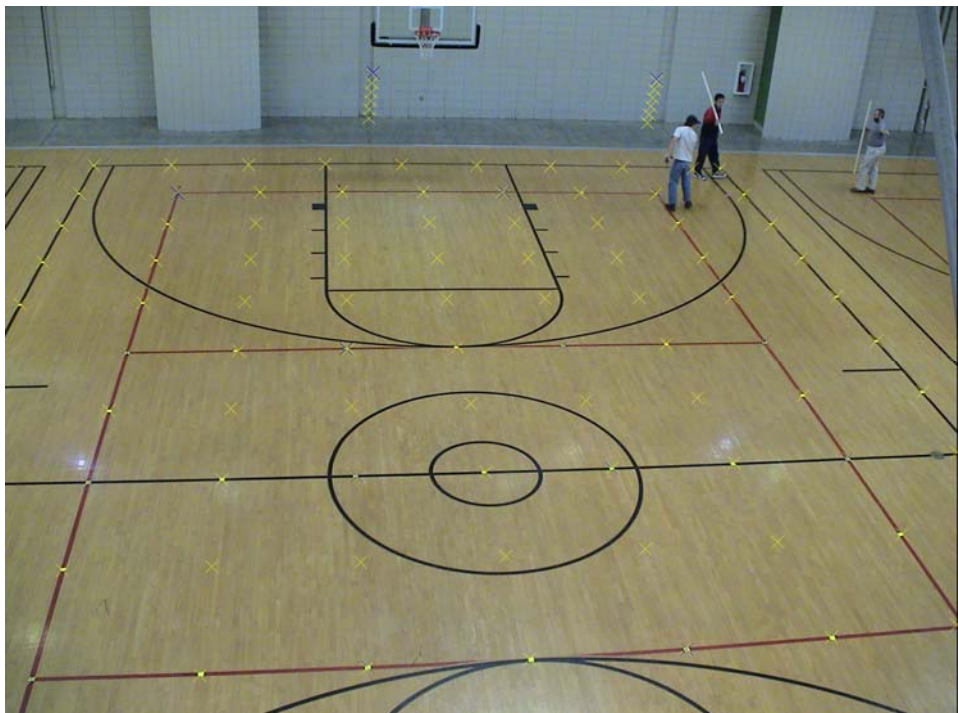


**Figure 6.8 Redrawing Crossing Points by Nonlinear Calibration Model**

**6.3.2**        **Model Verification for CCD camera image with the lens**

The image (see Fig. 6.9) is captured by Panasonic GP KR-222 CCD camera with the 90 degree view angle lens. The image with 720-by-480 pixel has the low quality because less light enters the CCD camera through the lens. In addition, the lens results in more distortion. In order to obtain more known points, the stick attached with the yellow label is hold vertically by the person standing on the court. Fig. 6.10 is reproduced by synthesizing several frames together in order to obtaining the stick height in the different position at the same time.



**Figure 6.9 Image Captured by the CCD Camera with Lens**

**Figure 6.10 Synthesized Image with Multiple Reference Points**

### 6.3.2.1    Linear Calibration Model

Six points are chosen as the known points (See Table 6.4). Two of six points are located on the stick hold by the person standing on the court. These points are draw by the blue crossing in Fig. 6.11.

**Table 6.4 Six Known Points Chosen on the Basketball Court**

| Court Coordinate | | | Image Coordinate | | Comment |
|---|---|---|---|---|---|
| $x_w$ (ft) | $y_w$ (ft) | $z_w$ (ft) | X (pixel) | Y (pixel) | |
| 15 | -25 | 0 | 605 | 439 | |
| 15 | 0 | 0 | 515 | 178 | |
| -15 | 0 | 0 | 152 | 185 | |
| -10 | -10 | 0 | 161 | 254 | |
| 0 | 0 | 2 | 320 | 160 | Stick hold by Rodney |
| -15 | -10 | 6 | 85 | 184 | Stick hold by Rodney |

**Figure 6.11 Redrawing the Basketball Court by Linear Model**

Based on the linear model, the court lines are drawn in Fig. 6.11. The new lines are not matched with the court very well.

Two known points on the stick are changed because perhaps the stick is not fully vertical to the court and it is also hard to find the target on the stick by eyes. Instead, two points on the basketball board edge marked by blue crossing in the Fig 6.12.

**Table 6.5 Six Reference Points Chosen on the Basketball Court**

| Court Coordinate | | | Image Coordinate | | Comment |
|---|---|---|---|---|---|
| $x_w$ (ft) | $y_w$ (ft) | $z_w$ (ft) | X (pixel) | Y (pixel) | |
| 15 | -25 | 0 | 605 | 439 | |
| 15 | 0 | 0 | 515 | 178 | |
| -15 | 0 | 0 | 152 | 185 | |
| -10 | -10 | 0 | 161 | 254 | |
| 2.7250 | 31 | 9.2750 | 368 | 11 | Basketball board edge |
| -2.7250 | 31 | 9.2750 | 327 | 13 | Basketball board edge |

**Figure 6.12 Redrawing the Basketball Court by Linear Model**

Shown as Fig 6.12, the center line doesn't match well.    Four new points around the

center court are selected in table 6.6 and are marked by blue crossing in Fig 6.13.

**Table 6.6 Six Reference Points Chosen on the Basketball Court**

| Court Coordinate | | | Image Coordinate | | Comment |
|---|---|---|---|---|---|
| $x_w$ (ft) | $y_w$ (ft) | $z_w$ (ft) | X (pixel) | Y (pixel) | |
| 0 | 10 | 0 | 332 | 130 | |
| 15 | 0 | 0 | 515 | 178 | |
| -15 | 0 | 0 | 152 | 185 | |
| -10 | -10 | 0 | 161 | 254 | |
| 2.7250 | 31 | 9.2750 | 368 | 11 | Basketball board edge |
| -2.7250 | 31 | 9.2750 | 327 | 13 | Basketball board edge |

**Figure 6.13 Redrawing the Basketball Court by Linear Model**

Compared with Fig 6.12, there is much improvement for center line matching in Fig 6.13. However, more pixels offsets occur at the basketball court sideline.

Therefore the linear model has the limited accuracy for camera calibration based on the distorted image. The nonlinear model will be employed in the following experiment.

### 6.3.2.2    Nonlinear Calibration Model

In the non-linear model, different known point quantity (seventeen, nineteen, twenty-two) is selected and separately shown in Fig 6.14-6.16. The blue crossings refer to the known points in the image. The yellow crossings are calculated and redraw in the image by nonlinear model. The blue crossings refer to the reference points.

**Figure 6.14 Marking Points by Nonlinear Model Based on 17 Reference Points**



**Figure 6.15 Marking Points by Nonlinear Model Based on 19 Reference Points**

**Figure 6.16 Marking Points by Nonlinear Model based on 22 Reference Points**

In Fig 6.14 and Fig 6.15, there are some points that are not matched with the yellow label post on the court line, especially the points on the red three-meter line of the volleyball court. In Fig 6.16, all yellow crossing points almost overlapped with the yellow label. Compared with Fig. 6.14 and Fig. 6.15, Fig 6.16 shows the best result when the model utilizes twenty-two points. Therefore, more reference points will improve the accuracy of the non-linear camera calibration model.

It is drawn as the conclusion that nonlinear model is more accurate to simulate the camera system than the linear model. However, it also needs to input more references points and consumes more calculation time. Linear model will be easy and convenient to implement because it only needs six reference points as input. In order to increase the calibration accuracy in the specified region, more reference points spread out in this region can be selected and utilized. This camera calibration technique is utilized and integrated with the temperature calculation method to work out the temperature distribution in the next chapter.

# 7. Furnace Modeling and 3-D Temperature Calculations

The linear and non-linear camera calibration models have already been successfully verified in the basketball court. The camera calibration technology in this work is applied in performing metrology on furnace dimension, different burner region identification, batch-line distance measurement, 3D temperature distribution.

## 7.1    Calibration Model for the Furnace

### 7.1.1         Calibration model setup

In the industrial plant, the CCD camera is set up on the corner of the furnace and captures the image for the flame and the wall in the furnace (see Figure 7.1). Since the camera location and angles of tilt and pan are not known, the camera calibration technique is employed for dimensional measurement in the furnace. In the image coordinate system, the original point is located in left-top corner and X-Y axis is illustrated in Figure 7.1. The pixel location is based on this coordinate system XY.
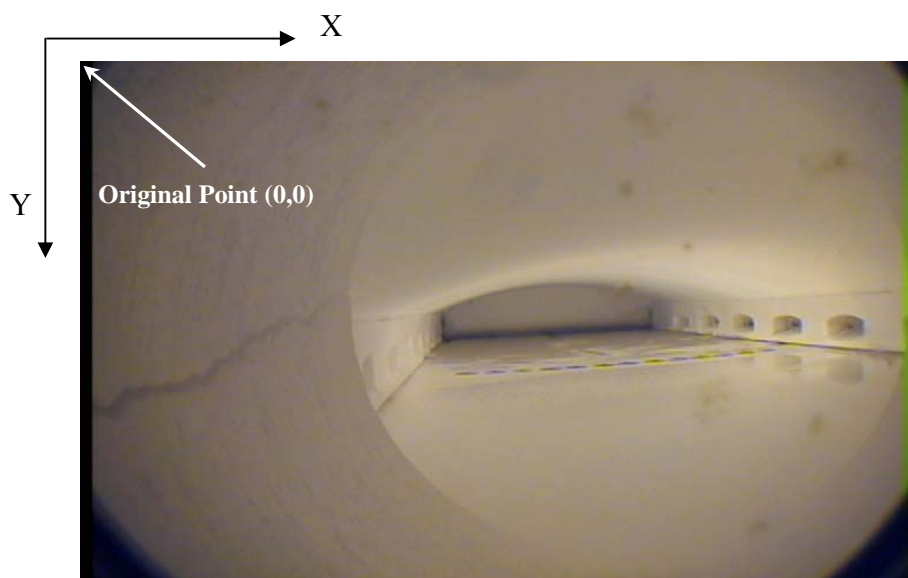


**Figure 7.1 Furnace Image Coordinate System**

The geometrical information for this industrial furnace which includes furnace length, width, distances among burners, and backwall height are known.  In the defined coordinate system xyz (see Figure 7.2), the left-bottom corner of the furnace is set as the original point, $x_w$ axis is parallel to the furnace length, $y_w$ axis is parallel to the furnace width and $z_w$ axis is vertical to the furnace bottom. In Figure 7.2, the maximum and minimum backwall heights are also illustrated. The backwall with the maximum height is located in the middle of the furnace. The backwall with the minimum height is located at the crossing edge between the side wall and back wall.
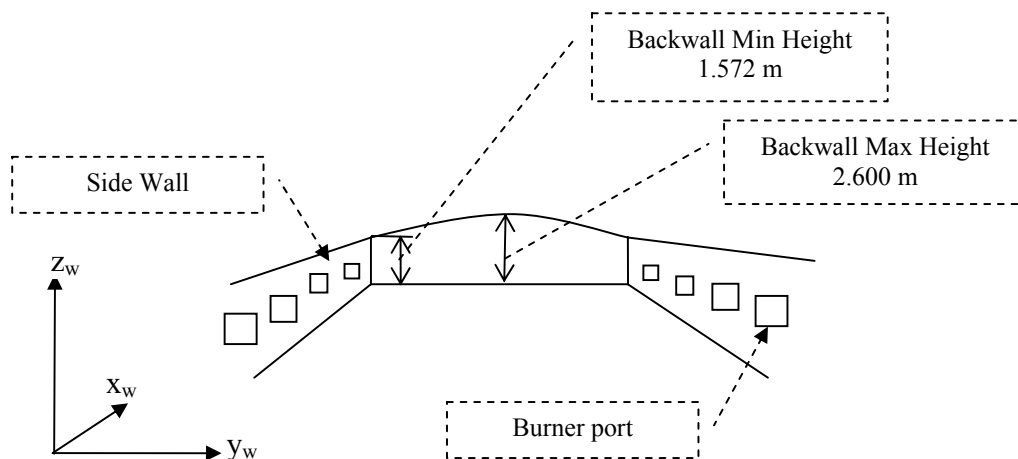


**Figure 7.2 the Coordinate System xyz in the Furnace**

In Figure 7.3, the geometrical information for this industrial furnace is illustrated including furnace width, furnace length, and distances among burners. The location installing the camera is shown as the red eclipse. The burners are numbered as No.1 to No.6 starting from the backwall.
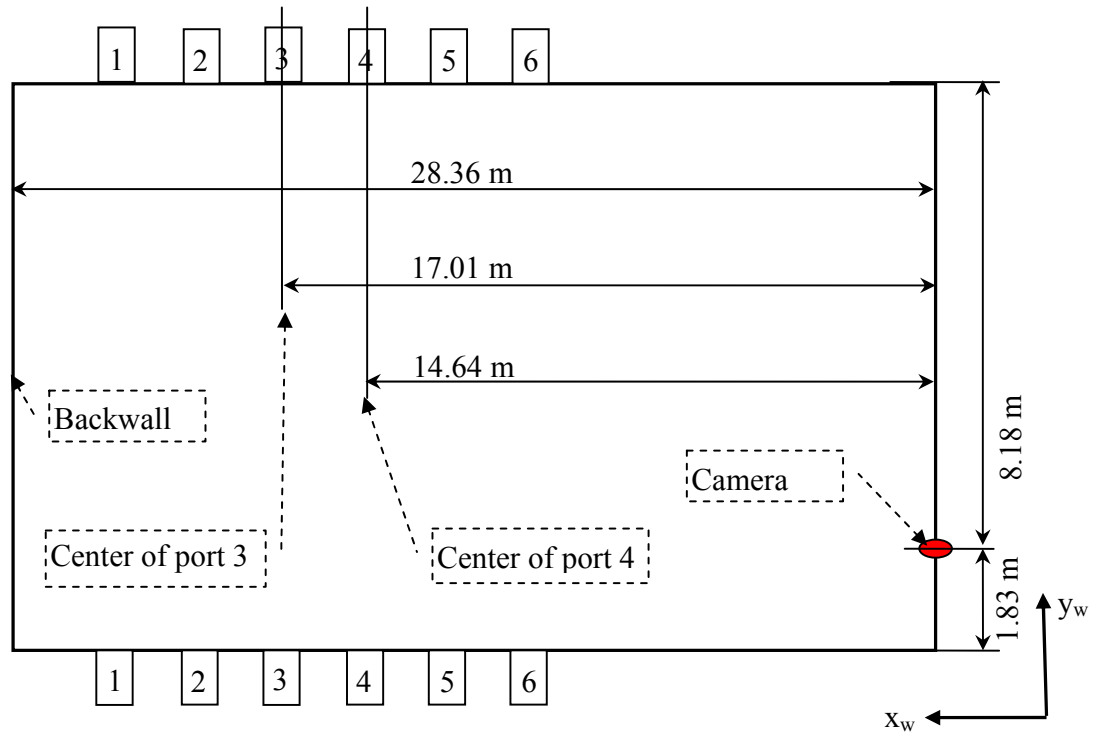
**Figure 7.3 Geometrical Information in the Coordinate System**

Since there is limited dimensional information for the furnace, it is difficult to find seventeen known points to be applied in non-linear calibration model. The linear model only needs minimum six calibration points according to the equation EQ (6.3), so this experiment utilizes the linear model in the camera calibration.

Six points with the known dimensional information are selected on the furnace image. These six points, located on the backwall, left sidewall and right sidewall in the furnace, are spread in the image. Figure 7.4 illustrates the furnace image with the location of six known points shown by white crossings.
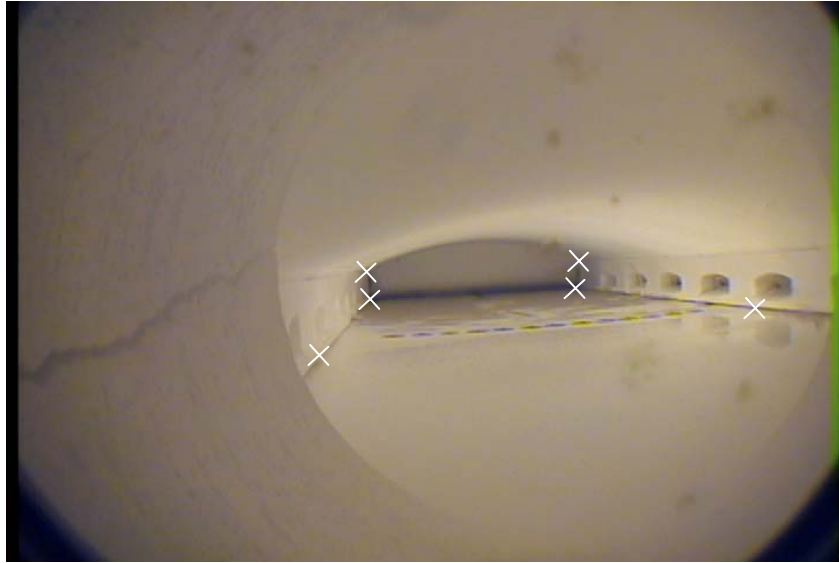
**Figure 7.4 Locations of Six Known Points in the Image**

Table 7.1 lists the location information for the six known calibration points based on the furnace dimensional information in world coordinates xyz and the corresponding pixel position in the image coordinates XY.

**Table 7.1 Six Known Points for the Linear Calibration in the Furnace**

| Furnace Coordinate | | | Image Coordinate | | Location in Furnace |
|---|---|---|---|---|---|
| $x_w$ (m) | $y_w$ (m) | $z_w$ (m) | X (pixel) | Y (pixel) | |
| 11.59 | 10.01 | 0 | 645 | 265 | Left Burner5 port |
| 12.95 | 0 | 0 | 268 | 311 | Right Burner5 port |
| 26.38 | 0 | 0 | 314 | 258 | Back Wall Bottom Corner |
| 26.38 | 10.01 | 0 | 495 | 247 | Back Wall Bottom Corner |
| 26.38 | 0 | 1.57 | 313 | 233 | Back Wall Crown Corner |
| 26.38 | 10.01 | 1.57 | 494 | 223 | Back Wall Crown Corner |

After solving the equation EQ (6.3), the solution for the coefficient vector $\vec{a}$ = [$a_{11}$, $a_{12}$…, $a_{33}$]$^T$ is as follows:

$a_{11}$ = -126.1278     $a_{12}$ = -220.3764     $a_{13}$ = 7.6872     $a_{14}$ = 584.6475

$a_{21}$ = -83.8692     $a_{22}$ = -20.5357     $a_{23}$ = 146.9078     $a_{24}$ = -45.9626

$a_{31}$ = -0.3689     $a_{32}$ = -0.1266     $a_{33}$ = 0.0043

Based on the coefficient vector $\vec{a}$, the relationship between the furnace coordinates xyz and image coordinates XY is build up. If any three coordinate position of $\{x_w, y_w, z_w, X, Y\}$ are known, the other two can be resolved by EQ. (6.3). For example, if the point location in the world coordinates $\{x_w, y_w, z_w\}$ are known, the corresponding pixel location $\{X, Y\}$ will be resolved by EQ (6.3) based on coefficient vector a.

### 7.1.2        Model Verification

In order to verify the accuracy of the calibration model, the furnace edges which are composed of the known geometrical points$\{x_w, y_w, z_w\}$ are resolved for the pixel location $\{X, Y\}$ in the image and are drawn with black color on the furnace image (See Figure 7.5). At the same time, the burner regions are separated by drawing the black line in the image based on the dimensional information of the furnace burners. (See Figure 7.6) Since the drawn lines are matched with the furnace edge, it is evident that the linear model is accurate enough for this furnace image calibration.
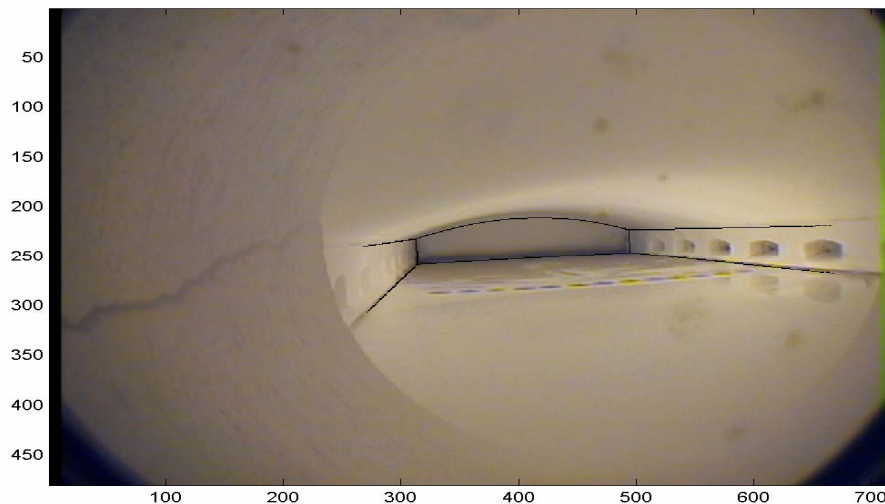


**Figure 7.5 Furnace Edge Line Drawn by Camera Calibration Model**
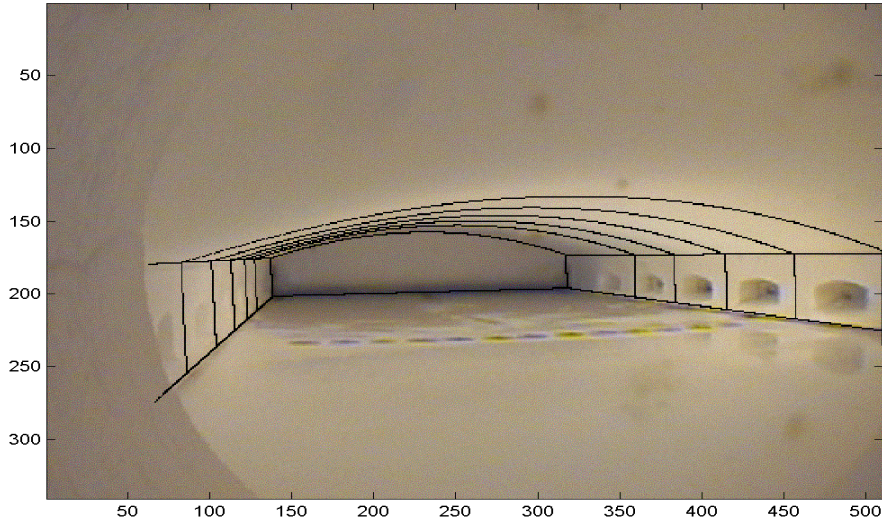
**Figure 7.6 Furnace Burner Region Separated by Lines Based on Camera Calibration Model**

### 7.1.3         Average Temperature for Grids in the Furnace

The grid is the basic unit in Calculational Fluid Dynamics (CFD). The grids are drawn by camera calibration model and the average temperatures in each grid could be calculated to compare with the CFD results. Figure 7.7 illustrates the furnace image with the drawing grid. The grid length x = 1.395095m, width y = 1.000760m, height z = 0.81m. The average temperature on each grid is calculated and utilized in other CFD applications. Table 7.2 shows the example of average temperature for each grid in the top row on right sidewall.

**Table 7.2 Average Temperature on each grid in the top row on right sidewall**

| Backwall →→ Burner 1 →→ Burner 2 →→ Burner 3 →→→ Burner 4 →→→ Burner 5 | | | | | | | | | | |
|---|---|---|---|---|---|---|---|---|---|---|
| 1772.3 | 1784.9 | 1801.7 | 1833.3 | 1841.1 | 1865.5 | 1874.6 | 1874.5 | 1879.8 | 1877.7 | 1881.5 |
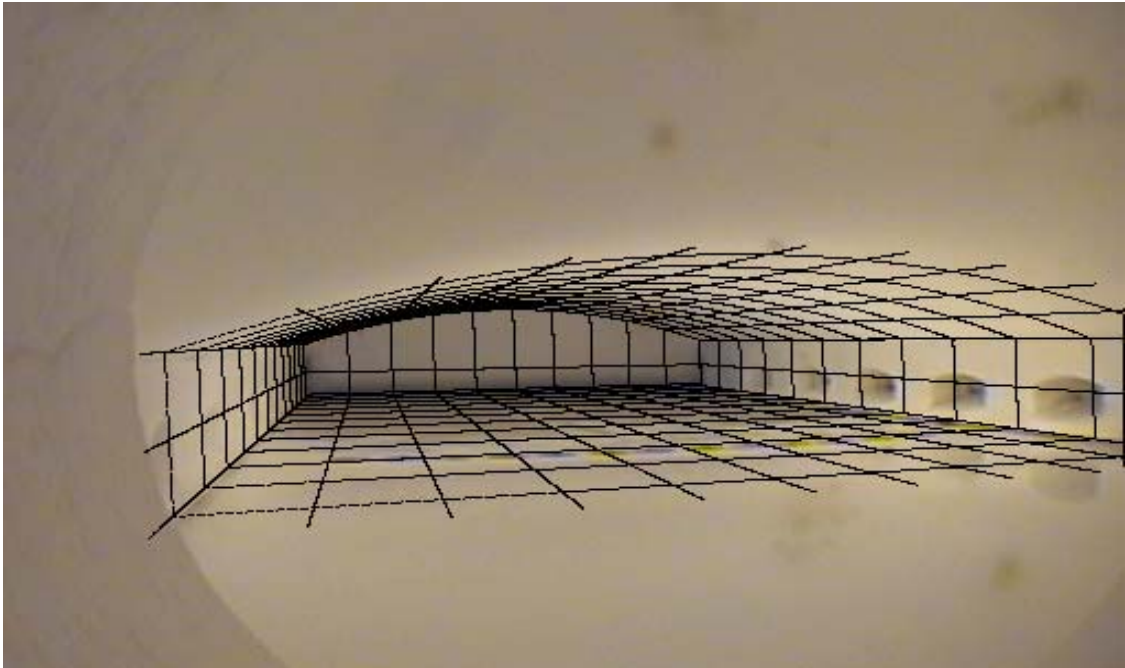
**Figure 7.7 Drawing Grids in the Furnace**

## 7.2     Reference Two-color Method for 3-D Temperature Calculations

The two-color reference method always employs the reading of the thermocouple or IR Gun, however, it is hard to find the corresponding reference position in the image where the thermocouple is installed or the IR Gun is pointed.  With the application of camera calibration, the position of the reference points can be calculated by calibration equation if their dimensional information is known.   Then, one can calculate the temperature profiling for each burner region using the temperature calculation methods.

For example, suppose that the temperature distribution on burner 5 region is needed.  The position of thermocouple for burner 5 is located on the center crown of the furnace ($x_w$ = 12.27m $y_w$ = 5.01 m and $z_w$ = 2.60m).  Using the linear calibration model, the position in the image is determined (x=492, y=190).  Nine pixels around the pixel (x=492, y=190) are used as reference points where positions are determined by camera calibration technique (See Table 7.3).

The image is captured by CCD camera in the industrial furnace when the right burners were turned off. The crown temperature around the burner 5 is $T_{ref}$ 1872.15 K measured by the thermocouple at the time when the image was captured.

**Table 7.3 Correction Coefficient Based on the Reference Pixels**

| X | Y | Red/Green | Green/Blue | A |
|---|---|---|---|---|
| 492 | 190 | 1.0757 | 1.1635 | 6.2339 |
| 493 | 190 | 1.0645 | 1.1698 | 6.2992 |
| 494 | 190 | 1.0642 | 1.1615 | 6.3013 |
| 492 | 191 | 1.0870 | 1.1429 | 6.1692 |
| 493 | 191 | 1.0815 | 1.1152 | 6.2002 |
| 494 | 191 | 1.0815 | 1.1152 | 6.2002 |
| 492 | 192 | 1.0939 | 1.1242 | 6.1299 |
| 493 | 192 | 1.0820 | 1.1296 | 6.1976 |
| 494 | 192 | 1.0820 | 1.1296 | 6.1976 |
| A (mean ± std. dev.) | | | | 6.2143±0.0562 |

Figure 7.8 shows the masked image representing the 3-D region (wall and ceiling) for burner 5. The mask is drawn by the use of the camera calibration linear model and furnace burner 5 dimensional data.



**Figure 7.8 Wall Image with the Mask around the Region for Burner No.5**

Based on correction coefficient A = 5.6572, the temperature profile for the masked image region is obtained. For the presentation purpose, the temperature 1700 K is set for the unmasked region. Figure 7.9 shows the temperature distribution for the region around Burner No.5. The image is split into three regions including left sidewall, crown and right sidewall.
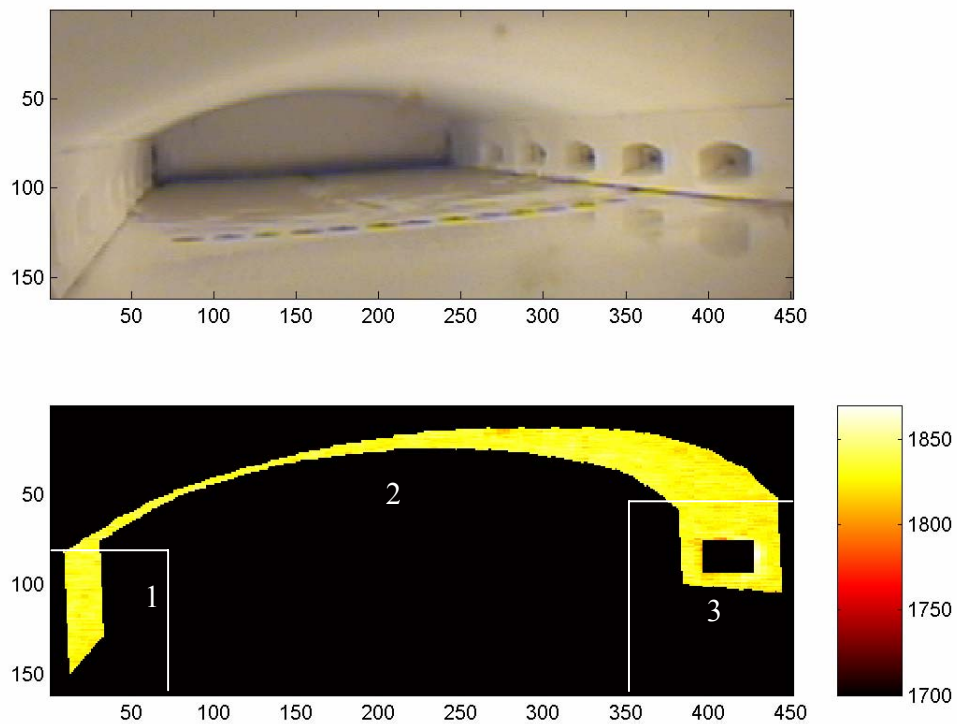


**Figure 7.9 Temperature Distributions for the Region around Burner No.5**

Table 7.4 shows that maximum, minimum, average temperature on the left sidewall, crown region and right sidewall near burner 5. The average temperature near crown region is the highest. As expected, the average temperature in left sidewall is higher than the one in the right sidewall since the right burner is just turned off.

**Table 7.4 Temperature Statistics in Three Regions near Burner No. 5**

|          | Region 1 (K) | Region 2 (K) | Region 3 (K) * |
|----------|--------------|--------------|----------------|
| Min      | 1816.6       | 1806.0       | 1791.8         |
| Max      | 1857.0       | 1854.6       | 1870.2         |
| Mean     | 1832.5       | 1832.8       | 1830.5         |
| Std. Dev | 5.9335       | 6.2066       | 9.1417         |

* In region 3, the masked area is excluded from temperature calculation.

As listed in table 7.4, the values of standard deviation for temperatures in all regions are below 10. The variations in temperature measurement are below 10%, within the acceptable accuracy of ± 10% between CCD results and IR temperature reading results (as IR reading is not considered 100% accurate either!). Hence, it is expected that this temperature measurement variation would not impact glass quality especially as compared to the impact of the furnace temperature variation due to the cycling heating of 20 minutes interval of the commercial glass furnace examined here.

# 8. Conclusion

Visual thermal imaging methods by CCD camera system for calculating the flame or wall temperature are proposed in this work and are also applied in several experiments in the laboratory and commercial furnaces. These novel methods when integrated with camera calibration technology generate three dimensional wall temperature profiles for a gas-fired furnace.

A periscope-based camera with a water cooling system that enables the CCD camera to withstand temperatures up to 3500°F is utilized in this research work. The original CCD system utilizes the interlaced CCD camera Panasonic GP KR-222 and video camcorder to record the video in the DV tape in experiments at a pilot scale glass furnace. The captured image extracted from the video tape is interlaced with medium resolution (720 by 480). To implement the real-time measurement and improve the quality of captured image without using frame grabber, the progressive firewire-based camera C640 and C1024 are utilized in the experiments and data acquisition from the industrial furnace. The captured visual images are directly saved into the computer storage device. The visual thermal imaging overcomes the disadvantages of IR thermography such as high cost, low resolution of the sensors and the lack of image processing supports: edge detection, shape and filtering.

The two-color blackbody algorithm is applied for the temperature calculation based on the visual color intensities in the image. Based on two-color algorithm, two new techniques for temperature calculations are proposed in this work: the reference method and camera response curve method.

The reference method is based on a known temperature measured by the thermocouple or IR gun in a specified region. It works well when the corresponding reference region in the image is precisely defined. The accuracy of the calculated result is as good as the one of the method used to obtain the reference temperature, i.e. IR-Gun or thermocouple readings.

The camera response curve method as proposed here is based on the assumption that the camera sensor responses are linear with respect to source intensity. It utilizes two-color blackbody technique and flame adiabatic temperature condition.  It doesn't need the reference points so it is independent of the IR-Gun and thermocouple readings. However, the camera response curve is needed which can be obtained from the manufacturer or the retailers.

The above two methods are applied for the flame and wall temperature calculations in pilot scale furnace and high temperature industrial gas-fired furnace. Various experiments are performed and temperature data are collected both with IR-Gun and thermocouples. These data are then compared with the results of CCD camera images using the proposed methods. Calculated temperatures indicate that these methods yield excellent results that are closely comparable with both the IR-Gun reading and thermocouples records.  Calculated temperature trends in the pilot scale glass furnace also follow the temperature trend from thermocouples and provide more detailed temperature variations as compared to thermocouple readings.

The camera calibration technology is utilized and integrated with these temperature calculation methods to produce a three dimensional furnace wall temperature profiling. The linear model and nonlinear model of camera calibration technology are

tested and verified in an experiment for measuring the dimension of a basketball court. Since there is limited dimensional information for non-linear calibration model in the furnace, the linear model is selected for the camera calibration.

The linear model is integrated with reference method and camera response curve method to obtain three dimensional temperature distributions for the furnace walls and crown and provide temperature profiling for a specified region such as the burner port area as well as the crown, and sidewalls associated with specific burner port. Calculated temperature results and corresponding trends indicate that these methods yield temperatures that are closely matched with the IR-Gun reading and thermocouples records and trends in commercial gas fired glass furnace as well as the pilot scale furnace.

If enough dimensional information for the furnace can be obtained in the future, the non-linear model could be utilized for increasing the accuracy of the camera calibration model. However, the non-linear model will consume more computational time than the linear model. In order to provide real-time temperature monitoring, the non-linear model is prepared for faster optimal algorithm.

With the development of CCD camera, more and more high-resolution and high-speed CCD cameras are being designed and produced. In the future research, the camera with high-resolution or high-speed camera could be employed for new experiments.

As discussed in this work, the camera adjustment is critical for the data acquisition during the experiments. The camera adjustments make an effect on the color intensity ratio and temperature results. Since the new CCD cameras have more customized adjustments such as iris, gain, and shutter speed, the adjustment effect on the color intensities could be investigated in the future experiments.

With the development of advanced CCD cameras, the cost of CCD camera is declining. Some researchers propose new experiment design to install multiple cameras in the furnace to capture the images from different angles. Zhou et al [73-74] proposed the design with installing eight fictitious CCD cameras in the furnace and produced the visualization of three-dimensional temperature distribution. They only proposed the experiment design and didn't implement the experiment. Since multiple CCD cameras will result in high cost and heavy maintenance burden, it is hard to realize to install eight cameras in the real-world industry. However, it could be possible to install two or three CCD cameras in the furnace experiment. The images from different cameras can be utilized to reconstruct the three dimensional vision for the flame and walls in the furnace. The design and implementation of the experiments will be the challenges for the future research.

# Appendix 1    Panasonic GP KR-222 CCD Specification



**Features[75]:**

- 1/2" interline transfer CCD with 768 (H) x 494(V) pixels
- 480-line horizontal resolution
- Minimum scene illumination of 3 lux at F1.4
- Signal-to-noise ratio of 50dB
- Digital signal processing circuit
- Electronic Light Control and Backlight Compensation
- C or CS-mount selectable
- S-VHS (Y/C) & Standard NTSC Composite output
- Selectable aperture level
- Auto Gain Control
- 12 Volt DC operation

**Specification:**

- Camera System: NTSC or PAL (GP-KR222E)
- Pick-up Device: 768 (H) x 494 (V) Pixels, interline transfer CCD
- Scanning Area: 525 lines/60 fields/30 frames horizontal 15.734kHz
- Scanning System: 2:1 interlace
- Synchronization: Internal
- Video Output: 1.0Vp-p NTSC composite / 75 ohms
- Horizontal Resolution: 480 TV lines

- S/N Ratio: 50dB (min.) (luminance S/N) (at AGC off, weight on)
- Minimum Illumination: 2 lux at f1.2 (3 lux at f1.4)
- AGC (Automatic Gain Control): Selectable on and off (approximately 14dB)
- White Balance: Selectable ATW and AWC (with white balance R/B VR)
- Aperture: Selectable - SOFT (off) / SHARP (on)
- Electronic Light Control: Equivalent to 1/60s - 1/15700s continuous variable shutter speed
- Lens Mount: Selectable C-mount and CS-mount
- Auto Iris Lens Type: DC Type Auto-Iris
- BLC (Backlight Compensation): Selectable normal and backlight control
- Y/C Out: Y out (1.0Vp-p/75 ohms)
- C out (0.286Vp-p/75 ohms burst level)
- Power Requirements: 10.8 to 16 Volts D.C.
- Dimensions: (excluding lens) 2 1/8"H x 2 5/8"W x 4 13/16"D
- Weight: 460g (1 lbs.)
- Operating Ambient Temperature: +14°F to +122°F

# Appendix 2    MicroPix IEEE1394 C640/C1024 CCD Camera Specification



The MicroPix camera series is a IEEE-1394 compliant (Firewire-based) progressive scan monochrome or color CCD camera designed for scientific or industrial imaging applications.  Through the IEEE-1394 interface, reliable transmission of images and full software control of the camera parameters are assured.  No Framegrabber is required ! [76]

**Features**

- PROGRESSIVE SCAN 1/3" CCD SENSOR
- UP TO 1024 (h) x 768 (v) PIXELS
- COLOR
- UP TO 30 FRAMES / SEC
- 24 BIT RGB COLOR
- AUTO SYNCHRONIZATION
- EXT TRIGGER & TWO STROBE I/O
- C/CS MOUNT w/ BACK FOCUS ADJUST

| MODEL | C640 | C1024 |
|---|---|---|
| Sensor Type | 1/3-in. HAD<br>Color – Bayer Tiled<br>Sony ICX-084AK | 1/3-in. HAD<br>Color – Bayer Tiled<br>Sony ICX-204AK |
| Effective Pixels | 640 x 480 | 1024 x 768 |
| Pixel Size | 7.4 um x 7.4 um | 4.65 um x 4.65 um |
| Data Output | 24-bit RGB Color<br>or 8-bit Raw Data | 24-bit RGB Color<br>or 8-bit Raw Data |
| Camera Interface | IEEE-1394 based Digital Camera Specification (DCAM v1.3) | |
| Frame Rate | 3.75, 7.5, 15, 30 Frames/Sec<br>(Full Resolution) | 3.75, 7.5, 15 Frames/Sec<br>(Full Resolution) |
| Partial Scan | 640 x 240 @ 50 Frames/Sec | N/A |
| Electronic Shutter | Auto Electronic Shutter (AES) or Manual Software Ctrl.  1/30 sec.<br>To 1/16,000 | |
| Extended Exposure | 1/30 sec.  To 64 Sec | |
| White Balance | N/A<br>Auto / Manual | N/A<br>Auto / Manual |
| Gain | Auto / Manual Software Ctrl 0-34dB (.035 Steps) | |
| Auto Synchronization | 125 us or Better | |
| External Triggering | + TTL (Max Delay 6 us) | + TTL (Max Delay 10 us) |
| General Purpose I/O | Two I/O pins.  User Defined for Input, Output, Async Trigger, or Strobe<br>( 1.3 volt w/ var.  delay & pulsewidth ) | |
| S/N | 58dB or Better | |
| Min.  Illumination (est) | 2 Lux F/2.0<br>( at 1/30 sec.) | 4 Lux F/2.0<br>( at 1/30 sec.) |
| Lens Mount | C / CS Mount (Adjustable Back Focus) | |
| Dimensions | 6.8 x 5.6 x 3.6 (cm) | |
| Mass / Weight | 250 g (9 oz.) | |
| Power Requirements | 12 Volts Provided by IEEE-1394 Port, Approx.  1.5 Watts | |

# Appendix 3     Sony ICX-084AK CCD sensor response curve
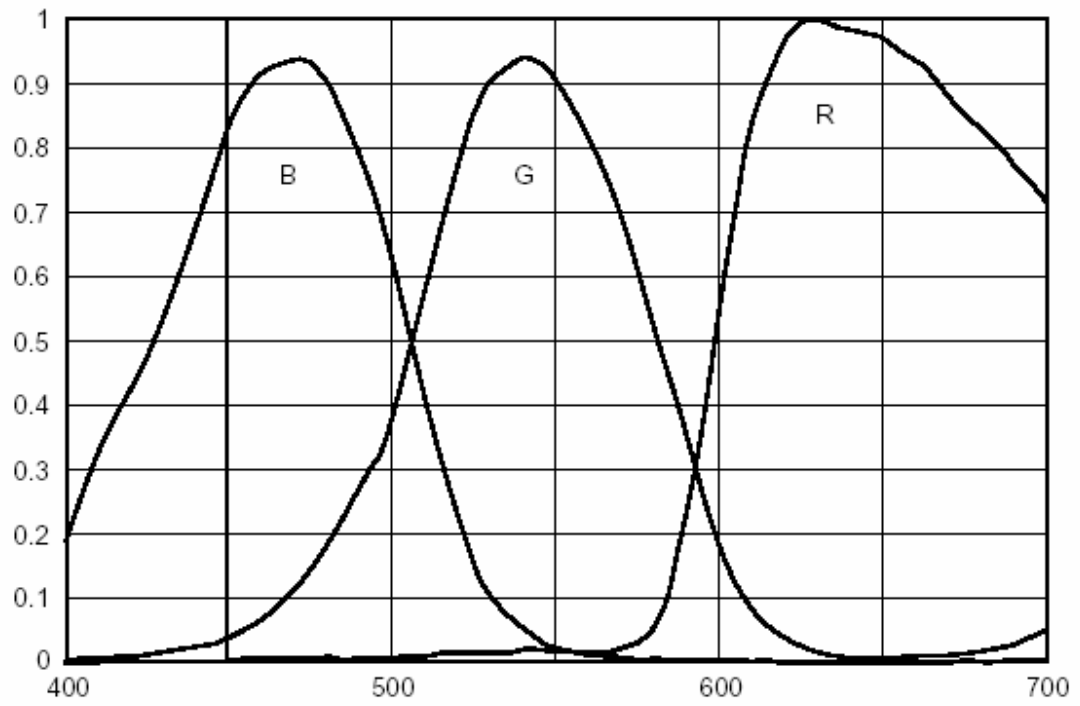


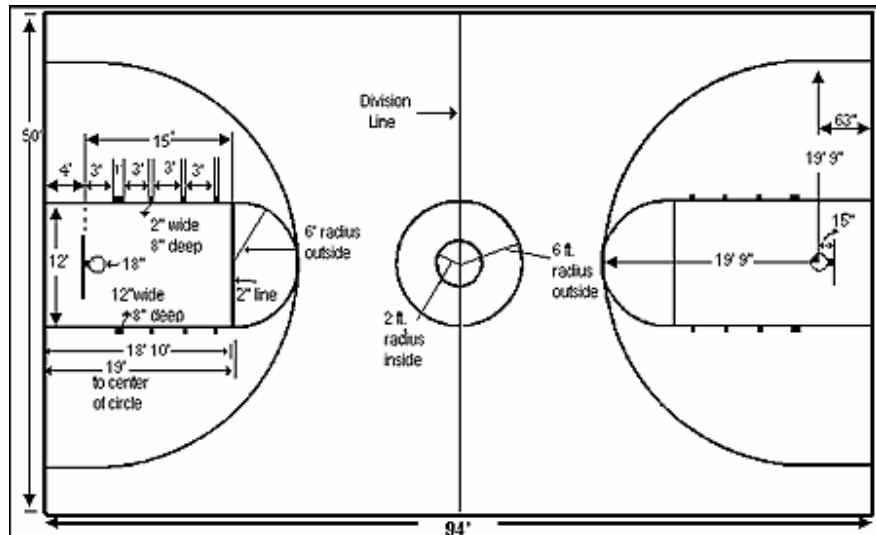Sony CCD sensor ICX-240AK Response curve[77]

# Appendix 4　　　Sony ICX-240AK CCD sensor response curve
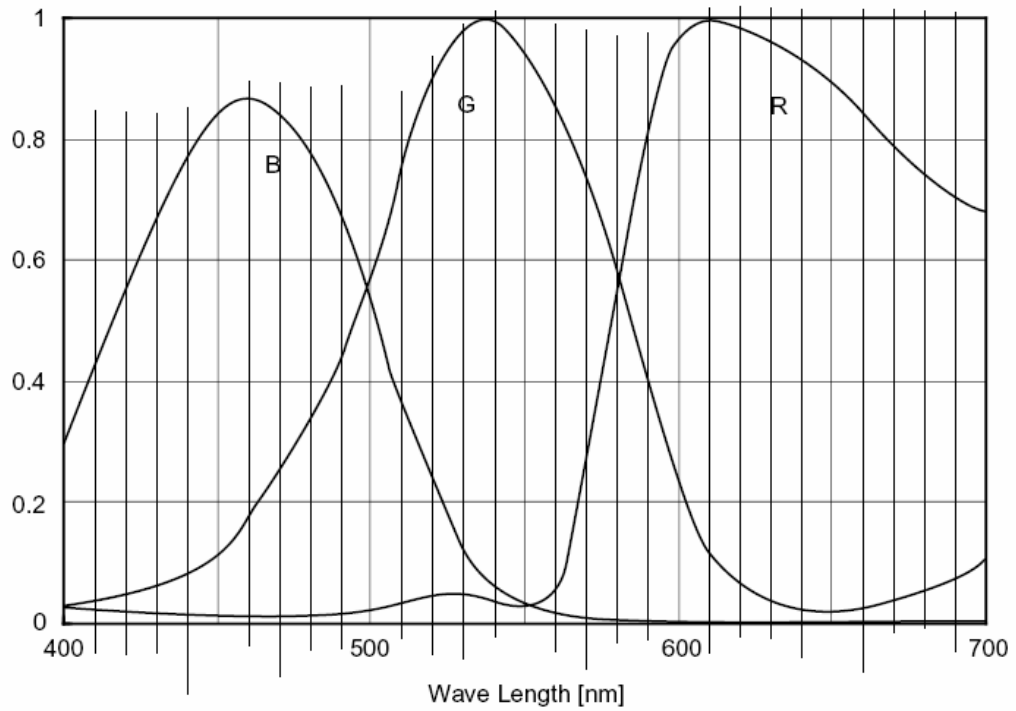


Sony CCD sensor ICX-240AK Response curve[78]

# Appendix 5     Basketball and Volleyball Court Dimensions

**Basketball Court Dimension**



The court dimensional information is as follows:[79]

• An NBA and official NCAA (college) court is 94 ft long and 50 ft wide.
• Half court is well.. half the distance of the full court.

• The free throw line is always 15 ft from the line to the backboard

• The distance from the ground to the rim is 10 ft.

• The 3 point arc in the NBA is 22ft to the center of the rim on the sides ( the arc starts 5 ft 3 in from the baseline, being a straight line until that point) then the curved part of the arc is 23ft. 9 in. from the center of the rim.

• The 3 point arc in college and high school is 19 ft 9 in. (The straight part extends 63 in out from the baseline before the arc begins).

• The key is 12 feet wide (the width of the free throw line) the backboard should extend 4 feet out over the baseline. The 12 ft wide free throw line forms the center of a circle with a 6 ft radius.

• The backboard is 72 inches wide by 42 inches high and has an 18 inch diameter rim.
• The inner square is marked above the rim in a rectangle of 24 inches wide and 18 inches high.

• The line markings are white and 2 inches wide.

## Volleyball Court Dimension

The volleyball court dimension is illustrated as follows[80]:
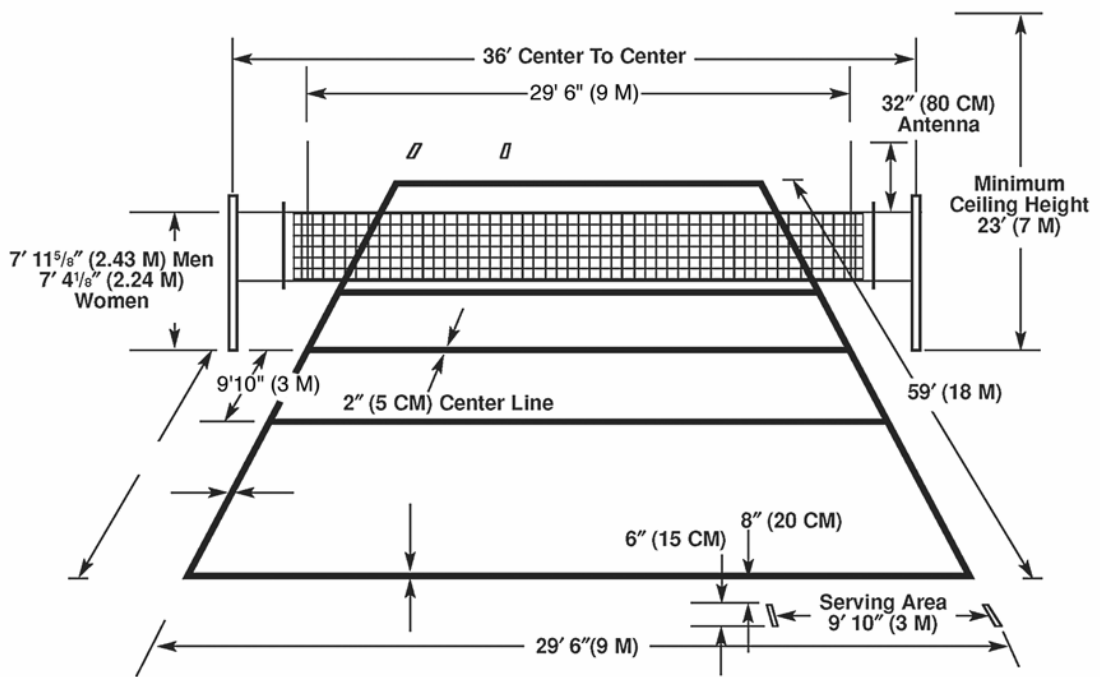
# BIBLIGRAPHY

[1]     H.D. Baker, M.E. Ryder and N.H. Baker, "Temperature Measurement in Engineering Vol. I " *John Wiley & Sons Inc*, New York, 1953.

[2]     L. Michalski, K. Eckersdorf, and J. McGhee, "Temperature Measurement," J. Wiley, New York, 1991

[3]     R.G. Siddall and I.A. Mcgrath, "The Emissivity of Luminous Flames," *Nine Symposium (International) on Combustion*, The combustion institute, pp. 102-110

[4]     H.C. Hottel and F.P. Broughton, "Determination of true temperature and total radiation from luminous gas flames," *Industrial and Engineering Chemistry (Analytical Edition)*, Vol. 4, No. 2, 1932, pp 166-175

[5]     K.L. Cashdollar, "Three-wavelength Pyrometer for Measuring Flame Temperatures," *Applied Optics*, Vol. 18(15), pp. 2595-2597.

[6]     R.A. Felice, "The Spectropyrometer – a Practical Multi-wavelength Pyrometer", t*he 8$^{th}$ Symposium on Temperature: Its Measurement and Control in Science and Industry*, 2002

[7]     U.E. Meier, D. Wolff-Gassmann, J. Heinze, M. Frodermann, I. Magnusson, and G. Josefsson, "LIF Imaging of Species and Temperature in Technical Combustion at Elevated Pressures," *Instrumentation in Aerospace Simulation Facilities, 18th International Congress*, 1999, pp. 701–710

[8]     G.S. Elliot, N. Glumac, and C.D. Carter, "Molecular Filtered Rayleigh Scattering Applied to Combustion," *Measurement Science and Technology,* 12 (2001), pp. 452-456.

[9]     C. Romero, X. Li, S. Keyvan, and R. Rossow. "Spectrometer-Based Combustion Monitoring for Flame Stoichiometry and Temperature Control," *Applied Thermal Engineering*, 25 (2005) pp. 659-676

[10]    W. Wojcik, T. Golec, A. Kotyra, "Combustion Assessment of Pulverised Coal and Secondary Fuel Mixtures Using the Optical Fiber Flame Monitoring System," *Modern Problems of Radio Engineering, Telecommunications and Computer Science. Proceedings of the International Conference*, Feb. 24-28 2004 pp. 464 – 467

[11]    T. Shimada and T. Akiyama, "Spectroscopic Observation of Luminous Flames in an Industrial High Efficiency Test Furnace with Regenerative Combustion of Heavy Oil and Heat Analysis," *Proceedings of 2000 International Joint Power Generation Conference*, July, 2000, pp 1-6

[12]    Y. Huang, Y. Yan, and G. Riley, "Vision-based Measurement of Temperature Distribution in a 500-kW Model Furnace Using the Two-colour Method," *Measurement* 28, 2000, pp. 175-183

[13]    M.J. Saeger, "Sepctroscopic Measurements in Flames for Glass Furnace Applications", Master thesis in Lehigh University, 2002

[14]    E.L. Dreniak and G.D. Boreman, "Infrared Detectors and Systems," *Wiley-Interscience publication, John Wiley & Sons, Inc*, New York, 1996

[15]    E. Renier, F. Meriaudeau, P. Suzeau, and F. Truchetet, "CCD Temperature Imaging: Applications in Steel Industry," *Industrial Electronics, Control, and Instrumentation, Proceedings of the 1996 IEEE IECON 22nd International Conference on*, Volume: 2, 5-10 Aug. 1996, pp. 1295–1300

[16]    P. Cielo and G. Vaudreuil, "Infrared Temperature Sensors for Control of the Surface Melting Process on Superconducting Ceramics," in *Proceedings of the LAMP '92*, Nagoaka, pp. 421-426.

[17]    H. Lee, "Introduction to Color Imaging Science", *Cambridge*, 2005

[18]    J. Chen, P. Osborn, A. Paton, and P.Wall, "CCD Near Infrared Temperature Imaging in the Steel Industry," *Industrial and Measurement Technology Conference*, 1993, pp 299-303.

[19]    M. Shimoda, A. Sugano, Y.Watanabe, T. Kimura and K. Tshiyama, "Prediction Method of Unburnt Carbon for Coal Fired Utility Boiler Using

Image Processing Technique of Combustion Flame," *IEEE Transactions on Energy Conversion*, Vol. 5, No.4, December 1990

[20]     G. Lu, S. Siouris, Y. Yan, C.W. Wilson, and S. Cornwell, "Concurrent Measurement of Combustion Oscillation and Temperature of Multiple Flames in a Simulated Gas Turbine," *Instrumentation and Measurement Technology Conference, Proceedings of the 21st IEEE* , Vol. 2 , 2004 pp. 1112-1115.

[21]     Y. Huang, Y. Yan, and G. Riley, "Vision-based Measurement of Temperature Distribution in a 500-kW Model Furnace Using the Two-colour Method," *Measurement* 28, 2000, pp. 175-183.

[22]     G. Lu, H.C. Bheemul and Y. Yan, "Concurrent Measurements of Temperature and Soot Concentration of Pulverized Coal Flames," *IEEE Instrumentation and measurement Technology Conference*, 2001, pp.1221-1225.

[23]     G. Lu, Y. Yan and O.D Ward, "Advanced Monitoring, Characterization and Evaluation of Gas-fired Flames in a Utility Boiler," *Journal of the Institute of Energy*, March 2000, Vol. 73, pp. 43-49.

[24]     G. Lu, Y. Yan, and D.D. Ward, "Advanced Monitoring and Characterization of Combustion Flames," *Advanced Sensors and Instrumentation Systems for Combustion Processes (Ref. No. 2000/080) IEE Seminar*, 27 June 2000, pp. 3/1 – 3/4.

[25]     G. Lu, Y Yan, M. Colechin, "A Digital Imaging Based Multifunctional Flame Monitoring System," *IEEE Transactions on Instrumentation and Measurement*, Vol. 53, Issue: 4, Aug.  2004, pp. 1152 – 1158

[26]     V. Manta, F. Cignoli, S. Iuliis, and G. Zizak, "2-D Soot Diagnostic with a Two-Color Emission Technique," *XXIII Event of the Italian Section of The Combustion Institute*, Lacco Ameno, Ischia, Napoli, May 22-25, 2000

[27]     Y. Chen, "Simultaneous Measurement Of Time-Resolved 2-D Temperature Distribution of Evaporation Surface Heated by Swept Electron Beam," *IEEE Transactions on instrumentation and measurement*, Vol. 50, No. 3, June 2001

[28]     J.A. Santos-Victor, J.P. Costeira, J.A.B. Tome, and J.J.S Sentieiro, "A Computer Vision System for the Characterization And Classification of Flames in Glass Furnaces," *IEEE Transactions on Industry Applications*, Vol. 29, Issue: 3, May-June 1993 pp. 470–478

[29]     G. Lu, Y. Yan, M. Colechin, and R. Hill, "Monitoring Of Oscillatory Characteristics of Pulverized Coal Flames through Image Processing and Spectral Analysis," *Instrumentation and Measurement Technology Conference, 2004. Proceedings of the 21st IEEE*, Vol. 3, 18-20, May 2004, pp. 1801 - 1805

[30]     T. Lalannea and C. Lempereur, "Color Recognition with a Camera: a Supervised Algorithm for Classification," *Image Analysis and Interpretation, 1998 IEEE Southwest Symposium on*, 5-7 April 1998, pp. 198–204

[31]     J. Bojkovski, V. Batagelj, I. Pusnik, and J. Drnovsek, "Using a CCD Camera for the Determination of the Target Size in Radiation Thermometry," *IEEE Transactions on Instrumentation and Measurement*, Vol. 53, Issue: 3, June 2004, pp. 661–664

[32]     W.B. Baek, S.J. Lee, S.Y. Baeg, and C.H. Cho, "Flame Image Processing and Analysis for Optimal Coal Firing of Thermal Power Plant Industrial Electronics," *Proceedings, ISIE 2001, IEEE International Symposium on*, Vol. 2 , 12-16 June 2001 pp. 928-931

[33]     F. Wang, X.J. Wang, and Z.Y. Ma, "The Research on the Estimation for No$_x$ Emissive Concentration of the Pulverized Coal Boiler by the Flame Image Processing Technique," *Fuel* 81(2002) pp. 2113-2120

[34]     M. Takeuchi and T. Kubono, "A Spectroscopic Detecting System For Measuring the Temperature Distribution of Silver Breaking Arc Using a CCD Color Camera," *IEEE Transactions on Instrumentation and Measurement*, Vol. 48, No.3, June 1999.

[35]     H. Yamagishi and J. Yamaguchi, "Fire flame Detection Algorithm Using a Color Camera," *International Symposium on Micromechatronics and Human Science*, 1999. pp. 255-259

[36]     Glad, F.A., "Color Temperature Alignment Using Machine Vision," IEEE Transactions on Consumer Electronics, Vol. 37, Issue: 3, Aug 1991, pp. 624–628

[37]     M. Planck, "Distribution of Energy in the Spectrum," Annals of Physics, Vol. 4, No. 3, 1901, pp. 553-563

[38]     J.A Barnard and J.N. Bradley, "Flame and Combustion," *Chapman and Hall*, London, 1985, pp. 163.

[39]     H. Hottel, "Background and Perspectives on Temperature Measurement in Furnaces," *Measurement of high temperatures in furnaces and processes. AlChE Symposium Series*, ed. David P. DeWitt and Lyle F. Albright (New York: American Institute of Chemical Engineerings, 1986) 1-12

[40]     G. Ewing, "Instrumental methods of chemical analysis," *McGraw-Hill*, New York, 1969, pp 176-179.

[41]     J. Nakamura, "Image Sensors and Signal Processing for Digital Still Cameras," *Taylor & Francis Group*, CRC press, Boca Raton, 2006

[42]     B. Jahne, "Image Processing for Scientific Applications," *CPC Press*, New York, 1997

[43]     R. Parenti, P. Verrecchia, G. Bosla and E. Pignone, "Industrialized Real-Time Flame Thermal Mapping System with Off-Line Correction of Spatial Error," *Industrial Electronics, Control and Instrumentation*, 1994.  IECON '94., 20th International Conference on , Volume: 3 , 5-9 Sept.  1994, pp. 1977-1980

[44]     P.L. Vora, J.E. Farrell, J.D. Tietz, and D.H. Brainard, "Digital color cameras - 1 - Response models," *Hewlett-Packard Co. Tech. Report,* HPL-97-53, Mar 1997

[45]     P.L. Vora, J.E. Farrell, J.D. Tietz, and D.H. Brainard, "Digital color cameras - 2 – Sepctral Response," *Hewlett-Packard Co. Tech. Report*, HPL-97-54, Mar 1997

[46]     P.L. Vora, J.E. Farrell, J.D. Tietz, and D.H. Brainard, "Image Capture: Simulation of Sensor Responses from Hyperspectral Images," *IEEE Transactions on image processing*, Vol. 10, No.2, Feb 2001, pp. 307-316

[47]    L.W. Macdonald and M.R. Luo, "Colour Imaging – Vision and Technology," *John Wiley & Sons Ltd*, England, 1999

[48]    L.M. Macdonald and W. Ji, "Colour Characterization of a High-Resolution Digital Camera," *Colour in Graphics, Imaging and Vision Conference*, Poitiers, April 2002.

[49]    ISO 17321, WD 4, "Graphic Technology and Photography – Colour Characterization of Digital Still Cameras (DSCs) Using Colour Targets and Spectral Illumination", November 1999.

[50]    S. Süsstrunk, R. Buckley, and S. Sven, "Standard RGB Color Space," *Proceedings of IS&T/SID's 7th Color Imaging Conference*, 1999. pp. 127 - 134

[51]    P.M. Hubel, J. Holm, and G.D. Finlayson, "Illuminant Estimation and Color Correction," *Proc. Colour Imaging in Multimedia – CIM98*, Derby, England, 1998, pp. 97-105.

[52]    J. Holm, "Photographic Tone and Colour Reproduction Goals," *Proc. CIE Expert Symposium '96*, 1996, pp. 51-56.

[53]    ISO 17321, "Graphic Technology and Photography – Colour characterization of digital still camera (DSCs) using colour targets and spectral illumination," March 9th 1999.

[54]    ITU-R Recommendation BT.709-3: 2002, "Parameter Values for the HDTV Standards for Production and International Programme Exchange".

[55]    Y. Matsui, T. Kamimoto, and S. Matsuoka, "Study on the Application of the Two-color Method to the Measurement of Flame Temperature and Soot Concentration in Diesel Engines", *SAE*, 1980, paper 800970.

[56]    R.W.G. Hunt, "Measuring colour," *Chichester, [West Sussex]: Ellis Horwood*, New York : Wiley, 1987.

[57]    G. Lu, Y. Yan, G. Riley and H.C. Bheemul, "Concurrent Measurement of Temperature and Soot Concentration of Pulverized Coal Flames", *IEEE*

*Transactions on Instrumentation and Measurement*, Vol. 51, No. 5, October 2002.

[58]    J.M. Char and J.H. Yen, "The Measurement of Open Propane Flame Temperature Using Infrared Technique," *J. Quant. Spec-Radist. Transfer 56 (1)*, 1996, pp. 133–144.

[59]    W.L. Flower, "Optical Measurement of Soot Formation in Premixed Flames," *Combustion Science, Technology,* Vol. 33, 1983, pp.17–33.

[60]    W. L. Grosshandler, "The Effect of Soot on Pyrometric Measurements of Coal Particle Temperature," *Combustion and Flame*, 55:59-71 (1984)

[61]    S. Keyvan, R. Rossow, C. Romero, and X. Li, "Comparison between Visible and Near-IR Flame Spectra from Natural Gas-fired Furnace for Blackbody Temperature Measurements", *Fuel* 83 (2004), pp. 1175-1181

[62]    G.C. Holst, "CCD Arrays, Cameras, and Displays," *SPIE Optical Engineering Press*, Washington USA, 1998

[63]    R.M. Frsistrom, "Flame Structure and Processes," *Oxford University Press*, 1995, pp. 412.

[64]    Y.I. Abdel-Aziz and H.M. Karara, "Direct Linear Transformation into Object Space Coordinates in Close-Range Photogrammetry," Symposium on Close-Range Photogrammetry, Jan 26-29, 1971, pp.1-18.

[65]    R.Y. Tsai, "A Versatile Camera Calibration Technique for High Accuracy 3D Machine Vision Metrology Using Off-the-Shelf TV Cameras and Lenses," IEEE J. Robotics Automat., Vol. RA-3, No. 4, Aug. 1987, pp. 323-344.

[66]    J. Weng, P. cohen, and M. Herniou, "Camera Calibration with Distortion Models and Accuracy Evaluation," *IEEE Transactions on pattern analysis and machine intelligence*, Vol. 14, No. 10, Oct 1992, pp. 965-980

[67]     W. Faig, "Calibration of Close-range Photogrammetry Systems: Mathematical formulation," *Photogrammetric Engineering and Remote Sensing*, Vol. 41, No. 12, 1975, pp. 1479-1486.


[68]     I. Sobel, "On Calibrating Computer Controlled Cameras for Perceiving 3-D Scenes," Artificial Intelligence, Vol. 5, 1974, pp. 185-198


[69]     M.A. Sid-Ahmed and T.B. Mohamed "Dual Camera Calibration for 3-D Machine Vision Metrology," IEEE Transactions on Instrumentation and Measurement, Vol. 39, 1990, pp. 512-516.


[70]     B. Hakan and S.K. Mohamed, "A Three-Step Camera Calibration Method," IEEE Transactions on Instrumentation and Measurement, Vol. 46, No. 5, 1997, pp. 1165-1172


[71]     B. Caprile and V. Torre, "Using Vanishing Points for Camera Calibration," International Journal of Computer Vision, 4(2), 1990, pp. 127-140


[72]     H. Zhuang and A.S. Roth, "Camera-Aided Robot Calibration," *CRC press*, 1996


[73]     H. Zhou, S. Han, F. Sheng and C. Zheng, "Visualization Of Three-Dimensional Temperature Distributions in a Large-Scale Furnace via Regularized Reconstruction from Radiative Energy Images: Numerical Studies," *Journal of Quantitative Spectroscopy & Radiative Transfer,* Vol. 72, 2002, pp. 361-383.


[74]     H. Zhou, F. Sheng, S Han, Y Huang, and C. Zheng, "Reconstruction of temperature Distribution in a 2-D Absorbing-emitting System from Radiant Energy Images", JMSE International Ser B 2000; 43(1), pp.104-109


[75]     Panasonic KR222 camera Specifications

**http://catalog2.panasonic.com/webapp/wcs/stores/servlet/ModelDetail?storeId=11201&catalogId=13051&itemId=67849&catGroupId=14872&displayTab=S&surfModel=GP-KR222&surfCategory=Discontinued**


[76]     MicroPix C640/C1024 camera specification

**http://www.aegis-elec.com/products/micropix-cam.html**

[77]     Sony ICX-084AK CCD sensor response curve.
         **http://products.sel.sony.com/semi/PDF/ICX084AK.pdf**


[78]     Sony ICX-204AK CCD sensor response curve
         **http://products.sel.sony.com/semi/PDF/ICX204AK.pdf**


[79]     Basketball court dimension
         **http://www.halfcourtsports.com/HCS_Basketball_Court_Dimensions.html**


[80]     Volleyball court dimension
         **http://www.tomark.com/GDPoll/volleyballcourtdiagram.html**

# VITA

Dong Li was born on February 24th, 1972, in Liaoning, China. After attending public schools in Liaoning, China, he received the following degrees: B.S. in Aerospace Engineering from Beijing University of Aerospace and Astronautics in Beijing, China (1994); M.S. in Aerospace Engineering from Beijing University of Aerospace and Astronautics at Beijing, China (1997). After the graduation, he worked as an engineer in Air China for about three years.

He began to study for PhD degree in Mechanical and Aerospace Engineering at the University of Missouri – Columbia on January 2000. He transferred to Computer Science and Computer Engineering Department on September 2000 and obtained M.S. in Computer Science from University of Missouri – Columbia at Columbia, Missouri (2004).